Università
degli Studi
di Padova

Sede Amministrativa: Università degli Studi di Padova

Dipartimento di Ingegneria Civile, Edile ed Ambientale

SCUOLA DI DOTTORATO DI RICERCA IN:

SCIENZE DELL'INGEGNERIA CIVILE E AMBIENTALE

INDIRIZZO: COMUNE, XVIII CICLO

MODELLING BIOMECHANICAL PROBLEMS IN THE FRAMEWORK OF POROUS MEDIA MECHANICS: DIABETIC FOOT AND BIOLOGICALLY INSPIRED SCAFFOLDS

Direttore della Scuola: Ch.mo Prof. Stefano Lanzoni

Supervisore: Ch.ma Prof.ssa Daniela Boso

Dottorando: Mattia Pizzocaro

This doctoral thesis has been approved as follows:

Prof. S. Lanzoni . . . .

Director of the PhD program

Prof. D. P. Boso. . . . .

Thesis Supervisor

Mattia Pizzocaro . . . .

PhD Candidate

Abstract

The Theory of Porous Media is applied in this thesis to two different biomechanical problems. First, a computational model of the diabetic foot is developed by taking advantage of patient specific geometries and time-dependent loads experimentally measured. Differently from the state-of-the-art hyperelastic behavior, the plantar tissue is modelled as a fully saturated porohyperelastic porous medium. In this way, time becomes a variable with a real physical meaning, allowing to consider the peculiarities of the subject specific gait cycles. In addition, thanks to the two different phases constituting the medium (i.e. solid and fluid phases), total stress can be split into interstitial fluid pressure and effective stress contributions. Thus, the position and the value of peaks is different, whether total or effective stress are considered, and the peaks in effective counterparts are increasing with the number of gait cycles, as a result of the fluid-structure interaction. By taking advantage of these results we hypothesized that the development of the ulceration phenomenon in the diabetic foot is guided by the excess of an average effective pressure limit. Due to the lack in literature of specific ulceration triggering stress value, maximum average pressure values found for a healthy subject are used as triggering values for the diabetic foot model. As a result, the development of the ulcers within the plantar tissue is mimicked, showing ulcer positions that are in good agreement with the one observed by clinicians.

The second application is the scaffold for the spinal fusion: starting from experimental results, a computational model of tissue differentiation is developed, guided by mechanical stimuli applied. The model obtained is capable to predict the tissue formation in post-surgery period, reducing the velocity of tissue transformation depending on stress values found in literature. It can be used by clinicians as a tool for defining subject specific scaffold dimensions and after surgery loading guidelines.

The last biomechanical application is the three layer composite scaffold for the articular defect repair. Due to the complexity of the problem, a scaffold with final

tissue developed is taken into account and its behavior as a function of loads applied is studied. By taking advantage of the experimental loads from the diabetic foot, we hypothesized to place the scaffold in a knee joint. Thus, it is loaded with vertical and shear loads, studying the development of effective stresses and interstitial fluid pressure within the domain. The numerical results allowed us to suggest an enhancement of the composite scaffold configuration, to avoid stress peaks patterns in the bone layer of the scaffold.

The Theory of Porous Media allowed us to make a step forward with respect to the state of the art modelling in different biomechanical fields, by developing computational models that can be used by physicians as effective tools in conjunction with experimental results.

Sommario

La Teoria dei Mezzi Porosi è stata applicata in questa tesi a due differenti applicazioni nell'ambito della biomeccanica. In primis è stato sviluppato un modello computazionale per il piede diabetico, sfruttando geometrie *patient specific* e carichi dipendenti dal tempo misurati sperimentalmente. Contrariamente al comportamento iperelastico usualmente utilizzato in letteratura, il tessuto plantare è stato modellato come mezzo poroso poroiperelastico completamente saturo. In tale maniera è stato possibile considerare la variabile tempo come una reale variabile fisica, permettendoci di tenere in considerazione le peculiarità del ciclo del passo del soggetto. Inoltre, grazie alla presenza delle due fasi che costituiscono il mezzo (fase solida e fase fluida), è stato possibile suddividere il contributo di stress totali in tensioni efficaci e pressione del fluido interstiziale. Di conseguenza la posizione dei picchi e la loro intensità risulta differente, a seconda che si consideri la componente totale o la controparte effettiva dello stress, e l'effetto dell'interazione fluido struttura determina un andamento crescente dei picchi con il numero dei cicli del passo compiuti. Tenendo conto dei risultati così ottenuti, si è ipotizzato che lo sviluppo del processo di ulcerazione nel piede diabetico sia guidato dal superamento di un valore limite di pressione effettiva media. A causa dell'assenza in letteratura di valori tensionali di soglia per l'innesco dell'ulcera, i valori massimi di pressione media efficace riscontrati nel modello del piede sano sono stati impiegati come valori limite per il piede diabetico. I risultati numerici così ottenuti hanno mostrato posizioni di innesco e sviluppo dell'ulcera nel tessuto plantare che sono in buon accordo con quelle riscontrate nella realtà dai clinici.

La seconda applicazione considerata è stato lo scaffold per *spinal fusion*: partendo dai risultati sperimentali, si è sviluppato un modello computazionale di differenziazione tissutale guidato da stimoli meccanici applicati. Il modello così ottenuto ha permesso di predire la formazione tissutale nella fase post operatoria, riducendo la velocità di trasformazione dei tessuti in funzione di specifici valori

tensionali trovati in letteratura. In tale maniera è stato possibile offrire ai medici uno strumento con cui si possa definire un dimensionamento *patient specific* dello scaffold e si possano sviluppare delle linee guida di carico per la fase post operatoria.

L'ultima applicazione in ambito biomeccanico analizzata è lo scaffold composito tristrato per la riparazione di difetti articolari. A causa della complessità del fenomeno si è considerato uno scaffold con tessuti target sviluppati e si è studiato il suo comportamento soggetto a differenti carichi applicati. Ipotizzando di porre lo scaffold in una articolazione del ginocchio, abbiamo utilizzato i carichi sperimentali ottenuti per il piede diabetico. Abbiamo così caricato lo scaffold con i carichi verticali e taglianti, studiando l'andamento della pressione del fluido e le tensioni efficaci nel tempo all'interno dei tre strati che lo compongono. I risultati numerici ottenuti ci hanno permesso di ipotizzare un miglioramento del layout dello scaffold composito, finalizzato a ridurre picchi tensionali che hanno origine nello strato osseo di quest'ultimo.

Grazie all'applicazione della Teoria dei Mezzi Porosi è stato dunque possibile compiere alcuni passi in avanti rispetto allo stato dell'arte in differenti campi della biomeccanica computazionale, permettendoci di fornire ai clinici utili strumenti che possono essere utilizzati a supporto dei risultati sperimentali.

Contents

List of Figures

List of Tables

1. General introduction: setting the stage

Nowadays, computer-assisted analyses are assuming a key role in different scientific and industrial fields, thanks to the rapid progresses in computational performance and efficiency. In the last four decades the development of the Finite Element Theory [1]–[4] opened to new scenarios that could not be imagined before. The capability of solving differential equation in an approximated way allows to resolve numerical models for continua that are able to catch their real physical behavior. In this sense, recently a revolution has started from the industry: because of the prominent costs of prototypes and experimental tests in a product conception, computational models are becoming the beginning point of the process. In this way, the optimization of geometries and materials becomes a more straightforward task, validated through preliminary in silico tests, in a low-consumption-of-resources way of working. Consequently, only few prototypes are produced and tested before the mass production, letting the research & development (R&D) department focus on more peculiar aspects in the product design. Similarly, it can be performed in field where experimental tests are extremely difficult to succeed, such as superconducting materials [5] and, of course, in biological contexts, where tests must be often done *in vivo* with experiments on animals (e.g. in [6]) or human subjects.

In this framework a new synergy between clinicians and engineers is reached (e.g. [7]–[10]). Thanks to the sharing of expertise from different fields of knowledge, a deeper understanding of complex biomechanical phenomena can be achieved.

On one hand physicians, biologists and chemists bring their medical and biological know-how about the problem considered. On the other hand, engineers, physicists and mathematicians can develop computational models to represent the phenomenon of interest and foretell its evolution. Prosthesis and medical procedures in rehabilitation or after-surgery healing process can be studied, thus reducing the need of a large amount of experimental tests as well as the number of prostheses prototypes fabricated in the product development.

This thesis is structured into four main parts: in *Chapter 1* a brief introduction of this work is presented, highlighting the collaboration that gave the aims to this work and the innovative aspects developed. In *Chapter 2* the theory foundations of the porous media and mass diffusion are extensively laid. In *Chapter 3* the general basis introduced are targeted to the specific biomechanical applications, developing computational models.

1.1. The collaborations

This work was developed in collaboration with different teams, composed of biologists, bioengineers and physicians: this partnership was certainly worthwhile, but also highly challenging, due to the need of developing transversal skills between the actors involved. The following considerations about the collaborations could seem trivial, but a great effort had to be done to accomplish good results. First, it was necessary to share the fundamental mechanisms of the phenomenon under study, to define correctly the problem to model: the main difficulty was certainly finding a common language of communication, because of the differences in the knowledge backgrounds. Second, it was necessary to select only the specific aspects that we wanted to investigate, in an engineering perspective. Finally, the computational models were written, defining their range of applicability, explicitly declaring in which situation and for what purpose they are supposed to work properly.

This thesis takes advantage of the expertise from different research groups, whose aims are briefly summarized here:

I. *The DICEA team (composed by M. Pizzocaro, D. Boso, P. Mascheroni, G. Sciumè and B. Schrefler)*

My team worked for years in the field of continuum mechanics, reaching a specific theoretical and computational expertise in the porous media and in composite material fields. Nonlinearity in computational mechanics (i.e. contact, geometry and constitutive equations) was extensively studied, leading the research group to deal with different field of applications, such as landslides, fracking and superconducting materials. Starting from the knowledge acquired on porous media in soils, our group in the last years opened to new applications in biomechanics. The encouraging results obtained by modelling the tumor growth drove the research team to consider additional new fields of application: the diabetic foot and scaffolds for tissue augmentation, which are the cases studied in this thesis.

II. *The DEI team from Information Engineering Department of University of Padova (IT), (composed by C. Cobelli, Z. Sawacha, A. Guiotto and A. Scarton)*[1].

Their main research application is the diabetic foot prevention. They focuses on the study of subject specific gait, by developing integrated systems for simultaneous acquisition of motion capture, ground reaction forces, plantar pressure and surface electromyography signals. By means of magnetic resonance image processing, they developed a patient specific finite element mesh of the diabetic foot, to be used in conjunction with data coming from gait analysis. This collaboration took place from the shared aim of investigating the foot ulceration risk, in a real time dependent perspective, to help clinicians in the follow up procedure.

III. *The HOUSTON team from the Houston Methodist Research Institute, Texas (US), (composed by S. Minardi, E. Tasciotti, A. Tampieri)*[2].

---

[1] http://biomov.dei.unipd.it/

[2] http://www.houstonmethodist.org/research/our-faculty/labs/tasciotti-lab/

This team is dealing with the development of innovative nanotechnology platforms and biomaterials for drug delivery and regenerative medicine, which includes advanced materials for scaffold[3] reinforcement (e.g. for the repairing of articular defects and for the spinal fusion). This work was born from their need of having a numerical tool to be used in the scaffold development process and in defining post-surgery procedures.

1.2. Innovative aspects of the work

The Theory of Porous Media was originally developed for geomechanics, but recently it has been successfully applied to biological fields, such as the tumor growth [10]–[13] , vertebral implants [14], [15] and scaffolds [16]. Biological tissues are made of micro and macro chambers at microscopic level, which are filled by interstitial fluid, so that their porous nature is evident. In tissue mechanics, differently from other widespread and consolidated constitutive theories, the porous medium behavior shows many advantages. First, time becomes a variable with a real physical meaning, allowing to consider time dependent loading configurations. Second, stresses within the domain can be separated into total and effective contributions, resulting different peak distributions depending on the variable taken into account. Third, the fluid-structure interaction phenomenon leads to a time dependent stress exchange between solid and fluid medium constituents.

By taking advantage of these valuable properties, in this work we applied the porous media approach to two different biomechanical applications: the diabetic foot and the scaffold for tissue augmentation. Regarding the diabetic foot (§3.1), we started from a patient specific geometry and loads and we developed a porohyperelastic model for the plantar tissue. The specificities of the gait cycles are mimicked, allowing

---

[3] A scaffold is a rather simple high porosity structure, which is able to trigger the cellular differentiation, in order to obtain a specific target tissues (see §3.2 for further details).

us to simulate multiple steps. The aim of this work was to develop a computational tool to identify the areas at risk of ulceration. Starting from numerical results, obtained with a subject specific healthy foot model, we defined pressure thresholds that triggers the ulcer formation and development. The evolution of ulcers within the tissue was then recorded by simulating multiple steps in the diabetic foot model, giving results in accordance with the experimental one.

As a result of collaboration with Houston team, the second biomechanical application is scaffold for tissue augmentation (§3.2.2). Two different models are introduced: one for the scaffold used in spinal fusion and another for the repair of osteochondral defects. By first considering the scaffold for spinal fusion, we developed a porohyperelastic model to predict the tissue differentiation within its domain. This application was born from the clinicians' need of a computational tools to help defining both adequate geometries for the scaffold and loading procedures in the after-surgery phase, to enhance the augmentation of the targeted tissue. The numerical model implemented is able to efficiently mimic the evolution of bone fractions experimentally measured. Furthermore, thanks to the dependence of tissue differentiation on specific mechanical stimuli, it allows us to suggest a limit load that can be applied to the scaffold, depending on its geometry, to induce the tissue differentiation requested.

Finally, the last numerical model is developed for the articular defect repair scaffold. A three-layer heterogeneous porohyperelastic model was introduced, with the aim of studying the effects of loads on the scaffold mechanical behavior and delamination risk.

2. Multiphysics modelling of biological tissues

The multiphysics modelling of biological tissue developed in §3 takes advantage of theoretical grounds of the Diffusion Theory and the Porous Media Theory. In the following paragraphs both theories are discussed.

2.1. The Diffusion Theory

"Diffusion is the process by which matter is transported from one part of a system to another, as a result of random molecular motions" [17, p. 1]. Thanks to its analogy with heat transfer, mass diffusion was defined firstly by Fick in 1855 [18] by exploiting Fourier's heat equations [19].

The fundamental hypothesis of the isotropic diffusion theory is that the rate of transfer of diffusing substance through a unit area of a section is proportional to the concentration gradient, measured normal to the section [17]. This is the Fick's first law of diffusion:

$$\mathbf{F} = -\mathbf{D} \cdot \nabla C \tag{2.1}$$

where $\mathbf{F}$ is the rate of transfer per unit area of section, C is the concentration of the diffusing substance and $\mathbf{D}$ is the diffusion tensor, measured as a ratio of a square length and time; it is usually diagonal and constant, but it can depend on concentration in some particular cases. The negative sign in (2.1) indicates the opposite growth direction between diffusion and concentration gradient (i.e. diffusion starts from places at higher concentration to places at lower).

Differential equations for the isotropic medium can be obtained starting from a rectangular parallelepiped volume element of dimensions of $dx \cdot dy \cdot dz$. Let us consider a Cartesian system of axes with origin (P) in the center of the volume; α and α' are the two faces normal to the x axis (Figure 2.1).

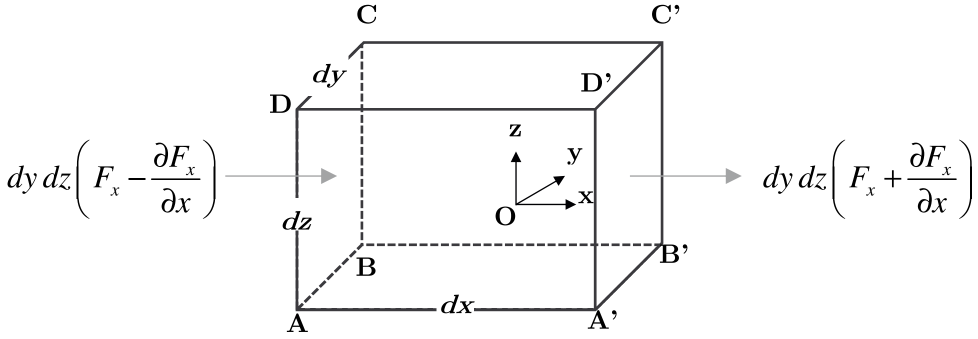

Figure 2.1 Volume element. α is defined by ABCD, whereas α' by A'B'C'D'.

The rate at which the diffusing substance enters the element through α is:

$$dy\,dz\left(F_x - \frac{\partial F_x}{\partial x}dx\right) \tag{2.2}$$

while the rate through the corresponding face α' is:

$$dy\,dz\left(F_x + \frac{\partial F_x}{\partial x}dx\right) \tag{2.3}$$

The net increase rate of diffusing substance along x axis writes:

$$-2dx\,dy\,dz\frac{\partial F_x}{\partial x} \tag{2.4}$$

By doing the same with faces β and β', and γ and γ' (normal respectively to the y and z directions (Figure 2.1)), we obtain:

$$-2dx\,dy\,dz\frac{\partial F_y}{\partial y} \tag{2.5}$$

$$-2dx\,dy\,dz\frac{\partial F_z}{\partial z} \tag{2.6}$$

for the y and z directions respectively.

The net rate of increasing substance in the whole element can be written as:

$$dx\,dy\,dz\frac{\partial C}{\partial t} \tag{2.7}$$

Summing (2.4), (2.5) , (2.6) and writing it equal to (2.7):

$$\frac{\partial C}{\partial t} + \frac{\partial F_x}{\partial x} + \frac{\partial F_y}{\partial y} + \frac{\partial F_z}{\partial z} = 0 \tag{2.8}$$

If the diffusion tensor is constant, we obtain Fick's second law of diffusion:

$$\frac{\partial C}{\partial t} = \mathbf{D} \cdot \nabla^2 C \tag{2.9}$$

Let us consider diffusion in anisotropic media. These media are materials in which molecules show a preferential direction of orientation, such as polymers and crystals. Diffusion in such materials forces us to change some of the fundamental hypothesis of the diffusion theory; because the flow direction of the diffusing substance is not normal to the surface of constant concentration anymore, the diffusion tensor must include also extra diagonal terms in $\mathbf{D}$. First Fick's law (2.1) becomes:

$$\begin{bmatrix} F_x \\ F_y \\ F_z \end{bmatrix} = \begin{bmatrix} D_{11} & D_{12} & D_{13} \\ D_{21} & D_{22} & D_{23} \\ D_{31} & D_{32} & D_{33} \end{bmatrix} \begin{bmatrix} \frac{\partial C}{\partial x} \\ \frac{\partial C}{\partial y} \\ \frac{\partial C}{\partial z} \end{bmatrix} \tag{2.10}$$

where the generic component $D_{\mathrm{ab}} \frac{\partial C}{\partial b}$ in (2.10) is the contribution of mass diffusion along *a*-direction due to a concentration gradient on *b*-direction.

Assuming constant diffusivity terms and substituting (2.10) in (2.8), it leads to the second Fick's law for the anisotropic media:

$$\begin{aligned} \frac{\partial C}{\partial t} &= D_{11} \frac{\partial^2 C}{\partial x^2} + D_{22} \frac{\partial^2 C}{\partial y^2} + D_{33} \frac{\partial^2 C}{\partial z^2} + \left(D_{12} + D_{21}\right) \frac{\partial^2 C}{\partial x \partial y} + \\ &+ \left(D_{13} + D_{31}\right) \frac{\partial^2 C}{\partial x \partial z} + \left(D_{23} + D_{32}\right) \frac{\partial^2 C}{\partial y \partial z} = 0 \end{aligned} \tag{2.11}$$

2.2. The Theory of Porous Media

Multiphase flow and transport in porous media can be described by three balance equations: the conservation of mass, the conservation of momentum and the conservation of energy. Since the number of system variables is higher than the number of equations, *constitutive relations* must be added to close the system, which otherwise would be undetermined [20].

The smallest scale at which the balance equations can be formulated is the continuum scale (called also *the microscale*). At microscale, the material can be seen as continuum, though molecules and atoms in reality occupy only a portion of the space. As a consequence, the number of molecules are averaged in an averaging space, in which the length scale has to be appropriately chosen [21][4]. At the continuum scale the system is generally composed of different phases: a solid phase$\left(s\right)$, a liquid phase $\left(w\right)$ and a gaseous one$\left(g\right)$, which are separated by sharp interfaces. Due to the fact that a high level of detail is required for taking into account this geometric structure, a microscale model is usually very challenging and almost always beyond usual requirements. A larger scale is commonly used, called *the macroscale*, as the reference scale for porous medium models. The macroscale has a characteristic length scale of 10÷100 diameters of medium pores. The averaging region, named the *representative elementary volume* (RVE), must contain each phase. Contrarily to the microscale region, at the macroscale there is no interface between phases after the averaging process. In fact, each phase shares with the others a position and occupies a specific volume fraction of the RVE.

The consistency and the accuracy in the upscaling process from one scale to another is guaranteed by the application of the averaging theories. In this work the

---

[4] By using a length scale sufficiently greater than mean free path, it is possible to include in the averaging region a number of molecules of which the average value is almost independent to small variation in the size of the averaging region.

Thermodynamically Constrained Averaging Theory (TCAT), developed by W. Gray and C. Miller in 2005 [22], is used and it is briefly explained in the following paragraph.

2.2.1. Brief overview of TCAT

The Thermodynamically Constrained Averaging Theory is a rigorous procedure that allows to model multiphase flow in porous media at any scale of interest. It proceeds from microscale relations and, by means of averaging theorems, it leads to macroscale equations. During the process of upscaling, conservation and thermodynamic principles are kept consistent between the scales, satisfying the entropy inequality. In this way, macroscale variables maintain a clear connection to their microscale counterparts [22], avoiding the risk - not so rare in models defined directly at the macroscale - of being inconsistent with microscale physics. Furthermore, contrarily to traditional models, in which balance equations are derived only for the phases, the TCAT also considers interface equations. Spatial and temporal variations of system properties in the transition region between phases [23] are therefore taken into account.

A complete discussion of TCAT is beyond the scope of this thesis, interested reader can find full details of the theory in [20], [22]–[26];

The TCAT approach for developing macroscale models is here summarized following W. Gray and C. Miller in [22] and [27]. The fundamental assumptions are:

1. Mass, momentum, energy balance equations and entropy inequality must be defined at the scale of interest for all the relevant entities (i.e. phases, interfaces, common curves and common points);
2. A consistent set of thermodynamic postulates must be used for all microscale quantities;
3. A rigorous change in scale of the governing equations, preserving relations between variables across the scales, is obtained through averaging theorems;

4. Entropy inequality is constrained by means of the product of Lagrange multipliers with conservation equations and differential thermodynamic equations;
5. Values of the Lagrange multipliers are set to be consistent with the detail at which the system will be modeled, leading to an entropy generation rate that is expressed principally in terms of products of forces and fluxes;
6. The entropy generation term is simplified to a form that is written in terms of macroscale forces and fluxes, by means of the use of geometric identities and approximations;
7. The resulting simplified entropy inequality is used to develop specific closure relations that satisfy the conservation laws and the second laws of thermodynamics;
8. Additional constraints can be needed to define the appropriate closure relation at the scale of interest.

2.2.2. Microscale

The first balance equation of the problem is the mass conservation; here it is initially written at the microscale for a chemical species i in the fluid phase, and then it is obtained for the macroscale by applying averaging theorems on the RVE, following the same derivation process introduced by G. Pinder and W. Gray in [21, p. 38].

The rate of change of mass of species i in the reference volume (V) is defined as the sum of the rate of change due to flow of the species across the volume boundary and the rate of change due to transformation from other species (see Figure 2.2):

$$\frac{d}{dt}\int_V \rho_i dv = -\int_S \rho_i \left(\mathbf{v}_\mathrm{i} - \mathbf{w}\right)\cdot \mathbf{n} ds + \int_V r_i dv \tag{2.12}$$

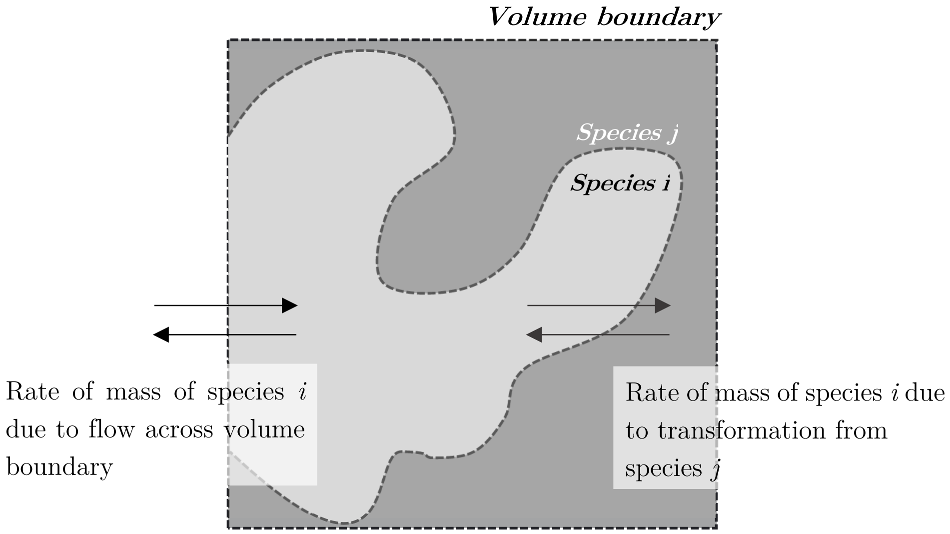

Figure 2.2: Microscale representation of mass balance conservation.

where $\mathbf{v}_i$ is the point velocity of the species i, $\mathbf{n}$ is the normal direction outward from the volume at a point on the boundary surface (S), $\mathbf{w}$ is the velocity of that surface and

$$\rho_i = \rho\omega_i \tag{2.13}$$

is the product of the microscale mass density (ρ) and the fraction of mass of species i (ω_i)

The sum of the mass fraction over the whole different species must give the unit:

$$\sum_i \omega_i = 1 \tag{2.14}$$

As a consequence, the integral of the microscale mass density of the species i over the volume V leads to the total mass of that species in the volume.

By considering (2.12), it clearly states that to have a non-zero flow it is necessary that:

1. Velocity of the species i has a normal component to the boundary surface;
2. Velocity of the species i is different from the boundary surface velocity.

Let us consider now the second term on the right hand side (rhs) of the equation (2.12): it is related to the change of mass due to biological or chemical reactions in the fluid phase; r_i is the *specific rate of mass production of the species i* and it is usually expressed in an approximate way using a specific constitutive relation.

Recalling equation (2.13), (2.12) can be rewritten as:

$$\frac{d}{dt}\int_V \rho\omega_i dv = -\int_S \rho\omega_i \left(\mathbf{v}_\mathrm{i} - \mathbf{w}\right)\cdot \mathbf{n}ds + \int_V r_i dv \tag{2.15}$$

The total conservation of mass for the fluid can be obtained from (2.15) by summing over all the species in the fluid phase as follows:

$$\frac{d}{dt}\int_V \rho dv + \int_S \rho\left(\mathbf{v} - \mathbf{w}\right)\cdot \mathbf{n}ds = 0 \tag{2.16}$$

defining $\mathbf{v}$ as the barycentric velocity of the fluid:

$$\mathbf{v} = \sum_i \mathbf{v}_\mathrm{i}\omega_i \tag{2.17}$$

Due to the fact that r_i is an intraphase term, the summation of r_i over all species is null except when nuclear reactions take place.

A further development of equation (2.15) can be achieved by summing and subtracting $\int_S \rho\omega_i \mathbf{v}\cdot \boldsymbol{n}ds$:

$$\frac{d}{dt}\int_V \rho\omega_i dv = -\int_S \rho\omega_i \left(\mathbf{v} - \mathbf{w}\right)\cdot \mathbf{n}ds - \int_S \rho\omega_i \left(\mathbf{v}_\mathrm{i} - \mathbf{v}\right)\cdot \mathbf{n}ds + \int_V r_i dv \tag{2.18}$$

On the rhs of (2.18), the integral over the boundary surface is split into two components: the first one represents the convection term, whereas the second is the diffusion term. The *convection* term is related to a mass change due to a difference between the average velocity of the fluid and the velocity of the volume surface boundary. The *diffusion* term states instead that there is a rate of change in the mass of the species *i* connected to a difference of the velocity of the species compared to the averaged velocity of the fluid, thanks to the phenomenon of molecules random collision. Two different quantities can be defined here. The diffusive velocity and the diffusion/dispersion term can be written respectively:

$$\mathbf{u}_\mathrm{i} = \mathbf{v}_\mathrm{i} - \mathbf{v} \tag{2.19}$$

$$\mathbf{j_i} = \rho\omega_i \mathbf{u_i} \tag{2.20}$$

We now derive a point formulation of (2.18). Let us apply the transport theorems to the left hand side (lhs) term of (2.18):

$$\int_V \frac{\partial}{\partial t}\left(\rho\omega_i\right)dv + \int_S \rho\omega_i \mathbf{w}\cdot\mathbf{n}ds = -\int_S \rho\omega_i\left(\mathbf{v}-\mathbf{w}\right)\cdot\mathbf{n}ds - \int_S \mathbf{j_i}\cdot\mathbf{n}ds + \int_V r_i dv \tag{2.21}$$

Then, the divergence theorem is applied to the terms of the equation involving integral over the boundary surface and, after some math, it can be obtained:

$$\int_V \left\{\frac{\partial\left(\rho\omega_i\right)}{\partial t} + \left[\nabla\cdot\left(\rho\omega_i\mathbf{v} + \mathbf{j_i}\right) + r_i\right]\right\}dv = 0 \tag{2.22}$$

Because the volume of integration is chosen arbitrarily, we can write:

$$\frac{\partial\left(\rho\omega_i\right)}{\partial t} + \nabla\cdot\left(\rho\omega_i\mathbf{v}\right) + \nabla\cdot\mathbf{j}_i + r_i = 0 \tag{2.23}$$

Equation (2.23) represents the point mass conservation for the species i in the fluid. By summing over all species we obtain the point mass conservation for the entire fluid, which clearly loses information about the concentration of the single species i within the phase:

$$\frac{\partial\rho}{\partial t} + \nabla\cdot\left(\rho\mathbf{v}\right) = 0 \tag{2.24}$$

Equation (2.24) also states the microscopic mass conservation of the solid phase.

The mass conservation equation has been derived extensively. Other microscopic balance equations can be obtained directly starting from the conservation equation within a phase α of a generic conserved variable ψ [28, p. 14]:

$$\frac{\partial\left(\rho\psi\right)}{\partial t} + \nabla\cdot\left(\rho\psi\mathbf{v}_\alpha\right) - \nabla\cdot\mathbf{i} - \rho b = \rho G \tag{2.25}$$

where $\mathbf{v}_\alpha$ is the local value of the velocity field of the α phase at a fixed point in space, $\mathbf{i}$ is the flux vector of ψ, b is the external supply of ψ and G is the net production of ψ.

It is also necessary to define the jump condition at the interface between two constituents α and α' as:

$$\left[\rho\psi\left(\mathbf{w}-\mathbf{v}_{\alpha}\right)+\mathbf{i}\right]\Big|_{\alpha}\cdot\mathbf{n}^{\alpha\alpha'}+\left[\rho\psi\left(\mathbf{w}-\mathbf{v}_{\alpha}\right)+\mathbf{i}\right]\Big|_{\alpha'}\cdot\mathbf{n}^{\alpha'\alpha}=0 \tag{2.26}$$

where $\mathbf{n}^{\alpha\alpha'}$ is the normal outward the α phase into α' phase, defined as:

$$\mathbf{n}^{\alpha\alpha'}=-\mathbf{n}^{\alpha'\alpha} \tag{2.27}$$

and $\Big|_{\alpha}$ means that the quantity on its left must be evaluated in the α phase.

By assigning $\boldsymbol{\psi}=\mathbf{v}_{\alpha}$, $\mathbf{i}=\mathbf{t}_{m}$, $\mathbf{b}=\mathbf{g}$ and $\mathbf{G}=\mathbf{0}$, the momentum balance equation for a phase is reached:

$$\frac{\partial\left(\rho\mathbf{v}_{\alpha}\right)}{\partial t}+\nabla\cdot\left(\rho\mathbf{v}_{\alpha}\otimes\mathbf{v}_{\alpha}\right)-\nabla\cdot\mathbf{t}_{m}-\rho\mathbf{g}=\mathbf{0} \tag{2.28}$$

where $\mathbf{t}_{m}$ is the microscopic stress tensor and $\mathbf{g}$ is the external momentum supply due to gravitational effects.

If we consider instead $\psi=E+\frac{1}{2}\mathbf{v}_{\alpha}\cdot\mathbf{v}_{\alpha}$, $\mathbf{i}=\mathbf{t}_{m}\mathbf{v}_{\alpha}-\mathbf{q}$, $b=\mathbf{g}\cdot\mathbf{v}_{\alpha}$ and $G=0$, we can define the microscopic energy balance:

$$\frac{\partial\left(\rho E+\rho\frac{1}{2}\mathbf{v}_{\alpha}\cdot\mathbf{v}_{\alpha}\right)}{\partial t}+\nabla\cdot\left[\rho\left(E+\frac{1}{2}\mathbf{v}_{\alpha}\cdot\mathbf{v}_{\alpha}\right)\mathbf{v}_{\alpha}\right]-\nabla\cdot\left(\mathbf{t}_{m}\mathbf{v}_{\alpha}\right)-\rho\mathbf{g}\cdot\mathbf{v}_{\alpha}=0 \tag{2.29}$$

where E is the specific intrinsic energy; an isothermal process is considered (heat fluxes and sources are therefore neglected).

Finally, by setting $\psi=\lambda$, $\mathbf{i}=\boldsymbol{\phi}$, $b=s$ and $G=\varphi$, where λ is the specific entropy, $\boldsymbol{\phi}$ is the entropy flux vector, s the intrinsic entropy source and φ is an increase rate of entropy, (2.25) turns into:

$$\frac{\partial\left(\rho\lambda\right)}{\partial t}+\nabla\cdot\left(\rho\lambda\mathbf{v}_{\alpha}\right)-\nabla\cdot\boldsymbol{\phi}-\rho s=\rho\varphi \tag{2.30}$$

2.2.3. Representative elementary volume

Up to this point, the conservation equations were written at the microscale. Let us now introduce the representative elementary volume (RVE), which is the volume used by averaging theorems to average microscale variables at macroscale. As can be seen in Figure 2.3, distinct phases in the RVE are averaged within its volume[5], giving rise to a homogeneous domain, entirely filled by each phase in every point, at the same time.

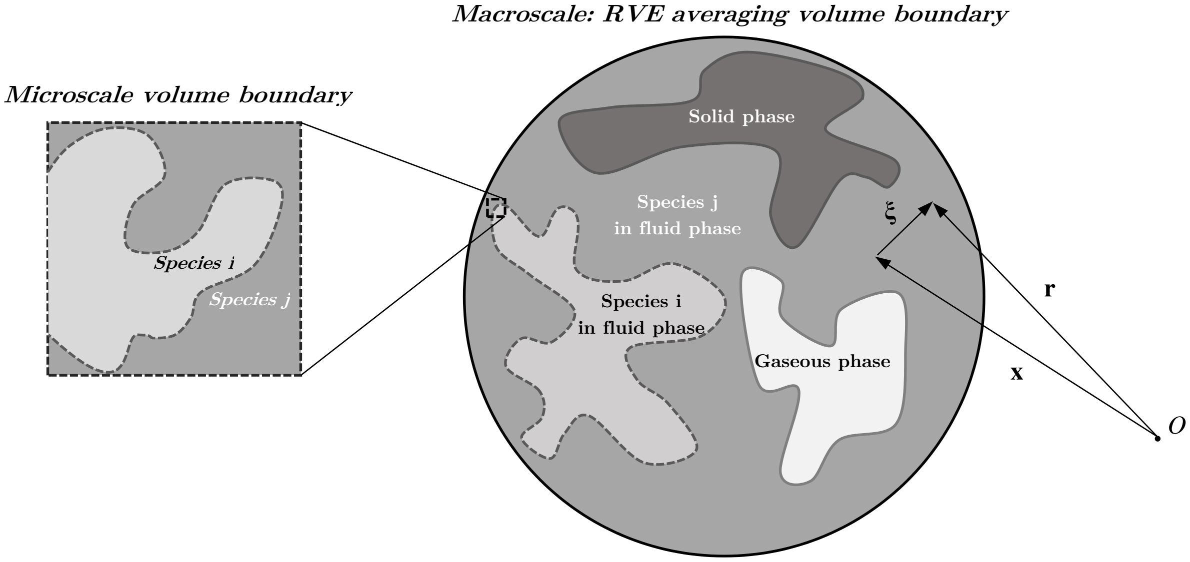

Figure 2.3 Schematic representation of RVE (on the right), in which the averaging process takes place, and a detail of the microscale reference volume (on the left)

As a consequence, the volume fraction of each phase must be defined, to take into account the specific quantity of the single phase within the RVE, though considering it in a continuous fashion.

The size of an RVE must be chosen appropriately: it must be large enough to include heterogeneities of the medium, in order to free average quantities from fluctuations,

---

[5] In Figure 2.3 RVE is represented before the application of the averaging process, with separate phases. After the averaging procedure, no sharp interfaces can be found within the RVE.

depending on RVE size. Also it must be small enough to be considered infinitesimal, to prevent partial derivatives in governing equations from losing sense [28, p. 11].

2.2.4. Averaging process and macroscopic variables

It is necessary to set up the stage for the transformation between different scales. Therefore, now we consider a multiphase system of volume δV and boundary surface A, made of different phases $\boldsymbol{\alpha}$ of volume δV^{α}. Let us consider each point of the volume coincident with the centroid of an REV: it can be possible to define a global coordinate system, which locates the specific position of the REV (by vector $\mathbf{x}$), and a local coordinate system, relative to REV centroid, that locates the points inside the RVE (by vector $\boldsymbol{\xi}$).

The position of a point (or a microscopic volume element dv_m) within the representative elementary volume can be then expressed by vector $\mathbf{r}$ as (see Figure 2.3):

$$\mathbf{r} = \mathbf{x} + \boldsymbol{\xi} \tag{2.31}$$

Referring to this coordinate system, the total volume of a phase $\boldsymbol{\alpha}$ in the RVE is:

$$\delta V^{\alpha}\left(\mathbf{x}, t\right) = \int_{\delta V^{\alpha}} dv_m \tag{2.32}$$

denoting a macroscale quantity with a superscript letter, whereas a microscale variable with subscript.

If we define the *phase-distribution function* as [28, p. 11]:

$$\gamma^{\alpha}\left(\mathbf{r}, t\right) = \begin{cases} 1 \text{ for } \mathbf{r} \in \delta V^{\alpha} \\ 0 \text{ for } \mathbf{r} \notin \delta V^{\alpha} \end{cases} \tag{2.33}$$

equation (2.32) can be rewritten as:

$$\delta V^{\alpha}\left(\mathbf{x}, t\right) = \int_{\delta V} \gamma^{\alpha}\left(\mathbf{r}, t\right) dv_m \tag{2.34}$$

Using (2.34), we can finally obtain the volume fraction for the phase $\boldsymbol{\alpha}$ as:

$$\varepsilon^\alpha\left(\mathbf{x},t\right)=\frac{\delta V^\alpha\left(\mathbf{x},t\right)}{\delta V}=\frac{1}{\delta V}\int_{\delta V}\gamma^\alpha\left(\mathbf{r},t\right)dv_m \tag{2.35}$$

Noting that the sum of all the volume phases gives the total volume and considering a system made of solid (s), liquid (w) and gaseous (g) phases, the sum of the volume fractions gives the unit, as follows:

$$\varepsilon^s+\varepsilon^w+\varepsilon^g=1 \tag{2.36}$$

Equations from (2.32) to (2.36) are fundamental in the transformation process from the microscale to the macroscale. With these relations at hand, let us now define some macroscale quantities. The following variables can be obtained by means of the averaging operator, defined by W. Gray and T. Miller in [24], defined as follows:

$$\left\langle P_\alpha\right\rangle_{\Omega_\beta,\Omega_\gamma,W}=\frac{\int_{\Omega_\beta}WP_\alpha dv}{\int_{\Omega_\gamma}Wdv}\quad\text{for }\dim\Omega_\beta>0,\ \dim\Omega_\gamma>0 \tag{2.37}$$

where P_α is a microscale property of phase α to be averaged, W is a weighting function (equal to 1 if not differently specified), Ω_β is the domain of integration of P_α and Ω_γ is the region of integration used in normalizing the averaging process.

We can then start with mass density in the $\boldsymbol{\alpha}$ phase:

$$\rho^\alpha\left(\mathbf{x},t\right)=\left\langle\rho_\alpha\right\rangle_{\Omega_\alpha,\Omega_\alpha}=\frac{1}{\delta V^\alpha\left(\mathbf{x},t\right)}\int_{\delta V}\rho\left(\mathbf{r},t\right)\gamma^\alpha\left(\mathbf{r},t\right)dv_m \tag{2.38}$$

This equation can be also expressed, recalling equation (2.35), in an equivalent way as:

$$\varepsilon^\alpha\left(\mathbf{x},t\right)\rho^\alpha\left(\mathbf{x},t\right)=\left\langle\rho_\alpha\right\rangle_{\Omega_\alpha,\Omega}=\frac{1}{\delta V}\int_{\delta V}\rho\left(\mathbf{r},t\right)\gamma^\alpha\left(\mathbf{r},t\right)dv_m \tag{2.39}$$

where Ω is the entire averaging volume.

The second quantity to be considered is the mass density of the species i within the α phase, which can be defined as follows, bearing equation (2.13) in mind:

$$\rho^{\alpha}\left(\mathbf{x},t\right)\omega^{i\alpha}\left(\mathbf{x},t\right)=\left\langle \rho_{\alpha}\omega_{i\alpha}\right\rangle_{\Omega_{\alpha},\Omega_{\alpha}}=\frac{1}{\delta V^{\alpha}\left(\mathbf{x},t\right)}\int_{\delta V}\rho\left(\mathbf{r},t\right)\gamma^{\alpha}\left(\mathbf{r},t\right)dv_{m}$$

(2.40)

or similarly:

$$\varepsilon^{\alpha}\left(\mathbf{x},t\right)\rho^{\alpha}\left(\mathbf{x},t\right)\omega^{i\alpha}\left(\mathbf{x},t\right)=\left\langle \rho_{\alpha}\omega_{i\alpha}\right\rangle_{\Omega_{\alpha},\Omega}=\frac{1}{\delta V}\int_{\delta V}\rho\left(\mathbf{r},t\right)\omega_{i}\left(\mathbf{r},t\right)\gamma^{\alpha}\left(\mathbf{r},t\right)dv_{m}$$

(2.41)

A worthwhile observation can be done by summing over all the species in (2.41) and applying both (2.14) and (2.39):

$$\sum_{i}\omega^{i\alpha}=1 \tag{2.42}$$

Equation (2.42) assures that both at microscale and macroscale the sum of all the mass fractions of the species in the phase gives the unit.

The third macroscale variable to define is the velocity of the species i in the phase α, that can be obtained from the momentum equation for the species using (2.35):

$$\varepsilon^{\alpha}\left(\mathbf{x},t\right)\rho^{\alpha}\left(\mathbf{x},t\right)\omega^{i\alpha}\left(\mathbf{x},t\right)\mathbf{v}^{i\alpha}\left(\mathbf{x},t\right)=\left\langle \rho_{\alpha}\omega_{i\alpha}\mathbf{v}_{i\alpha}\right\rangle_{\Omega_{\alpha},\Omega}=\frac{1}{\delta V}\int_{\delta V}\rho\left(\mathbf{r},t\right)\omega_{i}\left(\mathbf{r},t\right)\mathbf{v}_{i}\left(\mathbf{r},t\right)\gamma^{\alpha}\left(\mathbf{r},t\right)dv_{m}$$

(2.43)

Following the same strategy for (2.42) it is possible to introduce the *barycentric macroscale phase velocity* $\mathbf{v}^{\alpha}$:

$$\mathbf{v}^{\alpha}=\sum_{i}\omega^{i\alpha}\mathbf{v}^{i\alpha} \tag{2.44}$$

Analogously to the definition at microscale through (2.20), the macroscale diffusion/dispersion term can be written as:

$$\mathbf{j}^{i\alpha}=\rho\omega^{i\alpha}\mathbf{u}^{i} \tag{2.45}$$

with:

$$\mathbf{u}^{i\alpha}=\mathbf{v}^{i\alpha}-\mathbf{v}^{\alpha} \tag{2.46}$$

Finally, we define the chemical rate of mass production for the species *i*, by integrating r_i at the microscale within δV:

$$\varepsilon^{\alpha}\left(\mathbf{x},t\right)r^{i\alpha}\left(\mathbf{x},t\right)=\left\langle r_{i\alpha}\right\rangle_{\Omega_{\alpha},\Omega}=\frac{1}{\delta V}\int_{\delta V} r_{i}\left(\mathbf{r},t\right)\gamma^{\alpha}\left(\mathbf{r},t\right)dv_{m} \tag{2.47}$$

2.2.5. Macroscale

After defining the macroscale variables, we now write the conservation equations at the macroscale, obtained from microscale conservations by using averaging theorems of TCAT [24]. Three different group of theorems are developed by Gray and Miller to deal with averaging of divergence, gradient and partial time derivative operations. Here we do not derive the entire set of equations, interested reader can find a full derivation of the equations in [25].

I. *Mass conservation*

The averaging of microscale balance equation of the species dispersed within the phase α leads to the macroscale mass conservation:

$$\mathcal{M}^{i\alpha}:=\frac{\partial\left(\varepsilon^{\alpha}\rho^{\alpha}\omega^{i\alpha}\right)}{\partial t}+\nabla\cdot\left(\varepsilon^{\alpha}\rho^{\alpha}\omega^{i\alpha}\mathbf{v}^{i\alpha}\right)-\varepsilon^{\alpha}r^{i\alpha}-\sum_{\kappa\in\Im_{c\alpha}}\overset{i\kappa\rightarrow i\alpha}{M}=0 \tag{2.48}$$

where the meaning of the terms in the equation were defined in §2.2.4. Considering the last two terms of the equation, $\varepsilon^{\alpha}r^{i\alpha}$ is an intraphase mass exchange term due to reaction between species within the phase, whereas $\sum_{\kappa\in\Im_{c\alpha}}\overset{i\kappa\rightarrow i\alpha}{M}$ stands for an interphase mass exchange of the species through separation interface.

By considering instead the conservation of the entire phase α , equation (2.48) becomes:

$$\mathcal{M}^{\alpha}:=\frac{\partial\left(\varepsilon^{\alpha}\rho^{\alpha}\right)}{\partial t}+\nabla\cdot\left(\varepsilon^{\alpha}\rho^{\alpha}\mathbf{v}^{i\alpha}\right)-\sum_{\kappa\in\Im_{c\alpha}}\overset{\kappa\rightarrow\alpha}{M}=0 \tag{2.49}$$

where $\sum_{\kappa\in\Im_{c\alpha}} \overset{\kappa\rightarrow\alpha}{M}$ is again an interphase exchange term of mass between one phase to another ($\sum_{\kappa\in\Im_{c\alpha}} \left(\; \right)$ stands for the summation over all the phases exchanging mass at the interfaces with the phase α).

The second term of the equation can be split, analogously to what it was done at microscale in §2.2.2, by applying (2.46) and introducing the diffusive term:

$$\frac{\partial\left(\varepsilon^{\alpha}\rho^{\alpha}\right)}{\partial t} + \nabla\cdot\left(\varepsilon^{\alpha}\rho^{\alpha}\mathbf{v}^{\alpha}\right) + \nabla\cdot\left(\varepsilon^{\alpha}\rho^{\alpha}\mathbf{u}^{i\alpha}\right) - \sum_{\kappa\in\Im_{c\alpha}} \overset{\kappa\rightarrow\alpha}{M} = 0 \tag{2.50}$$

where $\mathbf{u}^{i\alpha}$ is the diffusive velocity of the species i.

II. Conservation of Momentum

By applying the averaging technique, the momentum balance of the phase α comprising different species i can be stated as:

$$\mathcal{P}^{\alpha} := \frac{\partial\left(\varepsilon^{\alpha}\rho^{\alpha}\mathbf{v}^{\alpha}\right)}{\partial t} + \nabla\cdot\left(\varepsilon^{\alpha}\rho^{\alpha}\mathbf{v}^{\alpha}\mathbf{v}^{\alpha}\right) - \varepsilon^{\alpha}\rho^{\alpha}\mathbf{g}^{\alpha} - \nabla\cdot\left(\varepsilon^{\alpha}\mathbf{t}^{\alpha}\right) - \sum_{\kappa\in\Im_{c\alpha}}\left(\sum_{i\in\Im_{s}} \overset{i\kappa\rightarrow i\alpha}{M}_{v}\,\mathbf{v}^{\alpha} + \overset{\kappa\rightarrow\alpha}{\mathbf{T}}\right) = \mathbf{0} \tag{2.51}$$

where $\mathbf{g}^{\alpha}$ is the body force, $\mathbf{t}^{\alpha}$ is the stress tensor, $\overset{i\kappa\rightarrow i\alpha}{M}_{v}\,\mathbf{v}^{\alpha}$ is the momentum exchange between phases thanks to mass exchange of the species i, $\overset{\kappa\rightarrow\alpha}{\mathbf{T}}$ is the interaction force between phase α and the adjacent interfaces. By considering interface properties negligible, this term represents the interaction forces between phases.

Furthermore, if the time scales of the problem allows it and small velocities are at stake, inertial term and the contribution of momentum exchange $\overset{i\kappa\rightarrow i\alpha}{M}_{v}\,\mathbf{v}^{\alpha}$ become negligible, equation (2.51) turns into:

$$\varepsilon^{\alpha}\rho^{\alpha}\mathbf{g}^{\alpha} + \nabla\cdot\varepsilon^{\alpha}\mathbf{t}^{\alpha} + \sum_{\kappa\in\Im_{c\alpha}} \overset{\kappa\to\alpha}{\mathbf{T}} = 0 \tag{2.52}$$

III. Conservation of Energy

A macroscopic averaged equation for the conservation of energy of the phase α can be written as[6]:

$$\begin{aligned} \mathcal{E}^{\alpha} = {} & \frac{\partial}{\partial t}\left(E^{\alpha} + \frac{1}{2}\varepsilon^{\alpha}\rho^{\alpha}\mathbf{v}^{\alpha}\cdot\mathbf{v}^{\alpha} + \varepsilon^{\alpha}\rho^{\alpha}K_{E}^{\alpha} + \varepsilon^{\alpha}\rho^{\alpha}\psi_{g}^{\alpha}\right) + \\ & +\nabla\cdot\left[\left(E^{\alpha} + \frac{1}{2}\varepsilon^{\alpha}\rho^{\alpha}\mathbf{v}^{\alpha}\cdot\mathbf{v}^{\alpha} + \varepsilon^{\alpha}\rho^{\alpha}K_{E}^{\alpha} + \varepsilon^{\alpha}\rho^{\alpha}\psi_{g}^{\alpha}\right)\mathbf{v}^{\alpha}\right] + \\ & -\nabla\cdot\varepsilon^{\alpha}\mathbf{t}^{\alpha}\cdot\mathbf{v}^{\alpha} - \sum_{\kappa\in\Im_{c\alpha}}\left(\overset{\kappa\to\alpha}{M}_{E} + \overset{\kappa\to\alpha}{\mathbf{T}}_{v}\right) = 0 \end{aligned} \tag{2.53}$$

where E^{α} is the internal energy, K_{E}^{α} is the kinetic energy due to microscale velocity fluctuations, ψ_{g}^{α} is the gravitational potential and $\overset{\kappa\to\alpha}{M}_{E}$, $\overset{\kappa\to\alpha}{\mathbf{T}}_{v}$ are the transfer of energy from the interface $\kappa\alpha$ to the α phase for a phase change.

The entropy inequality is introduced in §4.1 to derive the Darcy's law.

---

[6] An isothermal process is considered. Thus, all terms involving heat transfer are neglected.

3. Biomechanical Applications

In this chapter we will focus on the development of computational models, by applying the Theory of Porous Media and Diffusion to different biomechanical research fields, namely the diabetic foot and the scaffold for spinal fusion and articular defect repair. This work is a reply to clinician and biologist need of having a numerical tool, which could assist them in a better comprehension and prediction of biomechanical and biomedical phenomena.

3.1. The Diabetic foot

3.1.1. Etiology of diabetes mellitus

Diabetes is a chronical disease, which is characterized by high levels of glucose in the blood. There are two main types of diabetes. The “type 1” is caused by an autoimmune disease that destroys the beta cells of pancreas [29], [30]. These beta cells have the function of producing insulin, an hormone that leads to the uptake of glucose from blood by peripheral tissues (most of all muscle and adipose tissue), in order to be used as energy source. Without insulin, the glucose remains in the blood and makes chemical reactions that damage different tissues. This kind of diabetes is also known as “juvenile diabetes” [29], because of its early onset, and all-life long therapy with insulin is mandatory.

The “type 2” diabetes has complicated pathology causes, because it is mainly due to a peripheral resistance to insulin action. Only in the latest part of the disease, a lack of insulin is recorded, because insufficient production of beta cells by pancreas. This kind of diabetes has usually a familiar pathogenesis and appears in adults and old people. While the type 1 has a sudden appearance, the type 2 has a silent appearance, so usually it is diagnosed when chronical damages have already developed.

The complications of diabetes can become really severe; the pathogenesis is characterized by damages in vessels and nerves, for this reason all organs are potentially involved. The major manifestations are retinopathy, nephropathy, cardiovascular diseases, diabetic neuropathy and the diabetic foot [31].

Concerning this last complication, both vascular and peripheral nervous damages are involved in the formation of ulcers in the foot. The loss of the sensitivity and the death of most peripheral nerves [32] are key factors in determining vulnerabilities to trauma, which direct consequence is the foot ulceration triggering. While the loss of the protective sensation of pain allows the ulcer to rapidly grow, the reduced blood flux adversely affects the process of wound healing, often preventing the damaged tissue regeneration.

This phenomenon is generally amplified by another complication of the disease: an excessive plantar pressure. The limited joint mobility, caused by the progressive stiffening of the collagen-containing tissues [33], [34], as well as the deformities of the foot, are responsible for peaks in plantar pressures [35], [36], which lead to foot ulceration. In addition, the tissues recovered after an ulceration are weakened (e.g. by the formation of scar tissue or incomplete remodeling of skin [37]) and, as a consequence, are more sensitive to following relapses.

In a strategy of prevention of the foot ulceration, first clinicians can operate by inspecting for peripheral vascular disease and for the nerve conduction state, to assess the condition of the foot and to schedule a set of medical examination checkups. Second, if excessive pressure peaks are revealed, off-loading intervention strategies should be realized, by using orthotics or patient specific footwear, to efficiently spread the body weight on larger areas of contact with the ground.

Though the ulcer formation is sensitive of elevated contact pressure at the interface tissue-floor [38], the ulceration triggering often takes place within the tissue, where stress peaks reach higher values, particularly at the interfaces of tissue-bone angularities [39], [40] (calcaneus and metatarsal head).

Therefore, the measurement of stresses is of paramount importance in the prediction of ulceration risk. Common biomedical experimental setup allows to measure only some variables *in-vivo*, such as the plantar pressures, the ground forces and the kinematic of the foot during gait cycle. Also the geometry of the foot can be achieved by image processing of magnetic resonance imaging (MRI) and computed tomography (CT), while internal stress field in the tissue remains unknown.

These limitations can be overcome by *in silico* tests. Numerical models allows to mimic the behavior of the foot during gait cycles, permitting to study the values of the stress state in the whole domain of interest, for the entire foot. In this way, by computer simulations it is possible to take advantage of the experimental inputs (i.e. loading paths, geometry and materials) and provide clinicians with valuable information that cannot be achieved *in-vivo*.

3.1.2. Introduction to the work

The model shown in this thesis is the result of a collaboration with *DEI* research group. This valuable partnership allowed us to join together different team skills, coming from specific expertise built up over years. In particular, it was possible to efficiently take advantage of the deep knowledge of diabetes pathology as well as the gained experimental data (i.e. subject specific forces, pressures, kinematics and geometry) coming from prof. Cobelli's group. They were efficaciously applied to a long-standing research activity on porous media as well as numerical and finite element knowledge, conducted by *DICEA* team.

In this chapter we apply the porous media constitutive behavior to plantar tissue. The first innovation introduced is the concept of time: contrarily to previous state-of-the-art modeling (e.g. linear elastic or hyperelastic constitutive behavior [41]–[43]), time here becomes a variable with a real physical significance. The poroelastic behavior used allows to consider the specific duration and structure of the gait cycle, measured from the patient. The development of the walk is studied with continuity all along its duration, not only at some specific time frames by applying an equivalent static loading configuration (see e.g. [9], [43], [44]). The second advance concerns the stress field: the poroelastic behavior used allows splitting the stresses in the tissues into effective stresses (in the solid skeleton) and the interstitial fluid pressure. With cyclic loadings (e.g. the gait cycles) the fluid-structure interaction phenomenon gradually takes place, transferring progressively the stresses from the fluid to the solid phase of the medium. The result is an increasing value of the effective stresses as the number of steps increases. In this phenomenon can be found the focal point of our choice: we effectively believe that ulcer initiation and evolution is linked to the excess of effective stresses with reference to a threshold value. As a consequence, the ulceration risk increases with the number of steps executed, as the fluid-structure interaction phenomenon progresses. All of these concepts will be extensively studied in the numerical results section of this work.

The mathematical model of the plantar tissue was developed with the valuable support of my team (*DICEA team*). My work finds its foundation from the model firstly introduced by Dr. G. Sciumè. In his work he applied the Porous Media Theory to different biological fields of application: initially the tumor growth [11], [13], [27] and then the plantar tissue of the foot [45]–[48]. Starting from his worthwhile initial work, I developed a new model with additional features and improvements (hyperelastic behavior of the solid skeleton, patient specific input data, large rotations/deformations regime, different geometry and behavior for healthy and diabetic feet [49], the onset and the development of the ulceration process with the introduction of an ulceration risk threshold variable).

In the next paragraph, the model will be explained in detail and the concepts developed in the general theory of porous medium (see §2.1) will be adapted to the specific field of application of this section: the diabetic foot.

3.1.3. The mathematical model of the plantar tissue

In this framework the soft tissue of the foot is modelled as a porous medium, made of a solid phase (the tissue cells and the extracellular matrix (ECM)) that is fully saturated by the interstitial fluid. According to (2.36), the sum of volume ratios of the two phases is:

$$\varepsilon^{s} + \varepsilon^{f} = 1 \tag{3.1}$$

Due to the fact that the whole pores are filled by fluid, the porosity can be defined as the volume ratio of the fluid phase:

$$\varepsilon = \varepsilon^{f} = 1 - \varepsilon^{s} \tag{3.2}$$

The fundamental governing equations of our model are: the mass conservation for the medium and the linear momentum balance equation.

The mass conservation of the solid phase is obtained starting from (2.48) by neglecting the diffusion term in the solid phase (it is commonly very slow, according to [21, p. 176]). The ulceration phenomenon is modelled by the transformation of a fraction of the solid phase (i.e. the healthy cells and the ECM) into another one (i.e. the ulcerated cells and the ECM). Thus, due to the presence of two different species, the solid phase conservation law splits into two contributions: the first, containing the mass fraction of the healthy cells and the second, containing the ulcerated cells and a dissolution term (see Figure 3.1):

$$\frac{\partial\left(\varepsilon^{s}\rho^{s}\omega^{Hs}\right)}{\partial t} + \nabla\cdot\left(\varepsilon^{s}\rho^{s}\omega^{Hs}\mathbf{v}^{s}\right) + \varepsilon^{s}r^{Us} = 0 \tag{3.3}$$

$$\frac{\partial\left(\varepsilon^{s}\rho^{s}\omega^{Us}\right)}{\partial t} + \nabla\cdot\left(\varepsilon^{s}\rho^{s}\omega^{Us}\mathbf{v}^{s}\right) - \varepsilon^{s}r^{Us} + \overset{Us\to f}{M} = 0 \tag{3.4}$$

where ω^{Hs} is the mass fraction of the healthy cells, whereas ω^{Us} is the ulcerated counterpart.

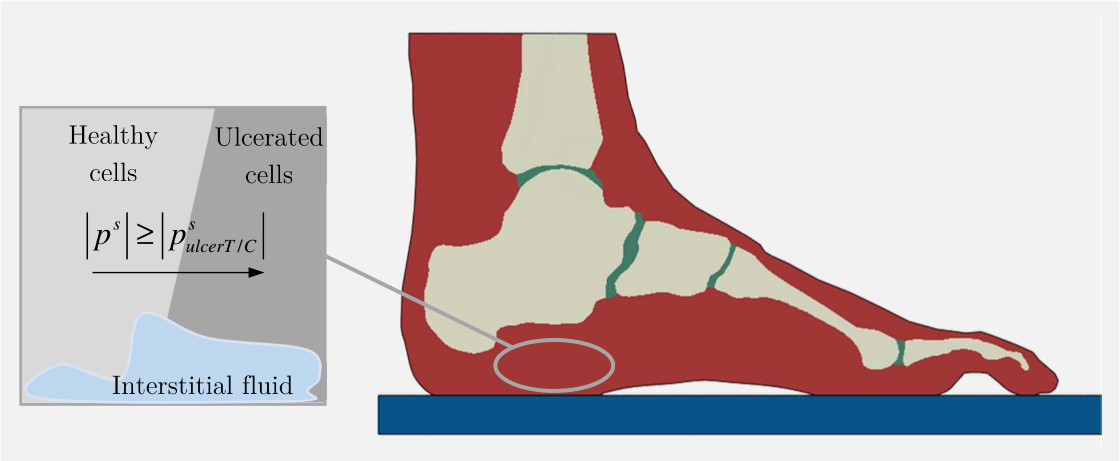

Figure 3.1 Schematization of phases in the plantar tissue and the rationale at the base of ulceration phenomenon.

The term $\varepsilon^s r^{Us}$ is an intraphase mass exchange term, which represents the rate of transformation of healthy cells into ulcerated, when a threshold pressure is exceeded. A constitutive relation for this term can be expressed using the relation in Preziosi and Vitale [50], [51], properly modified by defining different ulceration threshold pressures at traction p^s_{ulcerT} and compression p^s_{ulcerC} :

$$\varepsilon^s r^{Us} = \delta H\left(\left|p^s\right| - \left|p^s_{ulcerT/C}\right|\right)\left(1 - \omega^{Us}\right)\varepsilon^s \tag{3.5}$$

where δ is an additional ulceration factor due to pressure excess, p^s is the average pressure defined as $tr\left(\boldsymbol{\sigma}'\right)/3$ (see §3.1.3 and §3.1.8.2 for further details), the Heaviside function is:

$$H\left(\left|p^s\right| - \left|p^s_{ulcerT/C}\right|\right) = \begin{cases} 1 \text{ if } \begin{cases} p^s \geq 0, \left|p^s\right| \geq \left|p^s_{ulcerT}\right| \\ or \\ p^s \leq 0, \left|p^s\right| \geq \left|p^s_{ulcerC}\right| \end{cases} \\ 0 \text{ if } p^s_{ulcerC} < p^s < p^s_{ulcerT} \end{cases}$$

where $p^s_{ulcerT/C}$ is the threshold pressure at traction or compression, depending on the sign of p^s.

The transformation of the necrotic cells from solid to liquid is also considered. This process is called *dissolution*, and usually it takes place after necrosis has occurred.

It is convenient to rewrite equation (3.4) in the material frame reference. Let us split the divergence term by applying the chain rule, after having divided for the constant mass density of the solid (by considering variation of densities in time and space negligible ($\varepsilon^s \frac{\partial\left(\rho^s\right)}{\partial t}=0$; $\varepsilon^s\mathbf{v}^s\cdot\nabla\rho^s=0$)), as:

$$\nabla\cdot\left(\varepsilon^s\omega^{Us}\mathbf{v}^s\right)=\mathbf{v}^s\cdot\nabla\left(\varepsilon^s\omega^{Us}\right)+\varepsilon^s\omega^{Us}\,\nabla\cdot\left(\mathbf{v}^s\right) \tag{3.6}$$

If we use the material derivative definition[7], (3.4) becomes:

$$D^s\left(\varepsilon^s\omega^{Us}\right)+\varepsilon^s\omega^{Us}\,\nabla\cdot\left(\mathbf{v}^s\right)-\frac{1}{\rho^s}\left(\varepsilon^s r^{Us}-\overset{Us\to f}{M}\right)=0 \tag{3.7}$$

If we consider the material derivative of the Jacobian determinant, it is possible to write:

$$\dot{J}=J\,\nabla\cdot\mathbf{v}^s \tag{3.8}$$

By passing to the material reference frame, and applying the chain rule, (3.7) becomes:

$$\frac{\partial}{\partial t}\left(\varepsilon^s\omega^{Us}J\right)-\frac{J}{\rho^s}\left(\varepsilon^s r^{Us}-\overset{Us\to f}{M}\right)=0 \tag{3.9}$$

Reapplying the chain rule to the first term of equation (3.9) leads to:

$$-\omega^{Us}\frac{J}{\rho^s}\overset{Us\to f}{M}+\varepsilon^s J\frac{\partial}{\partial t}\left(\omega^{Us}\right)-\frac{J}{\rho^s}\left(\varepsilon^s r^{Us}-\overset{Us\to f}{M}\right)=0 \tag{3.10}$$

where the first term of (3.10) is obtained from the mass conservation for the solid phase[8]:

---

[7] $D^s\left(\varepsilon^s\omega^{Us}\right)=\frac{\partial\left(\varepsilon^s\omega^{Us}\right)}{\partial t}+\mathbf{v}^s\cdot\nabla\left(\varepsilon^s\omega^{Us}\right)$, where $D^s\left(f\right)$ is the material derivative of the function f.

[8] (3.11) is obtained starting from the sum of both (3.3) and (3.4), using a similar strategy to the one used here to derive the equation for ω^{Us}:

$$\frac{\partial\varepsilon^s}{\partial t}+\nabla\cdot\left(\varepsilon^s\mathbf{v}^s\right)=-\frac{1}{\rho^s}\overset{Us\to f}{M}$$

$$\frac{\partial\varepsilon^s}{\partial t}+\mathbf{v}^s\cdot\nabla\left(\varepsilon^s\right)+\varepsilon^s\,\nabla\cdot\left(\mathbf{v}^s\right)=-\frac{1}{\rho^s}\overset{Us\to f}{M}$$, here the material derivative is identified:

$$\frac{\partial}{\partial t}\left(\varepsilon^{s} J\right)=\frac{J}{\rho^{s}}\overset{Us\to f}{M} \tag{3.11}$$

After some math we finally obtain the equation of the ulcerated cell mass fraction evolution in the material reference frame:

$$\frac{\partial \omega^{Us}}{\partial t}=\frac{1}{\rho^{s}\varepsilon^{s}}\left(\varepsilon^{s} r^{Us}+\left(\omega^{Us}-1\right)\overset{Us\to f}{M}\right) \tag{3.12}$$

We now address the mass conservation of a species i (e.g. the nutrient of the cells, the oxygen, etc.) in the fluid phase. Starting from equation (2.48), applying (2.46) and assuming no intraphase mass exchange rate, we finally obtain:

$$\frac{\partial\left(\varepsilon^{f}\rho^{f}\omega^{if}\right)}{\partial t}+\nabla\cdot\left(\varepsilon^{f}\rho^{f}\omega^{if}\mathbf{v}^{f}\right)+\nabla\cdot\left(\varepsilon^{f}\rho^{f}\omega^{if}\mathbf{u}^{if}\right)+\overset{if\to is}{M}=0 \tag{3.13}$$

where $\overset{if\to is}{M}$ is an interphase mass exchange term of the species *"i"*.

Considering now the diffusive/dispersive term, by recalling the first Fick's law (2.1) the diffusion process is guided at the microscale by a concentration gradient. It is commonly accepted in multiphase flow theory to substitute the concentration with the mass fraction of the species i in the phase. If we also consider the diffusion term in (2.45) as the rate of transfer per unit area in (2.1), we can get:

$$\varepsilon^{f}\mathbf{j}^{if}=\rho^{f}\omega^{if}\mathbf{D}_{eff}\cdot\nabla\omega^{if} \tag{3.14}$$

Equation (3.13) can be then rewritten as:

$$\frac{\partial\left(\varepsilon^{f}\rho^{f}\omega^{if}\right)}{\partial t}+\nabla\cdot\left(\varepsilon^{f}\rho^{f}\omega^{if}\mathbf{v}^{f}\right)+\rho^{f}\omega^{if}\mathbf{D}_{eff}\cdot\nabla\omega^{if}+\overset{if\to is}{M}=0 \tag{3.15}$$

By summing the mass balance for all the species both in the solid and fluid phase, we can write the mass conservation for the entire medium:

$D^{s}\varepsilon^{s}+\varepsilon^{s}\frac{\dot{J}}{J}=-\frac{1}{\rho^{s}}\overset{Us\to f}{M}$, then we pass to material reference frame:

$J\dot{\varepsilon}^{s}+\varepsilon^{s}\dot{J}=-\frac{J}{\rho^{s}}\overset{Us\to f}{M}$, and by considering the chain rule:

$\frac{\partial}{\partial t}\left(\varepsilon^{s} J\right)=-\frac{J}{\rho^{s}}\overset{Us\to f}{M}$

$$\frac{\partial\left(\varepsilon^f+\varepsilon^s\right)}{\partial t}+\nabla\cdot\left(\varepsilon^f\mathbf{v}^f\right)+\nabla\cdot\left(\varepsilon^s\mathbf{v}^s\right)=\left(\frac{1}{\rho^f}-\frac{1}{\rho^s}\right)\overset{s\to f}{M} \tag{3.16}$$

where $\overset{s\to f}{M}=\overset{Us\to f}{M}=-\sum_i\overset{if\to is}{M}$ and variation of densities in time and space are assumed negligible: ($\varepsilon^f\frac{\partial\left(\rho^f\right)}{\partial t}=\varepsilon^s\frac{\partial\left(\rho^s\right)}{\partial t}=0$; $\varepsilon^s\mathbf{v}^s\cdot\nabla\rho^s=\varepsilon^f\mathbf{v}^f\cdot\nabla\rho^f=0$).

From [10] (see appendix §4.1), by neglecting inertial term, the Darcy velocity $\mathbf{q}$ can be written as:

$$\mathbf{q}=\varepsilon\left(\mathbf{v}^f-\mathbf{v}^s\right)=-\frac{\mathbf{k}}{\mu^f}\nabla p^f \tag{3.17}$$

where $\mathbf{k}$ is the permeability, μ^f the viscosity of the fluid and p^f the interstitial fluid pressure.

By substituting equation (3.17) into (3.16) we can obtain the final mass conservation equation written in spatial frame:

$$\nabla\cdot\mathbf{v}^s+\nabla\cdot\left(\mathbf{q}\right)=\Delta m\,\overset{s\to f}{M} \tag{3.18}$$

having defined $\Delta m=\frac{1}{\rho^f}-\frac{1}{\rho^s}$.

Let us now derive the equation for the material reference frame. It is possible to start with the transformation of the gradient operator from material to spatial frame:

$$\nabla f=\nabla_X f\,\mathbf{F}^{-1}=\mathbf{F}^{-\mathrm{T}}\nabla_X f\ ^{9} \tag{3.19}$$

where f is a scalar function and $\mathbf{F}$ is the deformation gradient.

The transformation of the gradient operator between reference frames can be obtained by using the *Piola Transform* after having defined the *Piola identity* (ref. [52, p. 7]):

$$\nabla_X\cdot\mathbf{W}=J\,\nabla\cdot\mathbf{w} \tag{3.20}$$

---

[9] The divergence operator $\nabla_X\cdot\left(\ \right)$ and the gradient operator $\nabla_X\left(\ \right)$ defined in the material frame is marked by the subscript X. Their spatial counterparts, conventionally written with x subscript, are written here for simplicity without any subscript.

where $\mathbf{W}\left(X,t\right) = J\,\mathbf{F}^{-1}\mathbf{w}\left(x,t\right)$, with $\mathbf{w}$ a vector function of $\left(x,t\right)$.

If we also define $\mathbf{Q}$ as:

$$\mathbf{Q} = J\,\mathbf{F}^{-1}\mathbf{q} \tag{3.21}$$

we finally can write the mass conservation of the medium in the material reference frame as:

$$\dot{J} - J\,\nabla_X \cdot \left(\frac{\mathbf{k}}{\mu^f}\mathbf{C}^{-1}\nabla_X\, p^f \right) = J\Delta m\, \overset{s\to f}{M} \tag{3.22}$$

where $\mathbf{C}$ is the Right Cauchy-Green tensor.

Let us now focus on the linear momentum balance equation. First, we need to define the stress tensor for the solid $\left(\mathbf{t}^s\right)$ (3.23) and for the fluid phase $\left(\mathbf{t}^f\right)$ (3.24), as in [53]:

$$\mathbf{t}^s = \mathbf{t}^s_e - \mathbf{I}\,\alpha_B p^f \tag{3.23}$$

$$\mathbf{t}^f = -\mathbf{I}\,\alpha_B p^f \tag{3.24}$$

where $\mathbf{t}^s_e$ is the effective stress of the solid phase, $\mathbf{I}$ is a second order unit tensor, α_B is the Biot's coefficient [54] and p^f is the interstitial fluid pressure.

From (2.52), neglecting the body forces and summing together solid and fluid phase contribution, we obtain the linear momentum balance equation:

$$\nabla \cdot \left[\left(1-\varepsilon\right)\mathbf{t}^s_e - \mathbf{I}\,\alpha_B p^f \right] = 0 \tag{3.25}$$

or $\nabla \cdot \boldsymbol{\sigma} = 0$, where $\boldsymbol{\sigma}$ is the Cauchy stress tensor.

If we define the effective stress tensor as:

$$\boldsymbol{\sigma}' = \left(1-\varepsilon\right)\mathbf{t}^s_e \tag{3.26}$$

equation (3.26) becomes:

$$\nabla \cdot \left[\boldsymbol{\sigma}' - \mathbf{I}\,\alpha_B p^f \right] = 0 \tag{3.27}$$

resulting:

$$\boldsymbol{\sigma} = \boldsymbol{\sigma}' - \mathbf{I}\,\alpha_B p^f \tag{3.28}$$

Let us now examine in detail some constitutive behaviors of the medium. In case of small strain and small rotation regime, the linear elasticity theory holds for the Cauchy effective stresses. But if rotations become relevant, the Second Piola Kirchhoff stress tensor must be used instead of the Cauchy stress and the Cauchy-Green strain tensor[10] must replace the small strain tensor [55, p. 237]. In case of small strain this type of nonlinear elasticity is called Saint Venant-Kirchhoff hyperelasticity and can be seen as an extension of linear elasticity for large rotations.

We can write the second Piola Kirchhoff stress tensor as:

$$\mathbf{S} = \mathbf{D} : \mathbf{E} \tag{3.29}$$

where $\mathbf{D}$ is the fourth-order tensor of elastic moduli, constant for Saint Venant-Kirchhoff materials, and $\mathbf{E}$ is the Green-Lagrange strain tensor.

Due to its path-independency and reversibility, Saint Venant-Kirchhoff material admits an elastic strain potential energy w :

$$w = \frac{1}{2}\mathbf{E} : \mathbf{D} : \mathbf{E} \tag{3.30}$$

from which the stress tensor can be derived as:

$$\mathbf{S} = \frac{\partial w}{\partial \mathbf{E}} \tag{3.31}$$

By considering an isotropic material, it can be shown that:

$$\mathbf{D} = \lambda \mathbf{I} \otimes \mathbf{I} + 2\mu \mathbf{I} \tag{3.32}$$

where λ and μ are the Lamé constants, which can be expressed in terms of Young's modulus and Poisson's coefficient as:

---

[10] The Cauchy-Green tensor is defined as:

$\mathbf{E} = \frac{1}{2}\left(\mathbf{F}^{\mathrm{T}}\mathbf{F} - \mathbf{I}\right)$, where $\mathbf{F}$ is the deformation gradient. It is commonly used for large rotation problems, because it does not produce deformation due to rotation. Indeed, if we consider a rigid body motion such as:

$\mathbf{x}\left(\mathbf{X}, t\right) = \mathbf{R}\left(t\right) \cdot \mathbf{X} + \mathbf{x}_T\left(t\right)$, where $\mathbf{R}\left(t\right)$ is the rotation tensor and $\mathbf{x}_T\left(t\right)$ is a translation

the deformation gradient is then $\mathbf{F} = \mathbf{R}$, and by noting that $\mathbf{R}$ is an orthogonal matrix we obtain that $\mathbf{E}$ is null:

$$\mathbf{E} = \frac{1}{2}\left(\mathbf{F}^{\mathrm{T}}\mathbf{F} - \mathbf{I}\right) = \frac{1}{2}\left(\mathbf{R}^{\mathrm{T}}\mathbf{R} - \mathbf{I}\right) = \mathbf{0}$$

$$\lambda = \frac{E\nu}{\left(1+\nu\right)\left(1-2\nu\right)} \tag{3.33}$$

$$\mu = \frac{E}{2\left(1+\nu\right)} \tag{3.34}$$

If we substitute (3.32) in (3.30), we can finally rewrite the potential w as:

$$w\left(\mathbf{E}\right) = \frac{\lambda}{2}\left[tr\left(\mathbf{E}\right)\right]^2 + \mu tr\left(\mathbf{E}\right)^2 \tag{3.35}$$

giving the 2nd Piola Kirchhoff stress tensor $\mathbf{S}$ the form of:

$$\mathbf{S} = \lambda tr\left(\mathbf{E}\right)\mathbf{I} + 2\mu tr\left(\mathbf{E}\right) \tag{3.36}$$

Saint Venant-Kirchhoff hyperelasticity is valid only in small strain regime. In case of larger deformations, other hyperelastic constitutive relationships should be used such as the Polynomial Hyperelasticity.

As for every elastic materials the stress tensor is obtained by derivation of the stored strain energy potential. For almost incompressible materials, by considering isotropy and additive decomposition of the deviatoric and volumetric strain, it is possible to write the potential as [56]:

$$w = f(\overline{I}_1 - 3, \overline{I}_2 - 3) + g(J_{el} - 1) \tag{3.37}$$

where $\overline{I}_1, \overline{I}_2$ are the invariants of the deviatoric stretch matrix of $\overline{\mathbf{F}}$, $\overline{\mathbf{F}}$ is the volume-preserving part of the deformation gradient, defined as in [57]:

$$\overline{\mathbf{F}} = J^{-1/3}\mathbf{F} \tag{3.38}$$

and J_{el} is the elastic volume strain.

The deviatoric stretch matrix of $\overline{\mathbf{F}}$ is defined as:

$$\overline{\mathbf{B}} = \overline{\mathbf{F}}\overline{\mathbf{F}}^T \tag{3.39}$$

where

The connection of $\overline{\mathbf{B}}$ with the left Cauchy-Green strain tensor results:

$$\overline{\mathbf{B}} = J^{-2/3}\mathbf{B} \tag{3.40}$$

We can then express the invariants $\overline{I}_1, \overline{I}_2$ of $\overline{\mathbf{B}}$ as:

$$\overline{I}_1 = tr(\overline{\mathbf{B}}) \tag{3.41}$$

$$\overline{I}_2 = \frac{1}{2}\left(\overline{I}_1^{\,2} - tr(\overline{\mathbf{B}}\overline{\mathbf{B}})\right) \tag{3.42}$$

It is possible to write $\overline{I}_1, \overline{I}_2$ in terms of the two invariants I_1, I_2 of the left Cauchy-Green strain tensor by recalling equation (3.40):

$$\overline{I}_1 = J^{-2/3} I_1 \tag{3.43}$$

$$\overline{I}_2 = J^{-4/3} I_2 \tag{3.44}$$

It is finally possible to introduce g as in [56]:

$$g = \sum_{i=1}^{N} \frac{1}{D_i}\left(J_{el} - 1\right)^{2i} \tag{3.45}$$

expanding function $f(\overline{I}_1 - 3, \overline{I}_2 - 3)$ using Taylor series, we obtains the final form of the potential for a Polynomial Hyperelasticity:

$$w = \sum_{i+j=1}^{N} C_{ij}\left(\overline{I}_1 - 3\right)^{i}\left(\overline{I}_2 - 3\right)^{j} + \sum_{i=1}^{N} \frac{1}{D_i}\left(J_{el} - 1\right)^{2i} \tag{3.46}$$

where C_{ij} and D_i are the material parameters of the model.

Initial properties of the medium, such as shear and bulk moduli, which depend only on the polynomial coefficients of order $N = 1$ are:

$$\mu_0 = 2\left(C_{10} + C_{01}\right) \tag{3.47}$$

$$k_0 = \frac{2}{D_1} \tag{3.48}$$

Usually experimental results on mechanical properties of materials are commonly expressed in terms of Young's modulus and Poisson's coefficient: by using (3.47) and (3.48) initial values of E and ν can be then written as:

$$E = \frac{9k_0\mu_0}{3k_0 + \mu_0} \tag{3.49}$$

$$\nu = \frac{3k_0 - 2\mu_0}{2(3k_0 + \mu_0)} \tag{3.50}$$

The great importance of the proper choice of the constitutive behavior for the solid skeleton will be discussed in the material section (§3.1.7).

3.1.4. Experimental setup and data acquisition

One of the strengths of this thesis is the deep connection between the mathematical framework developed together with the computational skills and the experimental experience. As a result, the innovative model for the soft tissue obtained can be applied to patient specific data.

Here it is briefly shown how the subject specific (healthy and diabetic) input data of foot and gait cycles (i.e. kinetics, kinematics and geometry) are acquired and processed by *DEI team*.

The experimental setup is composed of two force plates, two plantar pressure systems and a 60 Hz stereophotogrammetric system with six cameras (see Figure 3.2).

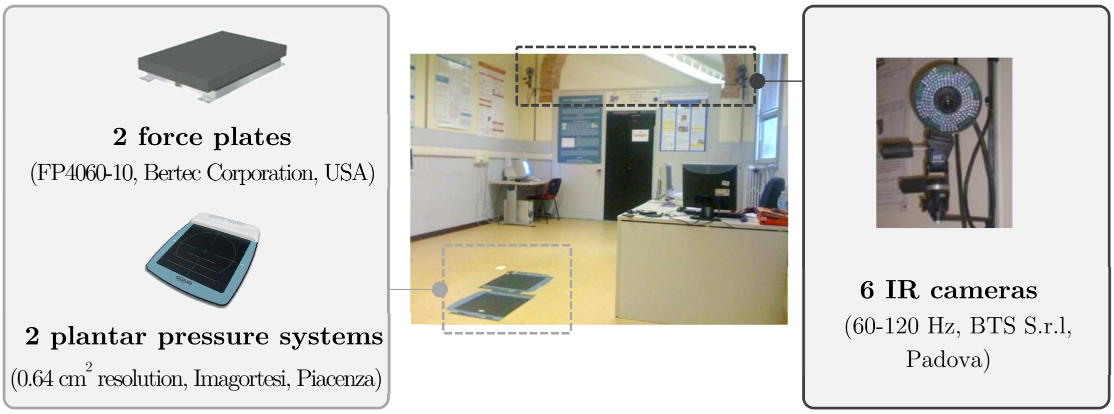

Figure 3.2 Experimental setup, comprising IR cameras, force and pressure systems, which allows to assess kinematic, kinetics and plantar pressure of the foot during gait cycles. [courtesy of DEI team]

Ground reaction forces are acquired by the force plates in terms of vertical reaction and in-plane shear forces (anterior-posterior and medio-lateral ground reacting forces), whereas plantar pressures (PP) are measured with the PP systems. The kinematics of the foot is obtained by starting from a four segment 3D foot kinematical model (Figure 3.3): the position of selected anatomic landmarks [7] (pinpointed on the foot with a tape) is tracked by the IR cameras, allowing to evaluate the joint rotation angles during the gait cycle. Both static trials and more than three gait cycles of each limb[11] are acquired in motion analysis data collection, to assure trustworthy output datasets.

The plantar foot is then subdivided into subareas [58], [59], by projecting the chosen reference landmarks on the ground, defining three surfaces of interest for contact pressures: the hindfoot, the midfoot and the forefoot [60] (Figure 3.3). Finally, the signals from different input sources are synchronized temporally and spatially in post processing, to align the data coming from different sources to the gait cycle timeline of the subject.

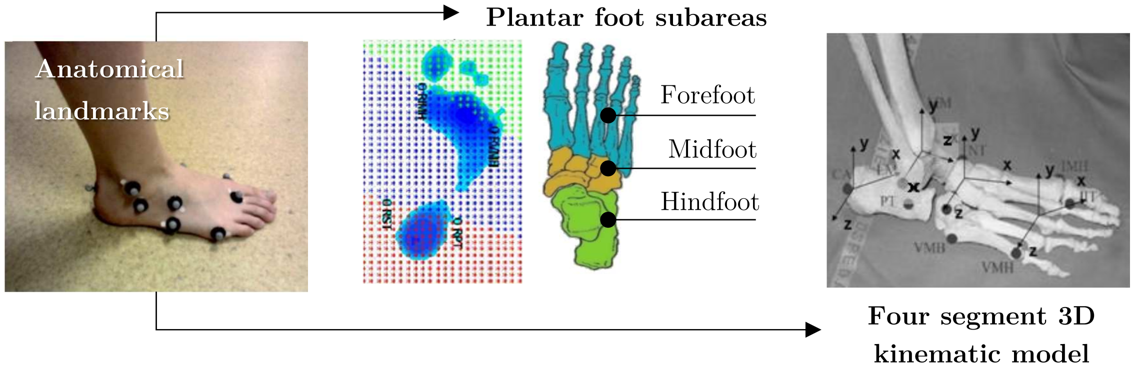

Figure 3.3 Details of the anatomical landmarks (on the left), of the three plantar foot surfaces (in the middle) and the four segment 3D kinematic model, composed by tibia, hindfoot, midfoot and forefoot (on the right). [Images: courtesy of DEI team]

This experimental setup allows to obtain the input loads for the numerical model and the contact pressures with the ground for the validation.

Let us now briefly consider the procedure developed for defining the patient specific geometry of the foot (interested reader can find full details in [9]). First, a magnetic

---

[11] Two different motor tasks are assigned to patients [60]:

1. *Static acquisition*, where patients have to stand in an upright position for 60 s.
2. *Gait analysis*, in which subjects have to walk at their natural and comfortable velocity for at least three steps.

resonance imaging of the foot is made, obtaining images of the foot in slices at fixed depth. Starting from the output images, tissue, bones, cartilages, plantar fascia and ligaments are segmented, giving rise to the 3D geometry of the patient specific foot. Finally, the three-dimensional geometry is discretized to obtain the mesh for the finite element analysis. A visual representation of the process is exemplified in Figure 3.4.

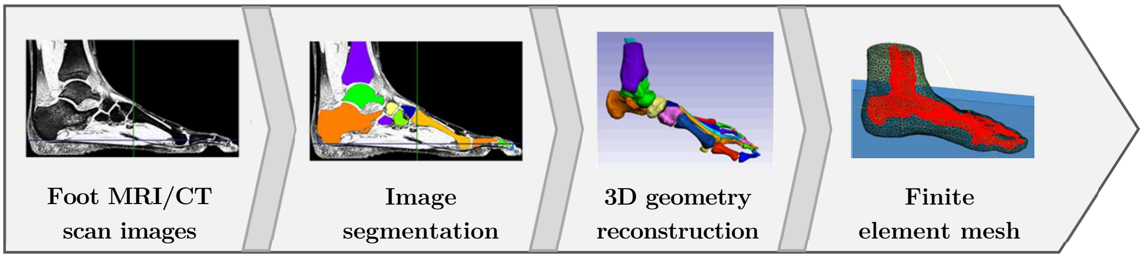

Figure 3.4 Flow chart of the processes to define a 3D patient specific FE mesh. [Images: courtesy of DEI team]

3.1.5. Patient specific geometry

Two different geometries are defined: one for the healthy foot and another one representing a diabetic foot. Out of the geometrical data, it is possible to obtain 3D representations as well as 2D ones.

The 3D geometries were very useful to assess main differences in behavior between the healthy and the diabetic models, depending upon specific constitutive behaviors assumed, through the comparison of different output variables such as stresses, strains and contact pressures. Furthermore, 3D finite element analyses allowed the comparison between numerical results and the experimental ones, for a possible validation.

By taking advantage of the valuable information obtained from 3D finite element models, 2D geometries were developed: by cutting the three-dimensional foot with a plane through tibia, heel and second metatarsal head, a 2D geometry is possibly defined for both healthy and neuropathic foot. In this case, ligaments, tendons and plantar fascia are neglected by assuming a stiffer cartilage to assure an adequate *arch effect* in the foot. That simplified geometry was accurately selected to preliminarily study the ulceration risk and, in the same time, to lessen the elevated computational costs connected to complexity of the mathematical model implemented (see §3.1.3). The geometry of the different models are represented in Figure 3.5, whereas the characteristics of the subjects are briefly summarized in Table 1:

Table 1 Data of the subject specific foot (healthy and diabetic) [9]

Condition	Healthy	Diabetic
Sex	F	M
Age	27	61
Weight [kg]	61	79
Height [cm]	174	175
Foot size	40	42.5
Type of foot	Normal	Cavus

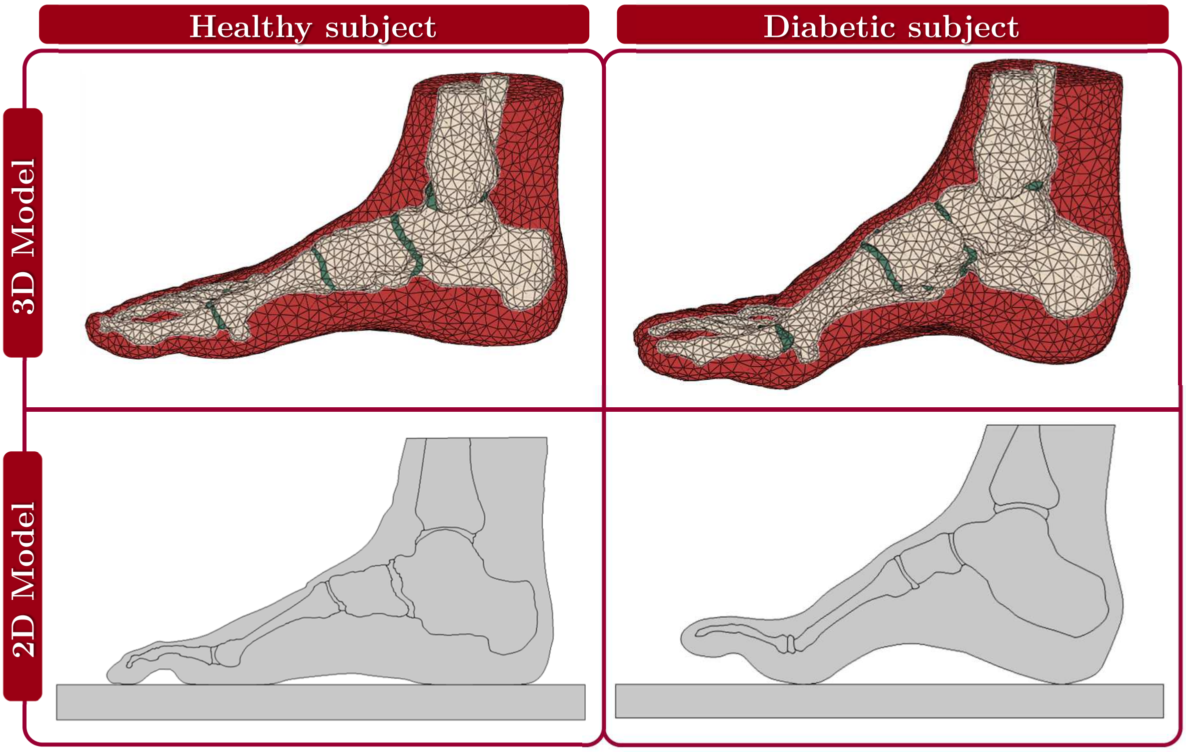

Figure 3.5 Healthy and diabetic geometries are represented. The two images on the top are the 3D models, whereas the other two at the bottom are the 2D models, which are obtained by considering a cutting plane that passes through tibia, heel and second metatarsal head.

3.1.6. Patient specific loading configuration

The definition of a proper loading scheme out of experimental acquisitions was a crucial point of this work. On one hand we have a rich dataset coming from experimental results (*DEI team*), while on the other we need to simplify it as much as possible for our model input. Different sources of nonlinearity affect simultaneously the model: the constitutive behavior of the whole tissue (solid and fluid), as well as the nonlinear elasticity behavior of its solid skeleton. Another aspect that influences the convergence rate of the analysis negatively is the contact feature: in order to represent the gait cycle faithfully, and to be able to evaluate contact pressures with the ground, we have to deal with the nonlinear problem of contact foot-ground.

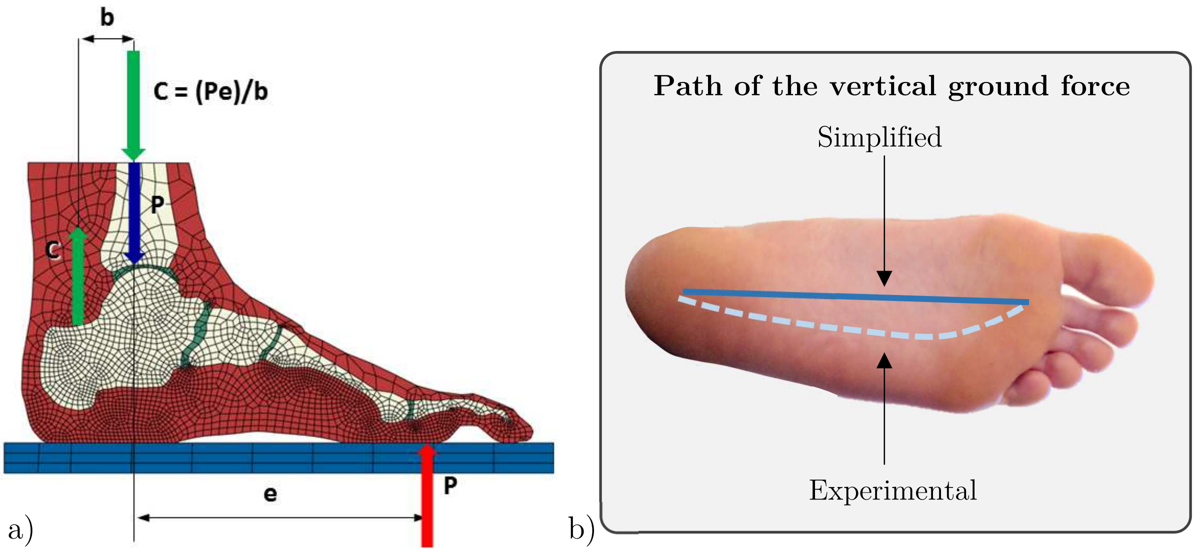

Figure 3.6 The loading scheme (a): the position of the resultant vertical force under the foot is made varying thanks to the application of a time dependent couple to the heel. (b) A simplified path is used: straight line, instead of curve.

First, we decided to start by neglecting the shear forces (anterior-posterior and medio-lateral) and considering only the vertical reaction force and its position during the gait. The loading configuration adopted is shown in Figure 3.6: by omitting the shear forces, the path of the resultant vertical force is transformed in a straight line, instead of the curve, measured experimentally (Figure 3.6, image on the right). The experimental vertical load and the angle of the foot with the ground in Figure 3.7 are normalized in time by using the values in Table 2.

Table 2 Stance phase and gait cycle time measured for healthy and diabetic subjects.

Condition	Healthy	Diabetic
t stance phase [s]	0.62	0.65
t gait cycle [s]	1.10	1.07

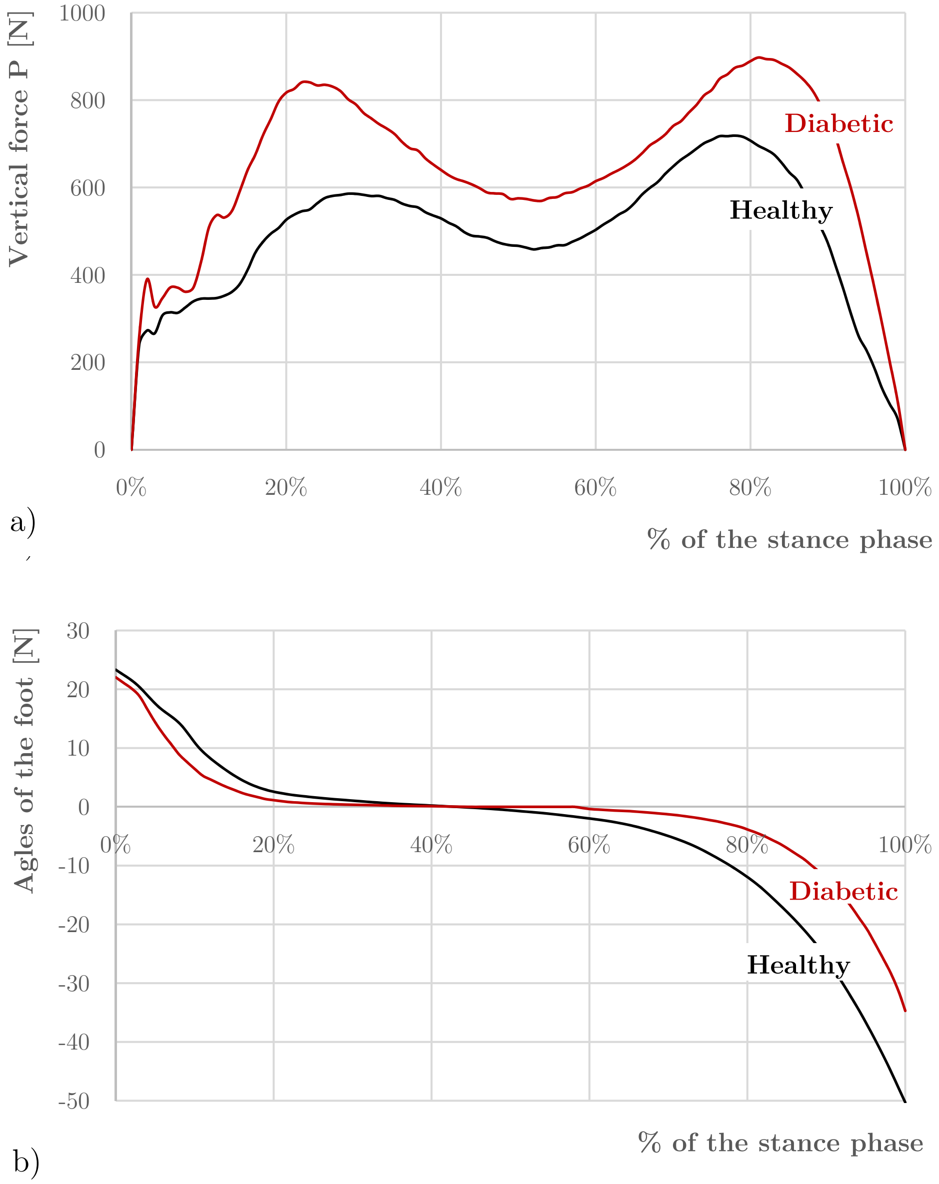

Figure 3.7 a) Values of vertical forces as a function of time and b) angles of the sole of the foot with respect to the ground, experimentally measured for healthy and diabetic subjects.

Two type of load cases are finally considered: one that represents the movements of the foot from the initial contact with the ground to the propulsive phase (i.e. a complete gait cycle) and a simplified one, to simulate multiple gait cycles.

Let us now focus on the first load configuration. To ensure the movement of the resultant force $\left(\mathbf{P}\right)$ under the foot (from the heel to the toes), a couple $\left(\mathbf{C}'\left(x_1+x_2\right)\ or\ \mathbf{C}''\left(x_1-x_2\right)\right)$ is used (Figure 3.8). Depending on the inclination of the foot during the gait cycle, a distance between forces $\left(x_1+x_2\right)\ or\ \left(x_1-x_2\right)$ that is variable with time is considered. To define the loading conditions, one step can be simplified in two parts: the first one is as an almost rigid rotation of the foot around its contact point with the floor. The second one starts when the whole foot is in contact with the ground (midstance phase): from this moment, another rotation of the foot undergoes around a small area of contact, near the forefoot (Figure 3.11).

Though the evaluation of the analytical formula for a couple is clearly a straightforward task, the large rotation regime forced us to develop, with some effort, an *ad hoc* formulation to take into account a distance between couple forces that varies with the rotation of the foot.

Let us consider the *initial contact* of the step (Figure 3.8a, Figure 3.9, Figure 3.11). The first thing to be computed is the limit inclination $\alpha_{\lim}$ when the points C and C1 in are aligned vertically:

$$\alpha_{\lim} = \alpha(x_1 = 0) = tg^{-1}\left(\frac{\overline{C1H}}{\overline{CH}}\right) \tag{3.51}$$

$\alpha_{\lim}$ influences the values of x_1, x_2, which are defined as:

$$x_1 = \left|\overline{CH}sen\alpha - \overline{C1H}\cos\alpha\right| = \begin{cases} \overline{CH}sen\alpha - \overline{C1H}\cos\alpha,\ \alpha \geq \alpha_{\lim} \\ -\overline{CH}sen\alpha + \overline{C1H}\cos\alpha,\ \alpha < \alpha_{\lim} \end{cases} \tag{3.52}$$

$$x_2 = \left|\overline{CB}\cos\alpha - \overline{QB}sen\alpha - x_1\right| = \begin{cases} \overline{CB}\cos\alpha - \overline{QB}sen\alpha - x_1,\ \alpha \geq \alpha_{\lim} \\ \overline{CB}\cos\alpha - \overline{QB}sen\alpha + x_1,\ \alpha < \alpha_{\lim} \end{cases} \tag{3.53}$$

Considering that in our model we have always $x_3 > x_2$, the force **C'** of the couple can be finally obtained as (Figure 3.8a, bottom):

$$C' = \begin{cases} -P\dfrac{\left(x_2 - x_3\right)}{x_1 + x_2},\ \alpha \geq \alpha_{\lim} \\ -P\dfrac{\left(x_3 - x_2\right)}{x_2 - x_1},\ \alpha < \alpha_{\lim} \end{cases} \tag{3.54}$$

We can now pass to the second part of the gait, after the midstance and up to the uplift of the heel.

By considering the quantities displayed in Figure 3.8b, we can define:

$$x_1' = \overline{HN}\cos\alpha - \overline{CH}sen\alpha \tag{3.55}$$

$$x_2' = \overline{MN}\cos\alpha - \overline{PM}tg\alpha\cdot\cos\alpha \tag{3.56}$$

$$x_3' = \left[C_1N - x_3\right]\cos\alpha \tag{3.57}$$

And finally the force of the couple C'' can be written using (3.55) and (3.56) as:

$$C'' = P\frac{\left(x_2' - x_3'\right)}{x_1' - x_2'} \tag{3.58}$$

The vertical resultant force **P** and force of the couple **C'** are represented, for both healthy and neuropathic subjects, in Figure 3.10.

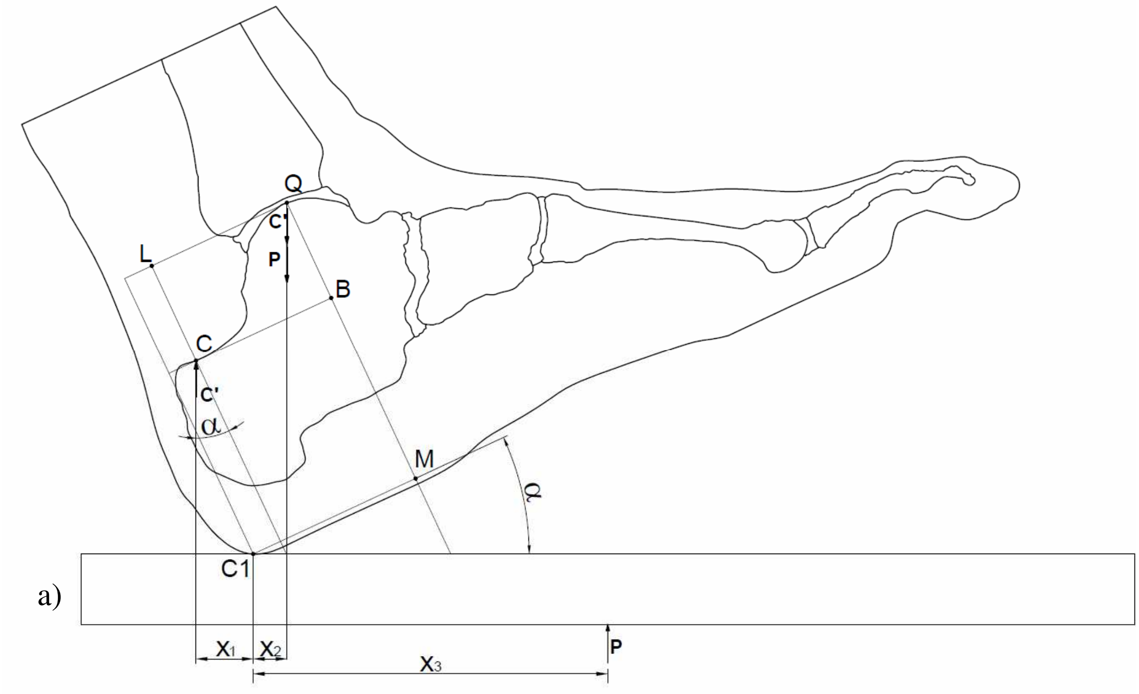

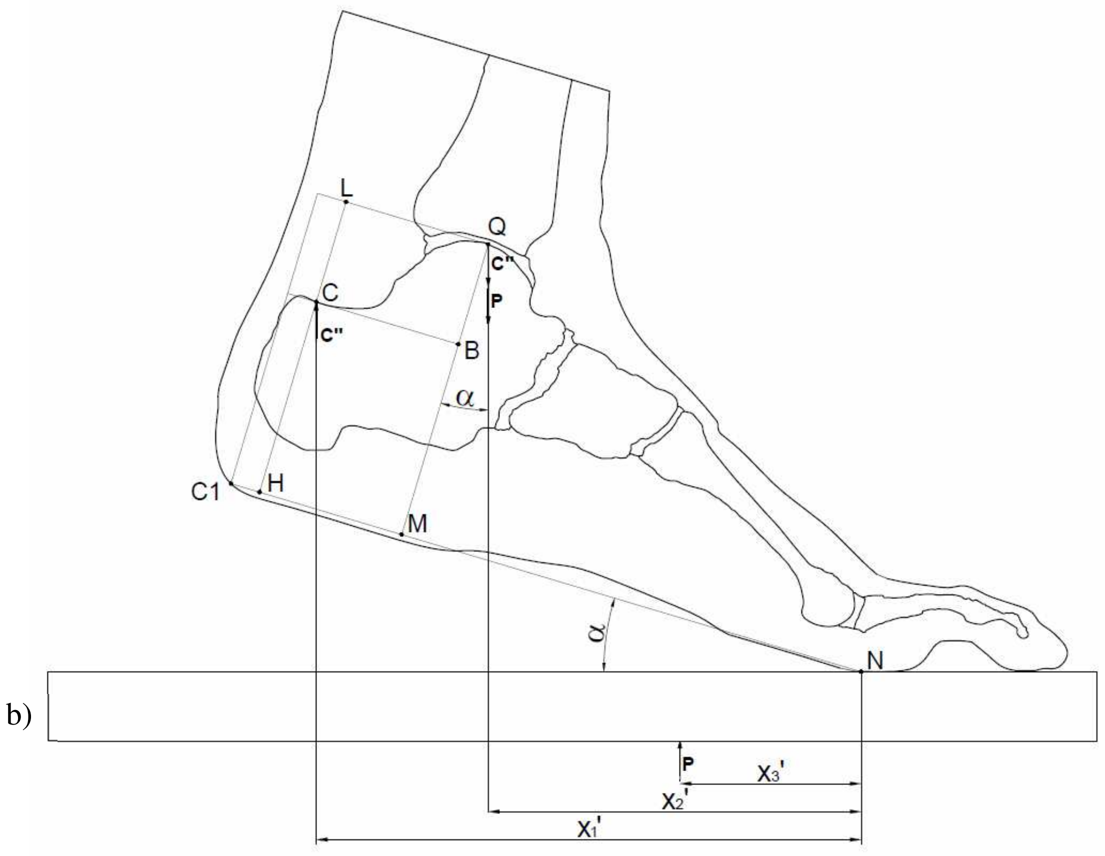

Figure 3.8 Schematization of the parameters in the definition of the couple. Two configuration are represented: a) From initial contact to the midstance; b) From the midstance to the preswing.

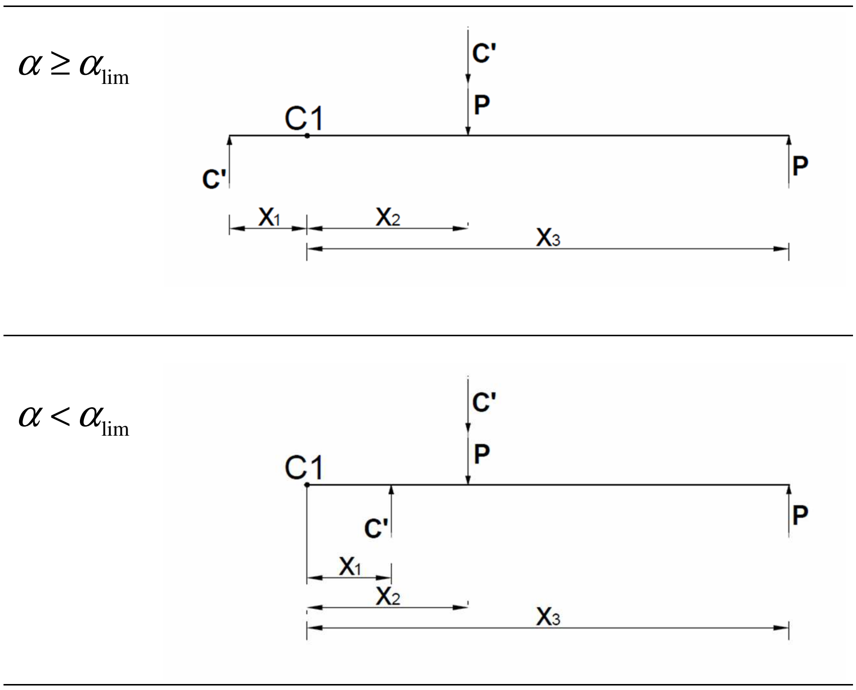

Figure 3.9 Schematization of the forces from initial contact to the midstance.

The final values of the vertical forces displayed in Figure 3.10a are smoothed from experimentally measured data (see Figure 3.7a), thanks to the use of a polynomial data interpolation, obtaining a continuous curve without discontinuities.

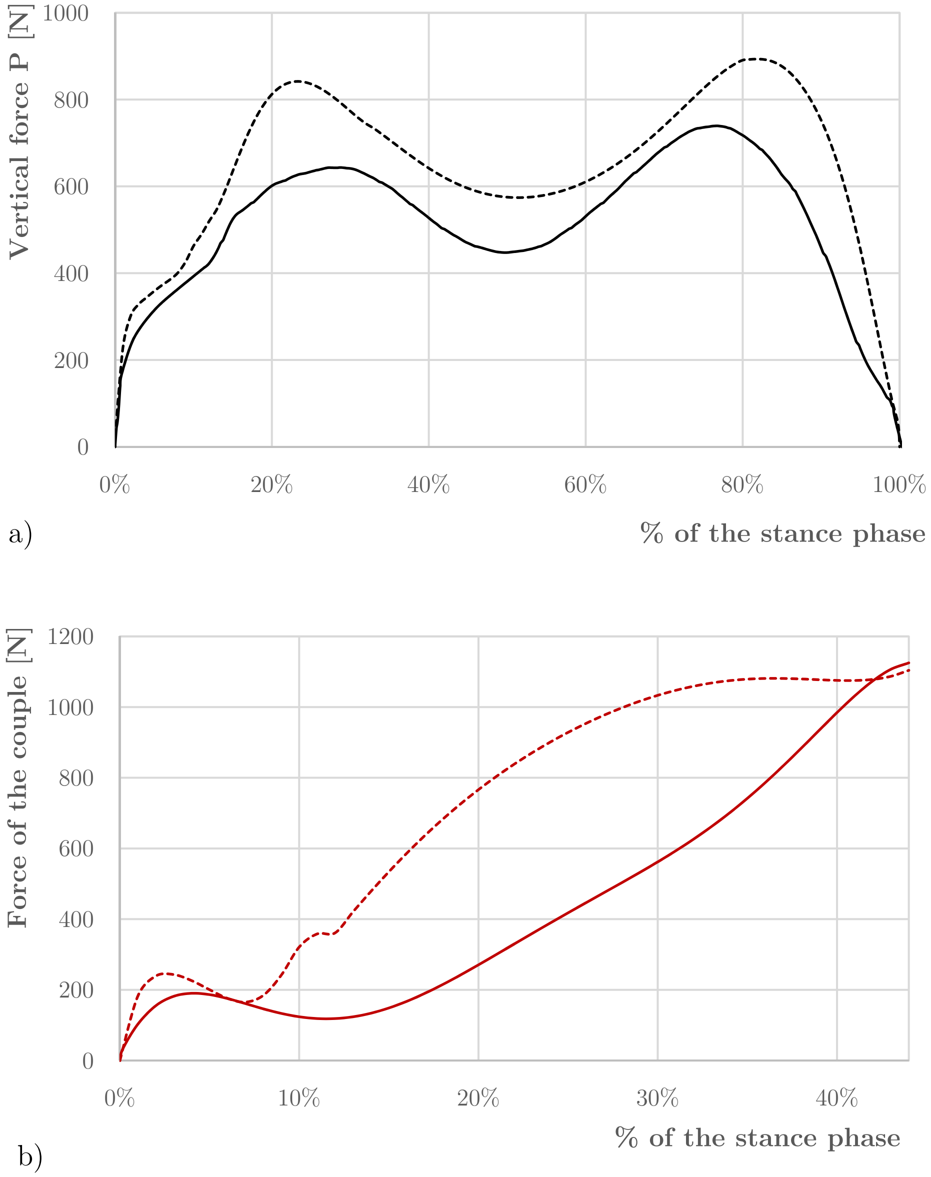

Figure 3.10 a)Vertical force and b)force of the couple as a function of the percentage of the stance phase in gait cycle, for both healthy (continuous line) and diabetic (dotted line) subjects.

Let us now consider the second loading configuration. We want to simulate multiple steps: that means making the foot to come in contact with the floor through the heel, reach the full contact, uplift, swing and finally start another the cycle (Figure 3.11).

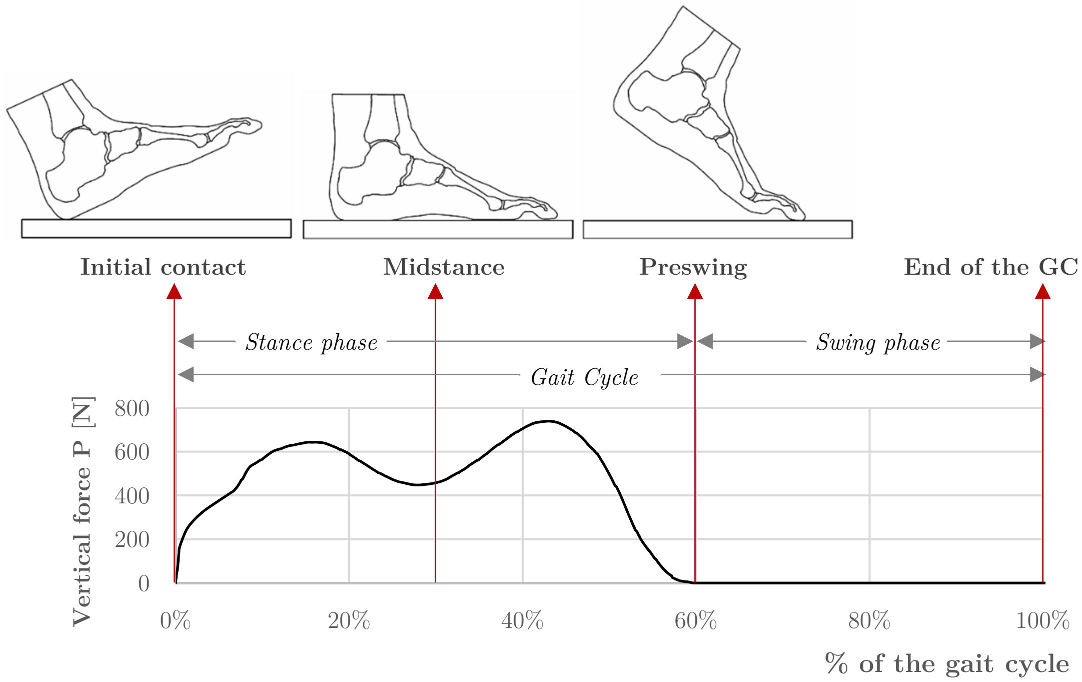

Figure 3.11 Schematization of the main subphases in the gait cycle.

The modelling of that situation is very hard: a trade-off solution is then developed to limit computational costs. As a consequence, we decide to reduce up to 50% the maximum extent of the position of the resultant vertical force $\left(x_3\right)$: in this way the foot undergoes small rotation as well as limited lifting of the heel. By depriving the analysis of large rigid body motions, we are allowed to simulate multiple simplified steps. In this way, pressure peaks hardly reaches toes region, nevertheless this solution permits to both study the fluid-structure interaction phenomenon due to cyclic loading as well as the development of the ulceration, allowing us to show the potentialities of our model. Loading values for both healthy and diabetic foot are represented in Figure 3.12, for the four gait cycles considered.

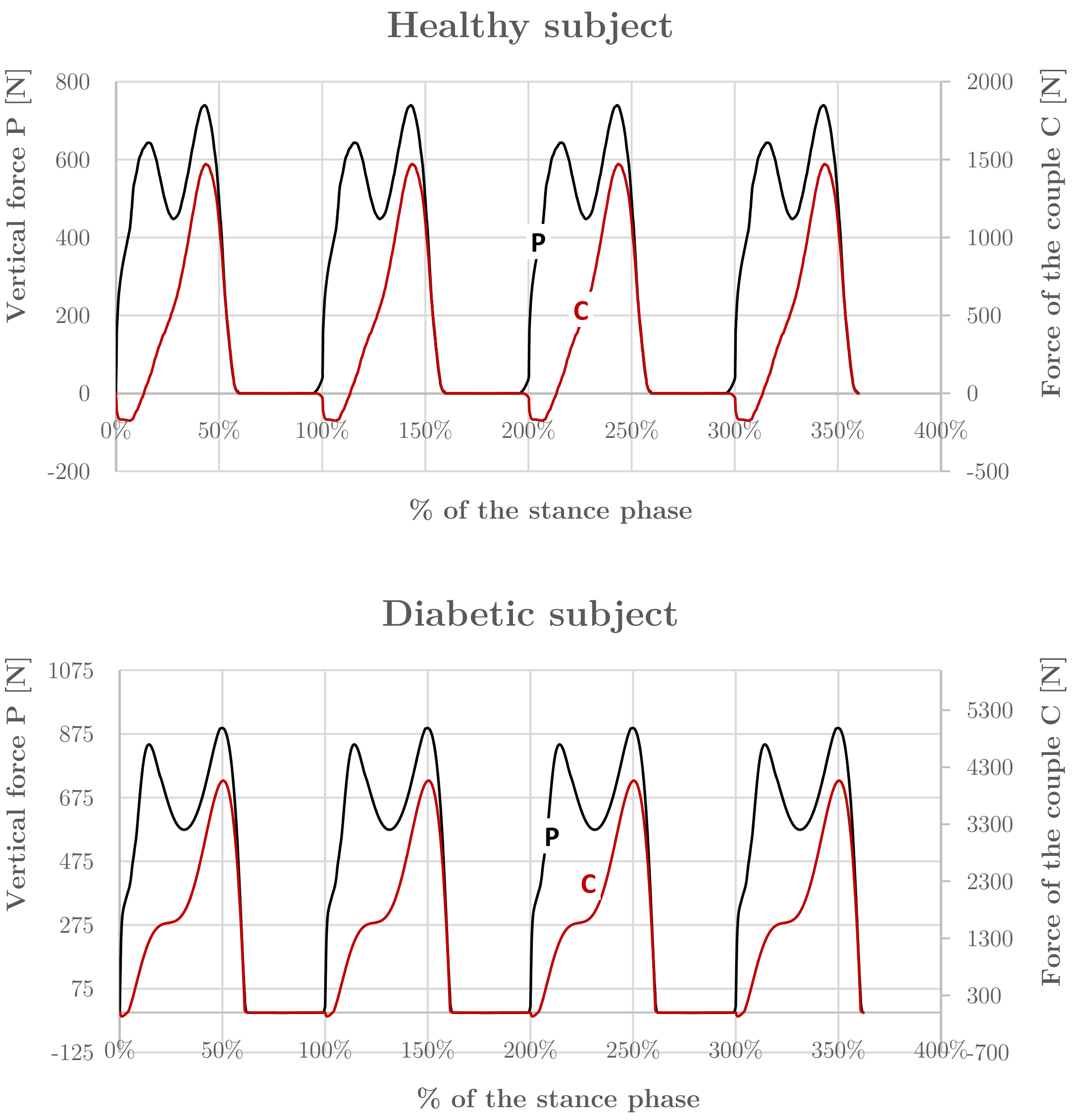

Figure 3.12 Vertical force and force of the couple as a function of the percentage of one gait cycle, for four steps, for a healthy (*top*) and diabetic (*bottom*) foot.

3.1.7. Material parameters

After defining the mathematical model, the domain of the problem and the loading configuration, we now focus on the materials of the foot components (i.e. tissue, bones, cartilages and ligaments).

Material characterization in biological field is certainly a challenging task: they must be made with specific *non-invasive* experimental setups. As a consequence, the lack of patient specific parameters is quite common, and it is often necessary to take literature values. In our model, the bones and the cartilages follow Saint Venant-Kirchhoff nonlinear elastic behavior, while the plantar fascia, tendons and ligaments are modelled as trusses, acting only for traction forces. The properties are summarized in Table 3 below.

Table 3 Material properties of bones, cartilages, tendons and ligaments in the diabetic foot FE model.

Component	E [MPa]	v	A [mm^2]
Bones [61]	7300	0.3	-
Cartilage [62]	1.01	0.4	-
Plantar fascia [44], [62]	350	-	290.7
Tendons and ligaments [44], [62]	260	-	18.4

In Table 3, soft tissue is not considered: an in-depth analysis must indeed be done for it. The plantar tissue behaves certainly as a nonlinear elastic material as can be found in [41], [61]–[63]. In our preliminary study we decided to start with modeling the solid skeleton of the tissue as a linear elastic material [45], [64], [65]($E = 1\ MPa$, $\nu = 0.4$) or as a Saint Venant-Kirchhoff material in case of large rotations, to reduce the computational effort. The resulting tissue is much stiffer than the one found in literature, but it seemed to be a good compromise [62] for taking into account the stiffening effect due to growing of strain values. By analyzing numerical results we focused on two main aspects. First, we observed that the contact pressures with the ground were higher than the one measured experimentally. Second, the values of strain peaks that the tissue underwent were around 30%. Clearly the hypotheses of linear elasticity (i.e. small strains) were not valid. As a consequence, following [9], [62], we decided to model the solid skeleton of the tissue as a polynomial hyperelastic material, to take into account its nonlinear behavior and, even more important, to be able to properly consider large strains. After introducing hyperelastic constitutive behavior another valuable enhancement was brought to our model: a differentiation between healthy and diabetic tissue behavior. Accordingly to §3.1.1, the diabetic patient undergoes modifications on tissue properties, e.g. stiffening phenomenon. By following the strategy introduced in [9], we decided to use experimental properties [62] for the healthy foot and a two times stiffer values for the diabetic foot (Table 4). A comparison between the trends of the different constitutive relations considered is shown in Figure 3.13.

As regards intrinsic permeability, which is fundamental in defining the porohyperelastic behavior of the tissue, no specific experimental data were found in literature. Nevertheless, it is assumed of the same order of magnitude of a similar tissue found in [66].

Table 4 Material properties for the soft tissue [9].

	C_{10} [MPa]	**C_{01}** [MPa]	**C_{20}** [MPa]	**C_{11}** [MPa]	**C_{02}** [MPa]	**D_1** [1/MPa]	**k** [m^2]	ε
Healthy	0.08556	-0.05841	0.039	-0.02319	0.00851	3.65273	2E-13	0.9
Diabetic	0.17112	-0.11682	0.078	-0.04638	0.01702	1.826365		

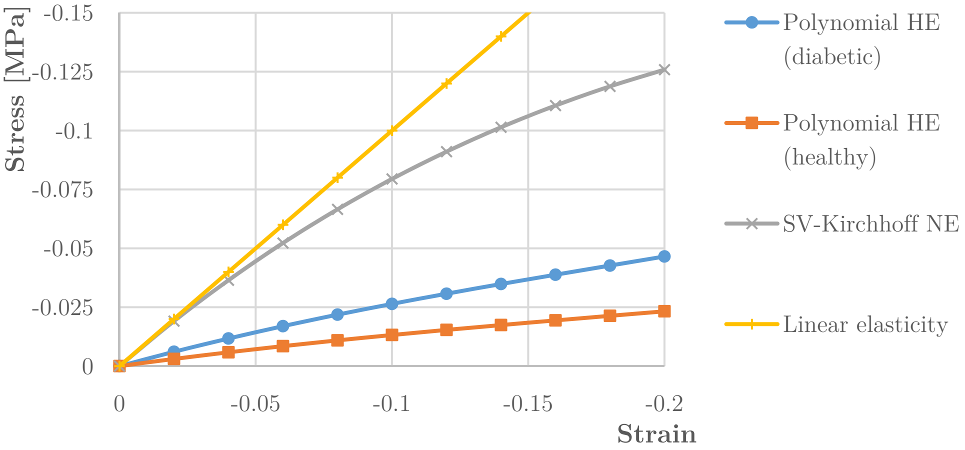

Figure 3.13 Comparison between different constitutive behaviors taken into consideration in the model development

However, due to the lack of experimental values, we decided to analyze the effects of permeability variations on two different control variables: the effective stress and the interstitial fluid pressure, because of their relevance in our model for the ulceration triggering phenomenon (§3.1.2).

Thus, an OAT (one-factor-at-a-time) sensitivity analysis [67] is performed, with values of permeability that vary from 0.0002 mm/s to 0.02 mm/s, considering also intermediate values (see Table 5).

Table 5 Values of permeability considered in the OAT sensitivity analysis.

$\mathbf{k_1}$ [m^2]	$\mathbf{k_2}$ [m^2]	$\mathbf{k_{ref}}$ [m^2]	$\mathbf{k_3}$ [m^2]	$\mathbf{k_4}$ [m^2]
2E-12	4E-13	2E-13	1E-13	2E-14

Four simplified gait cycles are taken into account and the values of the control variables are recorded in two points within the foot tissue: beneath the heel and under the second metatarsal head zone (see Figure 3.15). To include in our analysis the effect of material behavior in healthy and diabetic tissue, both hyperelastic constitutive models are studied using the healthy subject geometry[12]. Results are shown in Figure 3.15 and Figure 3.16, where the dotted lines represent the reference curves obtained with the reference permeability (0.002 mm/s). From Table 6 it is clear that the peaks of the output variables (interstitial fluid pressure and effective vertical stress) are sensitive to large variation of the permeability (one order of magnitude). On the contrary, a smaller but significant variation on permeability (about 50%), leads to maximum absolute values of fluid pressure and stresses that are not too dissimilar from the reference case (15% in the healthy, 20% in the diabetic foot). From these results we can state that the value found in literature [66] can be considered as a good starting point for our analysis. Taking full advantage of the information from the sensitivity analysis, let us make some remarks about the different constitutive behaviors of healthy and diabetic tissue.

---

[12] The application of different hyperelastic properties (for the healthy and diabetic tissue) to the geometry and loads of the healthy foot allows to consistently compare the results obtained.

Comparing for the reference permeability, the interstitial fluid pressure and the effective stress, it is possible to see that the peaks of vertical stress are higher in the diabetic tissue than in the healthy one. On the contrary, the pore pressure shows an inverse trend, with lower peaks in the healthy tissue. For this reason, we believe that the ulceration triggering is related to the effective stresses in the porous media. In addition, the diabetic tissue has a stiffer behavior and reach higher peaks values. The ulceration stress threshold must be higher than the stress peaks in the healthy foot, because it does not ulcerate. On the contrary, the higher maximum stress values in diabetic foot (using same geometry and loads) can induce the ulceration triggering phenomenon.

Table 6 Variation of the maximum (absolute) peak of the variables take into account with respect to the reference value.

Subject	**Variable**	**Region**	**k=2E-14 m^2**	**k=1E-13 m^2**	**k=4E-13 m^2**	**k=2E-12 m^2**
Healthy	IFP	II metatarsal head	16%	7%	-9%	-33%
		heel	1%	1%	-3%	-18%
	Vertical Effective stress	II metatarsal head	-19%	-11%	15%	56%
		heel	-1%	-2%	11%	66%
Diabetic	IFP	II metatarsal head	32%	13%	-14%	-42%
		heel	7%	4%	-6%	-28%
	Vertical Effective stress	II metatarsal head	-37%	-16%	18%	51%
		heel	-18%	-13%	20%	78%

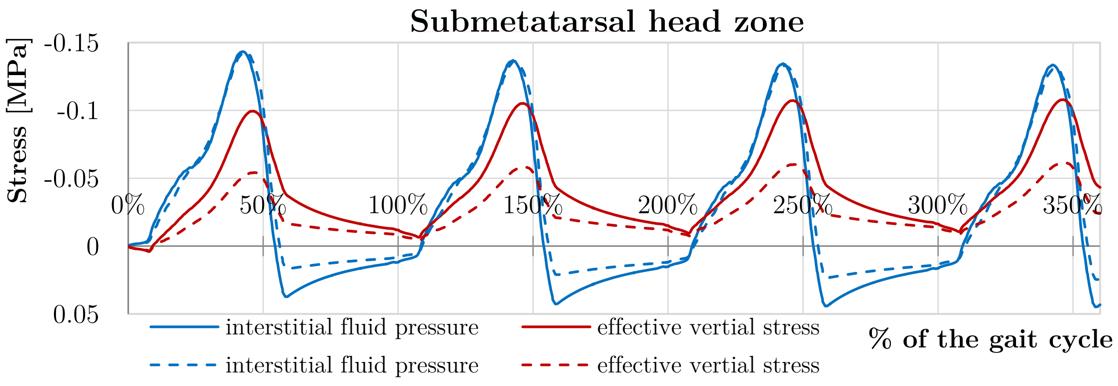

Figure 3.14 Comparison between results assuming different hyperelastic constitutive behavior for healthy and diabetic tissue, using the same reference permeability, as a function of the percentage of the gait cycle. Healthy tissue is represented in dotted lines, whereas diabetic one is displayed as continuous.

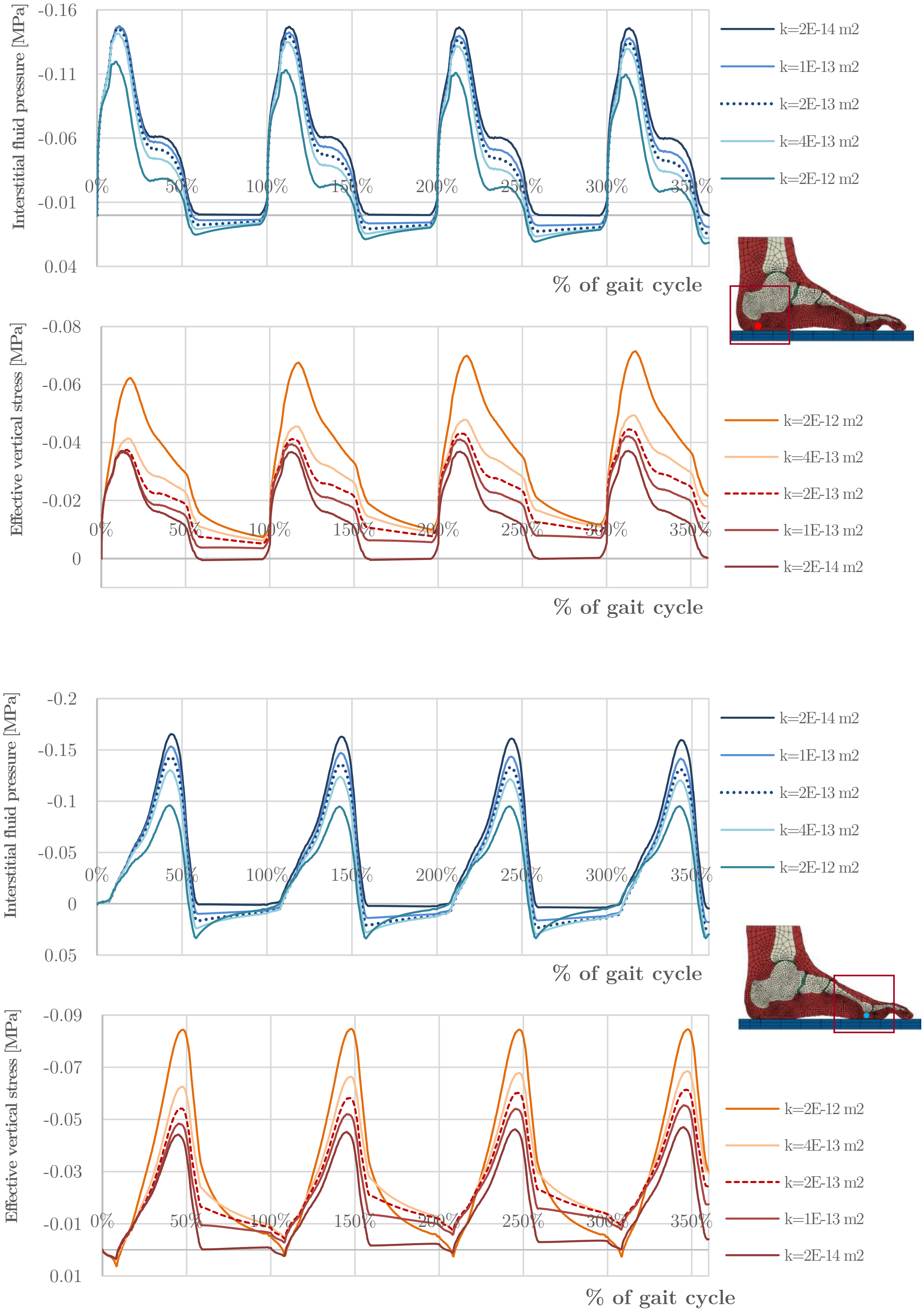

Figure 3.15 OAT sensitivity analysis for the permeability ***k*** in a healthy tissue for hindfoot (top) and forefoot (bottom) points.

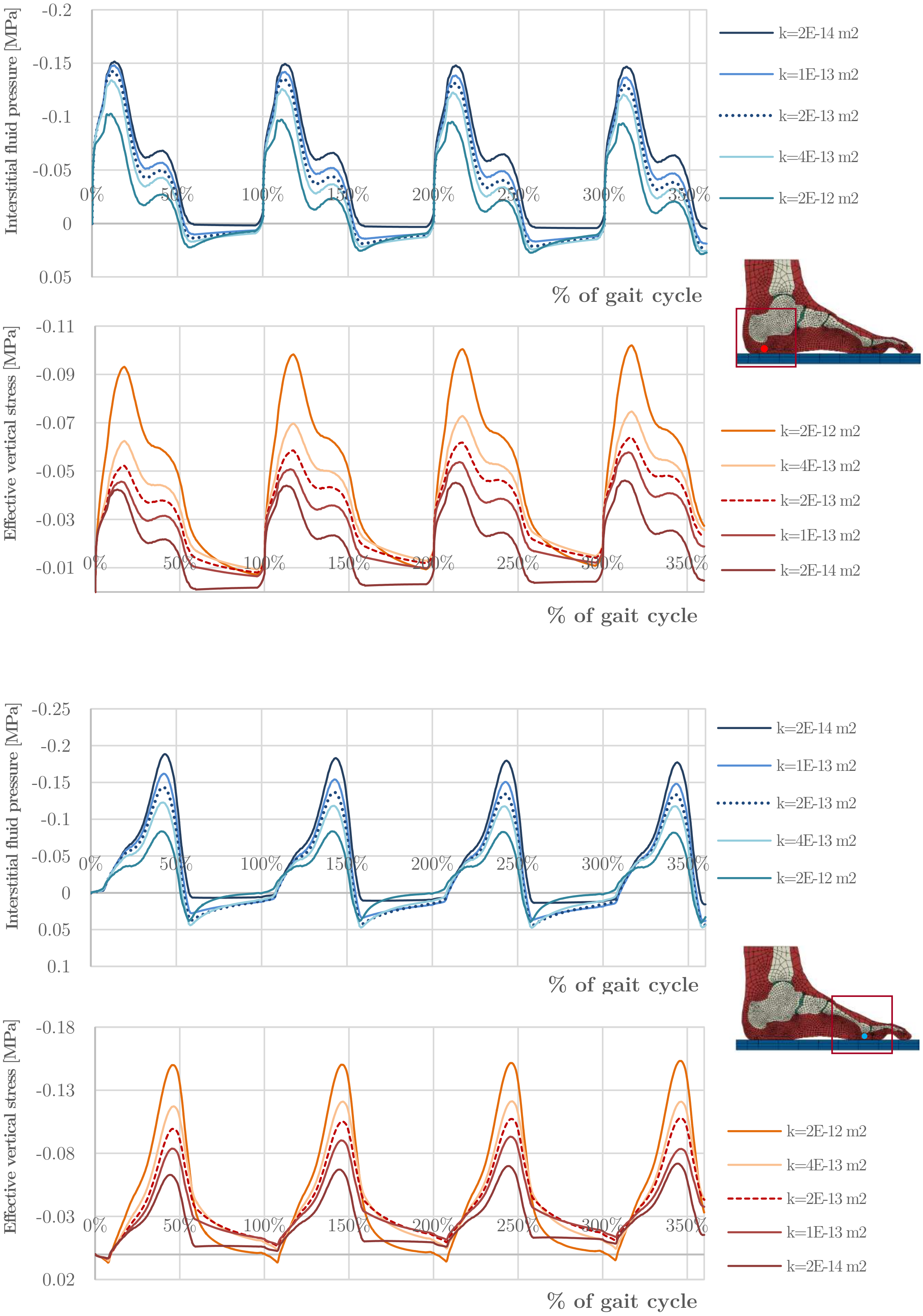

Figure 3.16 OAT sensitivity analysis for the permeability $\boldsymbol{k}$ in a neuropathic tissue for hindfoot (top) and forefoot (bottom) points.

3.1.8. Numerical results

First of all the Terzaghi consolidation benchmark is considered to test our model. It is inserted in appendix (§4.2), to avoid distracting from the main thrust of the thesis.

3.1.8.1. One gait cycle with 3D models

Let us introduce the first set of analyses of our work: the modelling of the foot behavior from the initial contact to midstance (Figure 3.17), in large rotations and large strains regime, with 3D geometry.

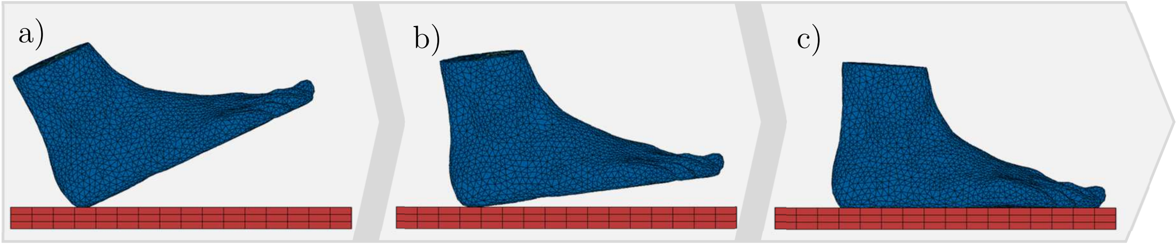

Figure 3.17 The movement of the healthy foot from the initial contact (a) to the midstance (c).

This was the starting point of our work: it was very helpful to preliminary assess the differences in the behavior of the two patient specific feet. Let us start with the study of the contact pressures with the ground. If we compare the healthy and neuropathic foot at the first peak of vertical force (i.e. about 25% of the stance phase, see Figure 3.7) we can notice the differences in the size of the contact areas (Figure 3.18). In the healthy foot the contact zones are more widespread under the heel. On the contrary, in the neuropathic foot, the contact takes place in limited areas under the heel as well as under the metatarsal heads, due to the structure of the foot and the stiffness of the tissue. As a result, the contact pressures are significantly higher in the diabetic subject (0.42 MPa) than in the healthy one (0.26 MPa). Even if the weight of the diabetic patient is different from the healthy one (79kg vs. 61kg, see

Figure 3.7), differences in peak values are due prominently to the geometry of the foot and to the stiffness of the neuropathic tissue. Difference between weights is indeed about 30%, whereas difference between peaks is about 50%.

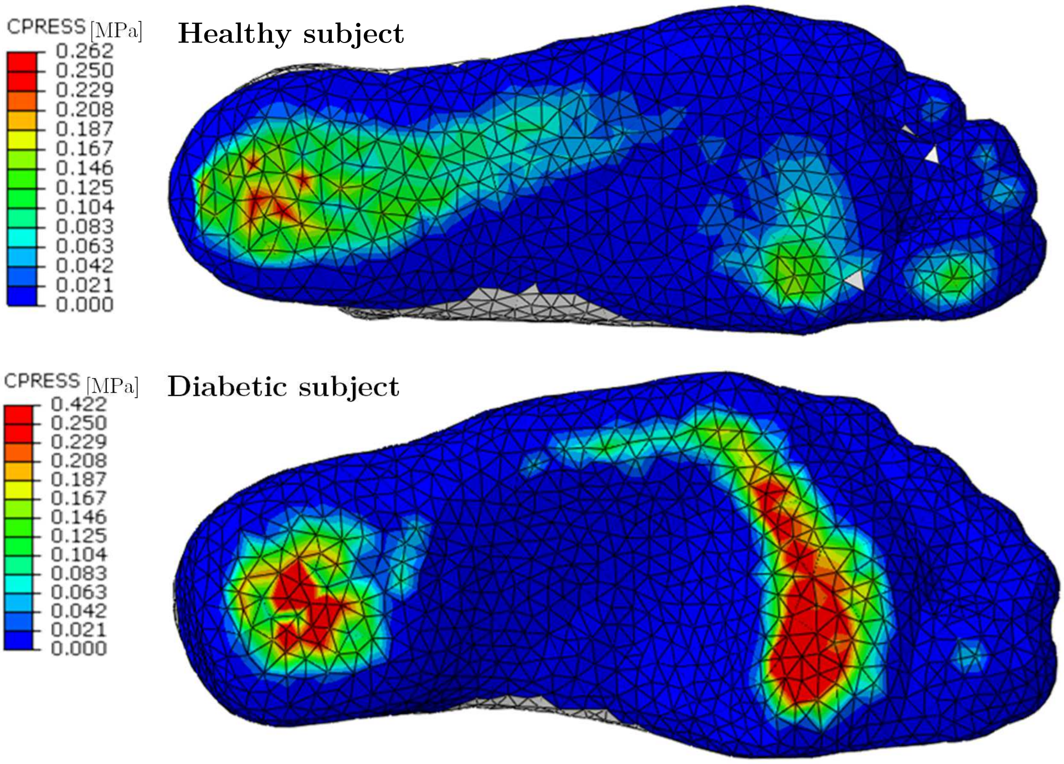

Figure 3.18 Contour plot of the ground contact pressure at about 25% of the stance phase in a gait cycle. Top: the healthy subject, bottom: diabetic patient.

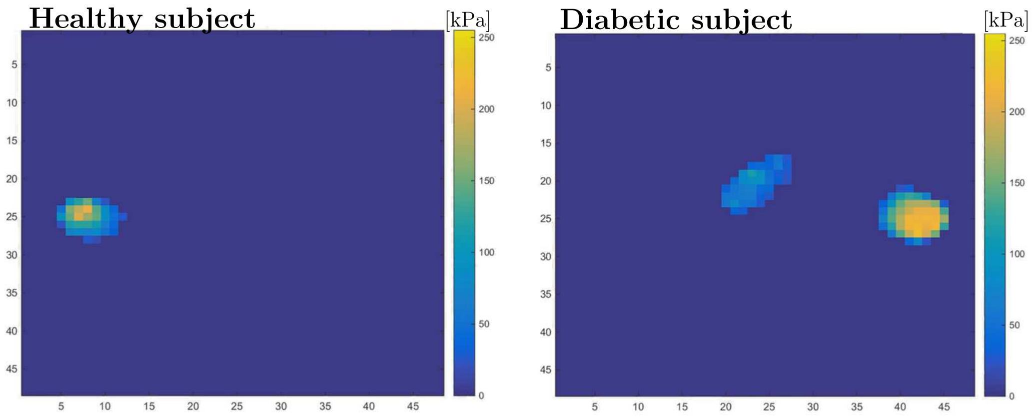

Figure 3.19 Contact pressure evaluated experimentally with the PP system, at 25% of the stance phase in gait cycle. On the left there are pressures for the healthy foot, while on the right the one for the diabetic. [Images: courtesy of DEI team]

These results are in good agreement with those evaluated experimentally through the plantar pressure system (Figure 3.19). Though the measured contact surfaces are smaller than in the finite element model, in the healthy foot the peak pressure is similar to the experimental one (0.24 MPa). As concerns the neuropathic foot, the finite element model predicts higher values of contact pressures (maximum peak is 0.42 MPa) that involves both hindfoot and forefoot areas. Let us consider in detail the possible motivations of this dissimilarity. First, the loading configuration is a simplification of the reality based on experimental data available and it probably anticipate the loading of the forefoot in the gait cycle, resulting premature contact pressure peaks. Second, the hyperelastic behavior of the diabetic tissue is assumed from literature two times stiffer than the healthy [9], as a reasonable assumption, but it is not a patient specific input: if the tissue of the patient is softer, the value of peaks will be lower, with a more diffused contact zone. Third, analogously to the tissue, the stiffness of the plantar fascia, ligaments and tendons are not patient specific as well. If the stiffness of these parts is too high, the *arch effect* is quite rigid and the foot becomes in contact rapidly with the forefoot area (Figure 3.20), without loading adequately the hindfoot contact surface. All these effects can be grouped in a future tuning phase of the model: when additional experimental material properties are available, they will be used to improve the model in mimicking experimental results.

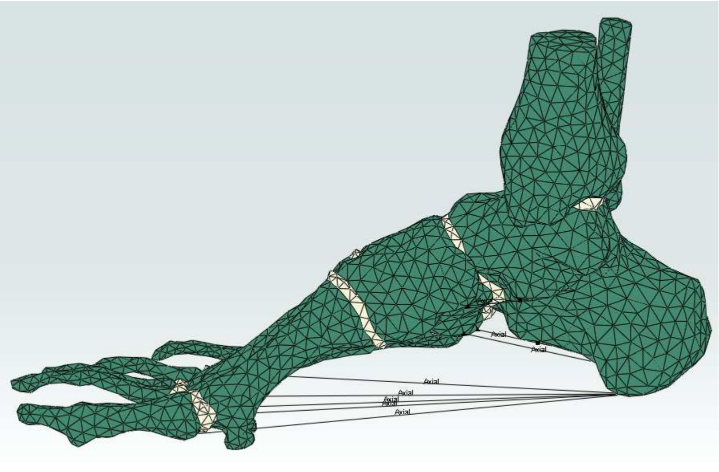

Figure 3.20 Arch effect in foot bones reached with tendons, ligaments and plantar fascia

Let us now consider strain field, effective stresses and interstitial fluid pressure. Contrarily to a usual approach in biomechanics, where the tissue of the foot is generally modelled with a hyperelastic material, by using the porohyperelastic constitutive law we enrich the numerical model with a real time-dependent behavior. The loading condition represents the evolution of the gait with time, mimicking the peculiarities of the patient specific gait cycle. In addition, the porous medium approach allows to split total stresses, which are the variables computed in hyperelastic models, into effective stresses and fluid pressure. A completely new scenario is then opened, due to the fact that stress peaks in these two variables are recorded in different points of the domain at a same time frame: total stress and effective stress peaks are different both in their value and in their spatial location.

If we look at Figure 3.22, at 25% of the stance phase in gait cycle peaks in fluid pressure are placed under the calcaneus in the healthy foot, whereas they interest also the forefoot area in the neuropathic subject, analogously to what was observed for contact pressures. Some peaks are interestingly revealed at the separation zones between different bone fragments: they are due to discontinuities introduced by different material properties (i.e. stiff bones and soft cartilages) and by angularities in the geometry.

By taking into account the effective vertical stresses in Figure 3.23, we can find predominantly compression components, due to vertical loading, but there are also some areas at the interface between bones and tissue, which are in traction, caused by the bone subfragments arch interaction on the surrounding tissue.

Finally, let us consider the strain field within the tissue domain. Due to the low stiffness of the plantar tissue (for both healthy and diabetic foot), values of strain field components are clearly high. If we compare the six components of the tensor, the maximum value is due to vertical strain: about 50% in the healthy subject and 65% in the diabetic one. Noteworthy peaks on shear strains γ_{yz} (see Figure 3.21) can be found again at the bone-tissue and cartilage-tissue interfaces, but also at the contact surface with the ground: it can be related to the constraint given by the friction with the ground (static friction coefficient of 0.6 implemented).

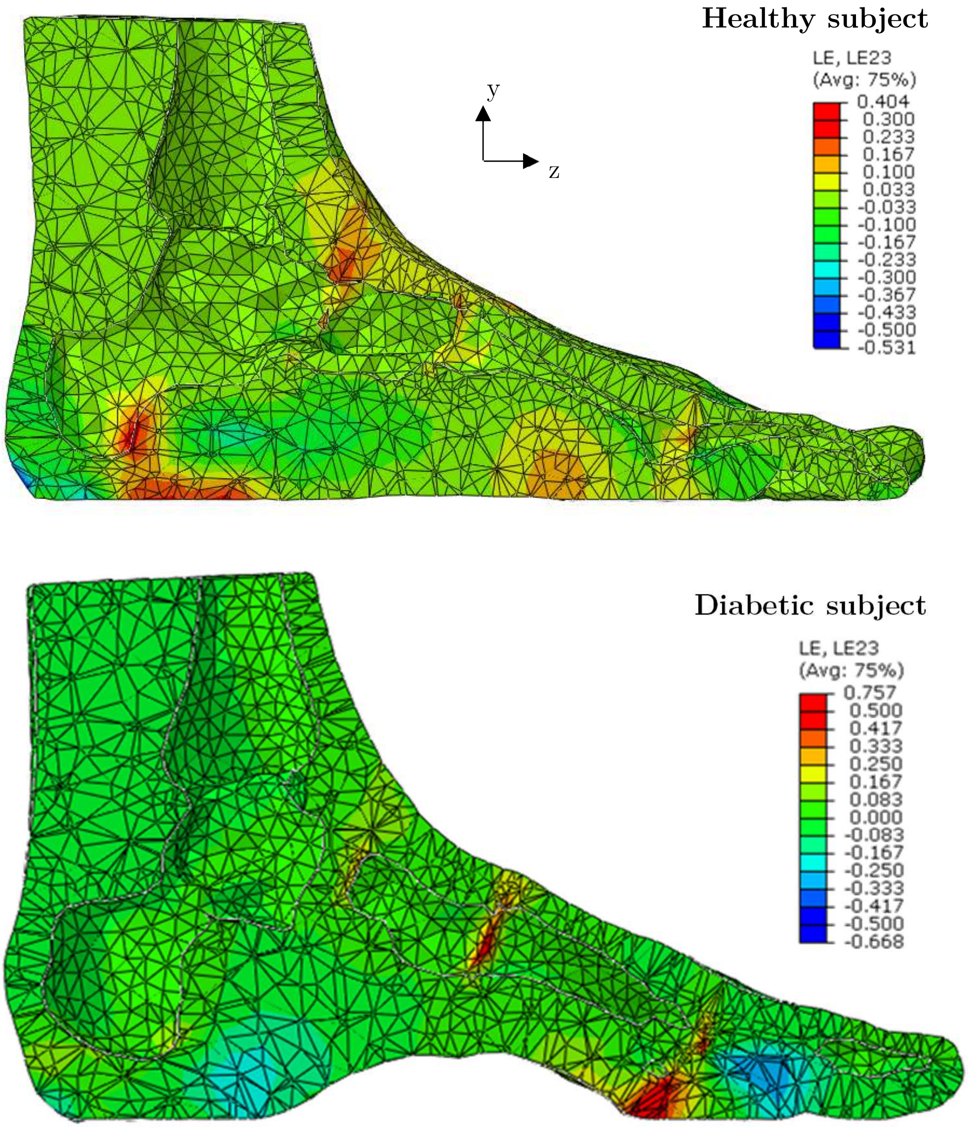

Figure 3.21 Contour plot of the shear strain (γ_{yz}) at 25% of the stance phase in the gait cycle for the 3D subject specific geometry

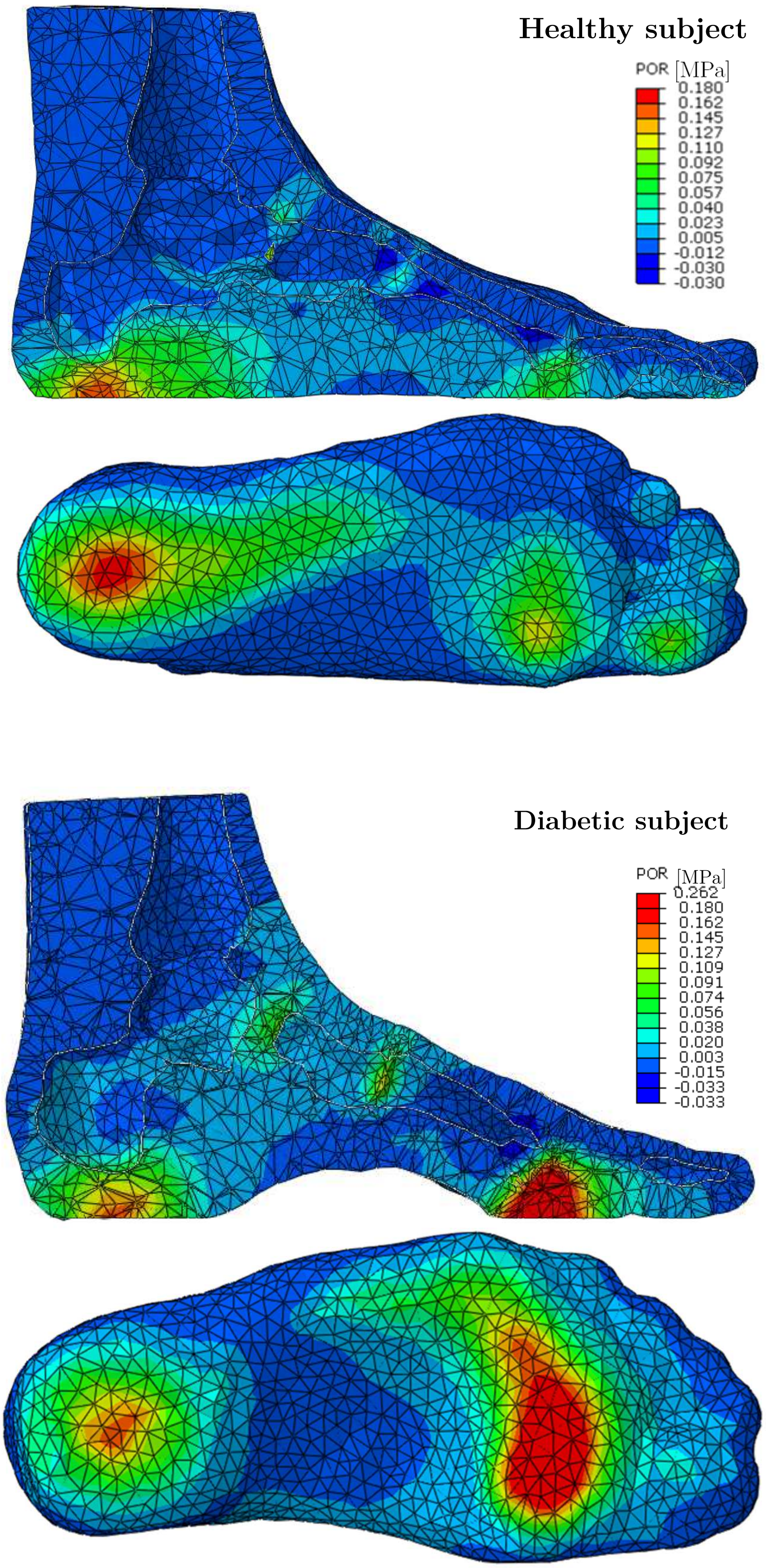

Figure 3.22 Contour plot of the Interstitial Fluid Pressure at about 25% of the stance phase in the gait cycle for the 3D subject specific geometry. For each model there are two plots: one section of the 2nd metatarsal-calcaneus on the top and a view of the foot sole at the bottom. (IFP is positive for compression)

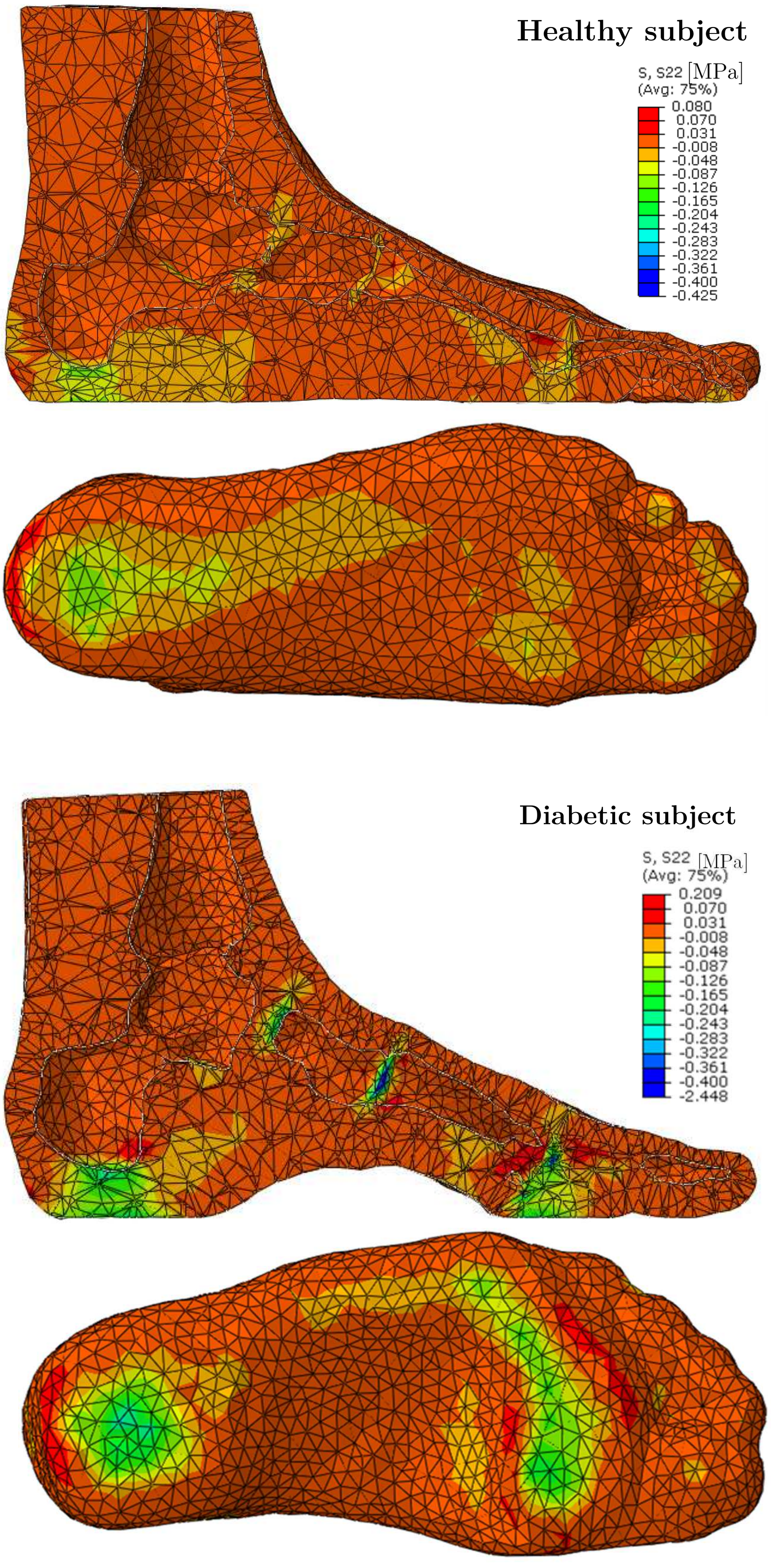

Figure 3.23 Contour plot of the effective vertical stress at about 25% of the stance phase in the gait cycle for the 3D subject specific geometry. For each model there are two plots: one section of the 2nd metatarsal-calcaneus on the top and a view of the foot sole at the bottom.

After having studied the behavior of the three-dimensional foot during the first part of the stance phase, we decided to consider a 2D model, to simulate multiple gait cycles and the development of the ulceration phenomenon. The use of a two-dimensional model is truly an efficient solution to prove the validity of our model while reducing the computational time.

In the following we will introduce first the results for the healthy foot, and second, we pass to the diabetic foot, to consider the possible development paths of the ulceration.

3.1.8.2. Four gait cycles in a 2D healthy foot

In this section four gait cycles (see §3.1.6) are considered in a healthy patient specific model. A further simplification is introduced: stiffer cartilages ($E = 700\ MPa$, $\nu = 0.4$) are considered instead of modelling ligaments, tendons and plantar fascia. In addition, no friction at the contact surface is considered.

First of all, let us consider the vertical strains (Figure 3.24) corresponding to the first $\left(t_{Ip}\right)$ and second $\left(t_{IIp}\right)$ load peaks in the fourth step (see Figure 3.12). Clearly the highest values of negative strains are under the heel (i.e. -25%, at the first loading peak) and below the metatarsal head (i.e. -30%, at the second peak); on the contrary, high positive strains can be found near the midfoot zone (~15%): they are caused by the compression of bone arch, which leads to an elongation of the zone at the bottom. With respect to deformation field, the high strain regime visibly confirms the need of a hyperelastic constitutive behavior, which can take into account large deformations in the plantar tissue. An inverse trend can be found by analyzing the horizontal strain at t_{Ip} and t_{IIp} (Figure 3.25). In the tissue under the calcaneus, when the first peak in vertical loading is applied, the horizontal expansion of the tissue takes place for the load, resulting a zone in the tissue that is in elongation (~50%).

Similarly, for $t = t_{IIp}$, under the metatarsal head positive strains can be found of approximately 55%. Contrarily, the area enclosed under the bone arch develops clearly negative strains (~10%), due to the zones in elongation at the hindfoot and forefoot.

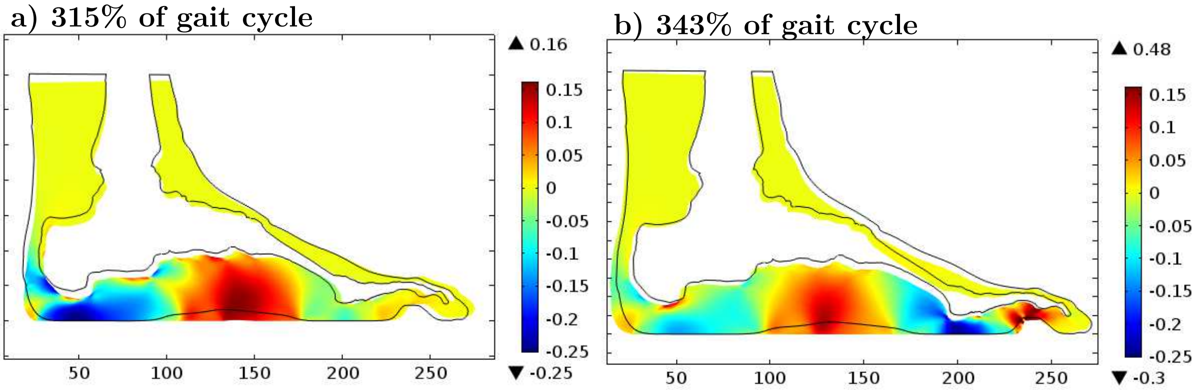
a) 315% of gait cycle

b) 343% of gait cycle

Figure 3.24 Contour plot of the vertical strain at the two vertical load peaks [a) 315%[13] and b) 343% of the gait cycle] at the fourth steps.

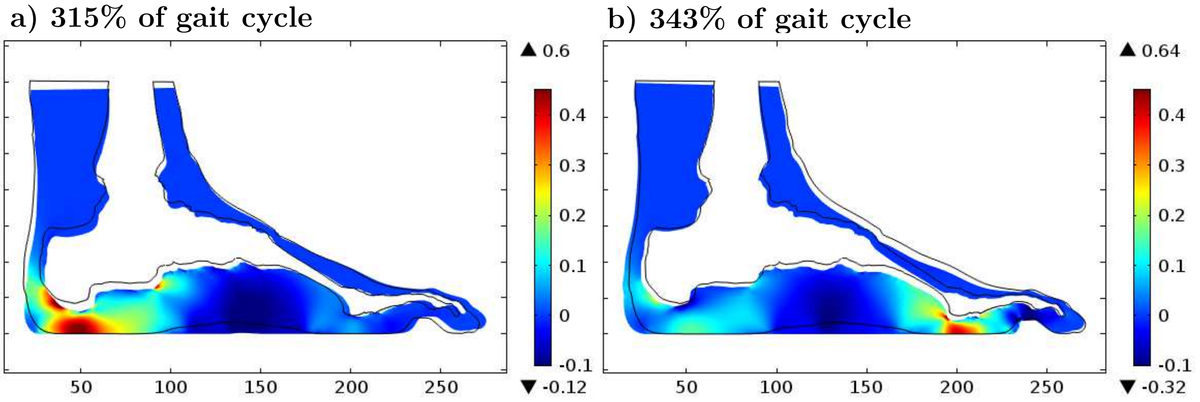
a) 315% of gait cycle

b) 343% of gait cycle

Figure 3.25 Contour plot of the horizontal strain at the two vertical load peaks [a) 315% and b) 343% of the gait cycle] at the fourth steps.

As previously introduced, the porous medium behavior allows to consider time with its real physical meaning. The length of the load path is of fundamental importance. For this reason, patient specific loading is properly taken into consideration, giving results that depend upon the duration of the step subphases and load peak instants.

---

[13] 315% and 343% of gait cycle are the time instants at the fourth steps when respectively the first and the second peak in vertical load are reached. (Figure 3.12)

The plantar tissue is modelled as a fully saturated porous medium (§3.1.3), made of a solid skeleton and an interstitial fluid. As a well-known process in geomechanics [68], [69], the *consolidation* (or better for our cases, the fluid-structure interaction) takes place when a porous medium is loaded and the excess of fluid within its domain drains out of it. When the load is applied, it is carried almost entirely by the water within the medium: as a consequence, at the beginning of the process the interstitial fluid pressure is equal to the load applied. As time goes on, the fluid pressure decreases, progressively transferring the load to the solid skeleton, with an increase of the effective stresses. We will see that this phenomenon affects also our model. In the following, vertical effective stresses, interstitial fluid pressure and total vertical stresses are recorded as a function of time in two points in the plantar tissue: under the calcaneus (P_1) and under the metatarsal head (P_2) (Figure 3.26).

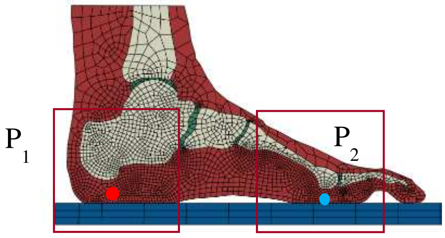

Figure 3.26 Points of evaluation of output variables for the hindfoot (red dot, (P_1)) and for the forefoot (blue dot, (P_2))

In P_1 the fluid-structure interaction phenomenon can be seen evidently in Figure 3.27: the cyclic load is transferred progressively from the fluid to the solid skeleton, with peak trends that are increasing for the effective stresses and decreasing in the IF pressure.

Furthermore, stress peak distribution is different for the total and the effective stresses (Figure 3.28). As a result, there could be different areas of potential ulceration, whether we consider one or the other stress component. If we compare total and effective vertical stress in P_1 (Figure 3.27 b,c), the maximum value of total stress remains constant in each step. On the contrary, the effective counterpart grows, highlighting an increasing risk of ulceration triggering with the number of steps.

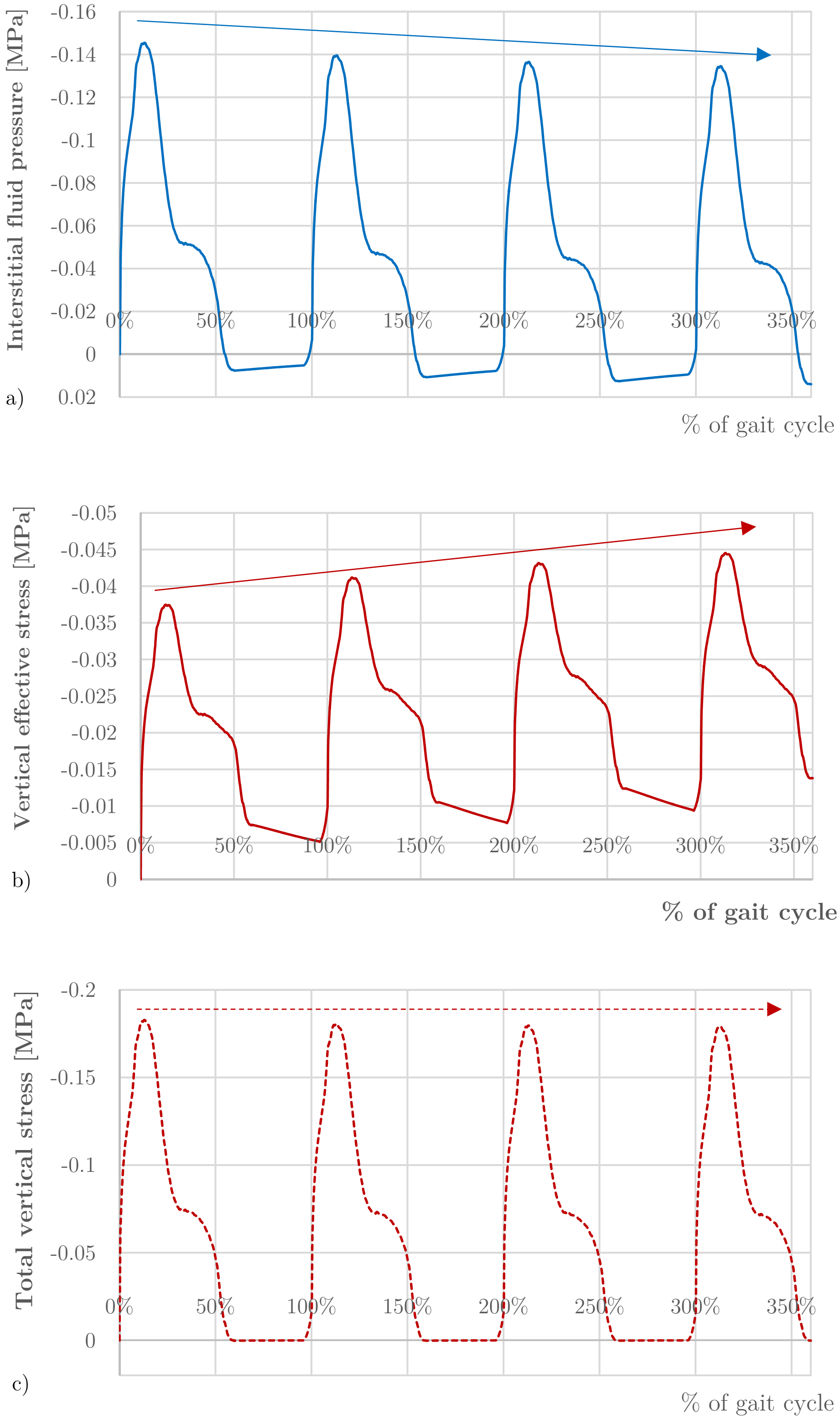

Figure 3.27 Graph of the interstitial fluid pressure (a), the vertical effective stress (b) and total vertical stress (c) as a function of the percentage of the gait cycle, evaluated in P_1. (IFP is positive for traction)

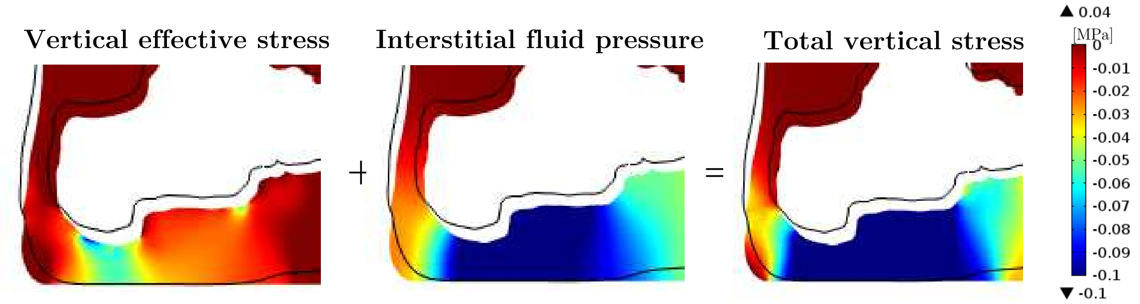

Figure 3.28 Comparison between stress peaks location at the same time (315% of gait cycle) for the hindfoot part of the foot. The position of the maximum value of vertical effective stress is clearly different from the total stress counterpart. (IFP is positive for traction)

Figure 3.29 gives a better insight of the phenomenon. The interstitial fluid pressure, total and effective vertical stresses are plotted for P_1 and P_2. The peaks under the calcaneus are reached earlier than in the metatarsal zone. These graphs reflect very well the loading condition of the foot, where the hindfoot is loaded first, then it starts to unload while the forefoot begins to be loaded, and finally almost only the forefoot is loaded. If indeed we superimpose the two graphs in Figure 3.29, we obtains a trend that recalls the initial loading condition seen in Figure 3.12 (i.e. the two peak trend of the vertical load).

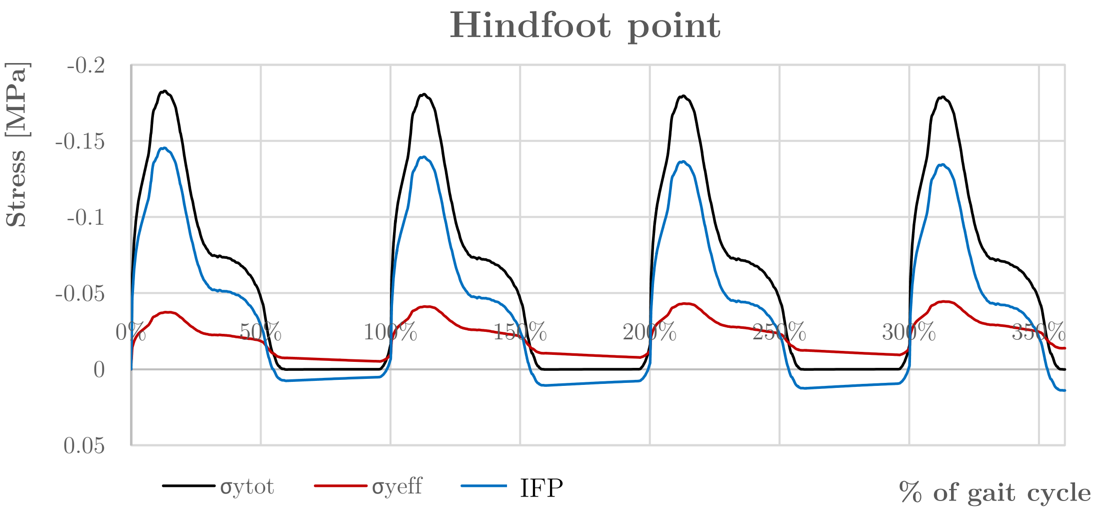

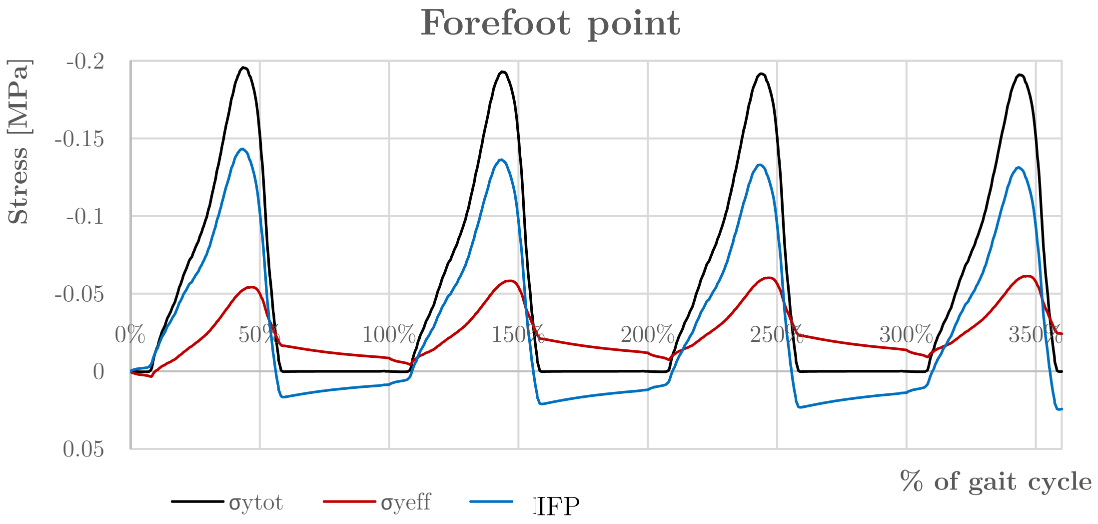

Figure 3.29 Trend of interstitial fluid pressure, total and effective stresses for four gait cycles at two reference point. (IFP is positive for traction)

In the mathematical formulation (§3.1.3) the rationale of the cell transformation from healthy to ulcerated was introduced: a limit stress is one of the key factors that trigger and guide the development of the ulcers. Three different variables that combines effective stress components are investigated, to define the most appropriate quantity as the ulceration index of risk: Von Mises stress, Tresca stress and Average pressure.

Von Mises criterion defines a specific threshold value of the deviatoric energy and is defined as:

$$\sigma_{VM} = \sqrt{\frac{1}{2}\left[\left(\sigma_x - \sigma_y\right)^2 + \left(\sigma_x - \sigma_z\right)^2 + \left(\sigma_y - \sigma_z\right)^2\right] + 3\left(\tau_{xy}{}^2 + \tau_{xz}{}^2 + \tau_{yz}{}^2\right)}$$

(3.59)

Figure 3.30a shows the distribution of VM stress for $t = t_{Ip}$ and $t = t_{IIp}$. The trend is evaluated at the VM peak points (Figure 3.30b) as a function of time, showing clearly a decrease of the maximum peaks as the number of steps increases. It seems that after multiple steps the fluid-solid interaction has a relieving effect on the shape variation. This trend is also illustrated in Figure 3.30c, where each component of (3.59) is displayed.

Let us consider the second variable: Tresca stress. This criterion limits the maximum shear stress:

$$\tau_{\max} = \max\left(\left|s_I - s_{II}\right|;\left|s_I - s_{III}\right|;\left|s_{II} - s_{III}\right|\right) \tag{3.60}$$

where s_I, s_{II}, s_{III} are the principal stress components.

It is similar to Von Mises criterion and gives almost the same result: in Figure 3.31 Tresca stress is shown, with peaks decreasing with the number of steps.

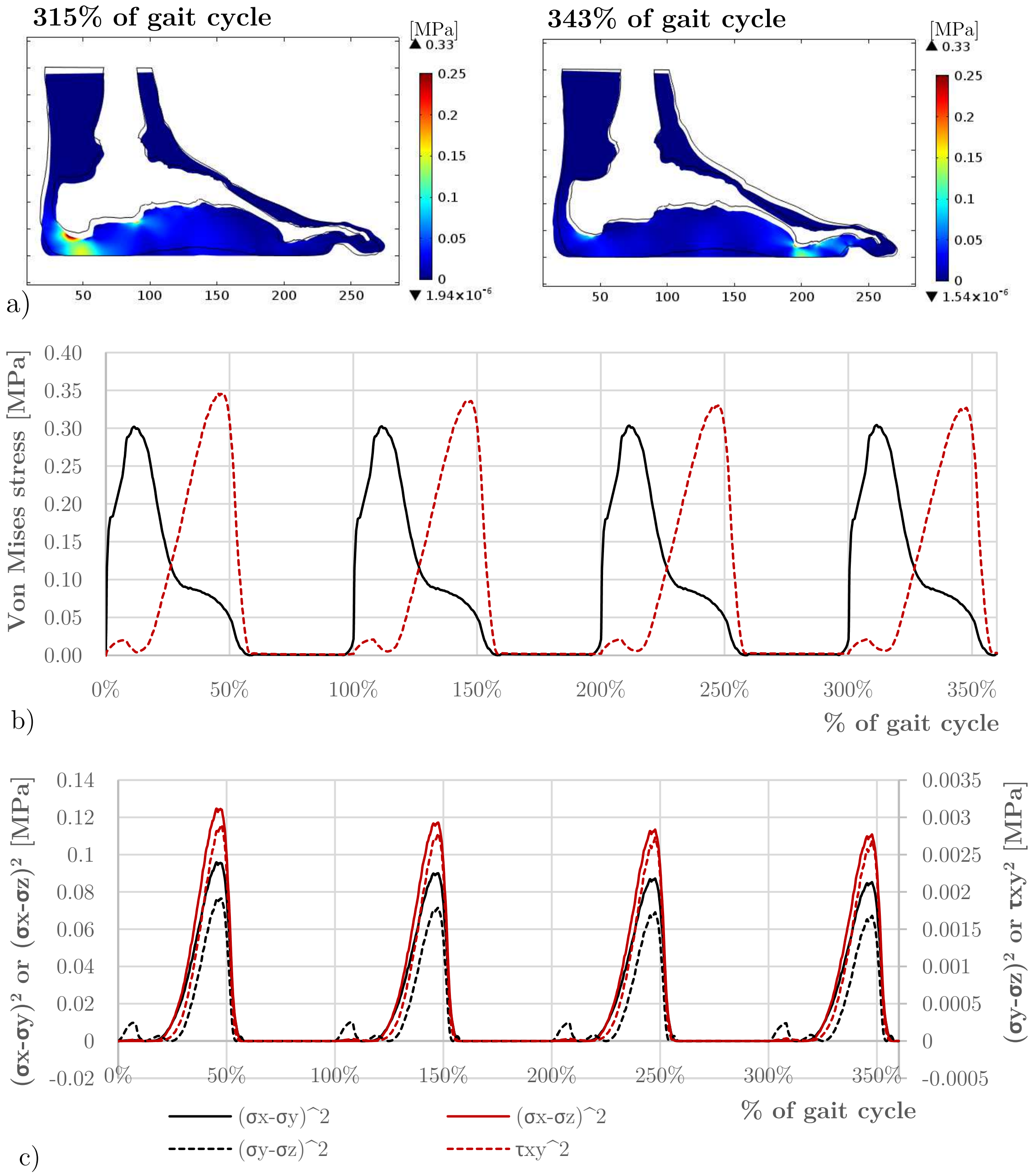

Figure 3.30 a) Contour plot of Von Mises stress at the two peaks in vertical loading at the fourth step. b) Graph of Von Mises stress in the points of stress peak (near calcaneus, with continuous line and near metatarsal head, with dotted line). c) Comparison of trends for each term in Von Mises criterion.

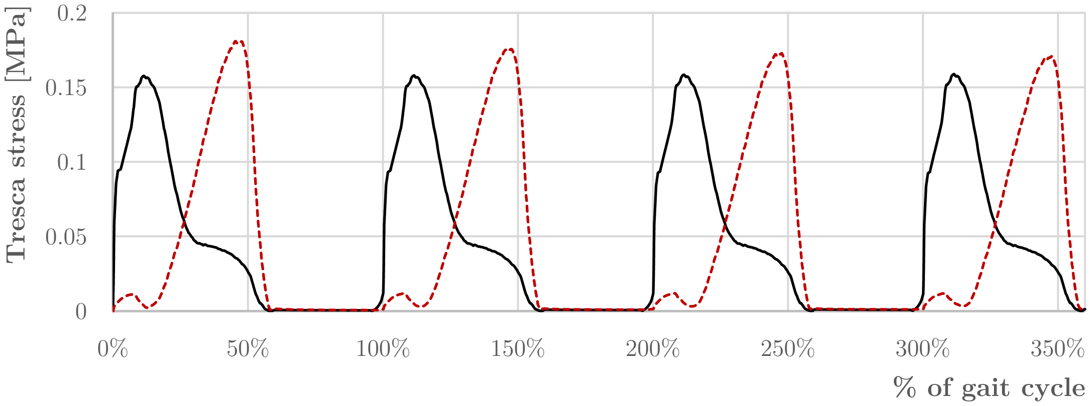

Figure 3.31 Graph of Tresca shear stress in the points of stress peak (near calcaneus, with continuous line and near metatarsal head, with dotted line)

We consider now the Average pressure, which is connected to the volume variation in the medium. The average effective pressure is defined as:

$$p = \frac{\sigma'_x + \sigma'_y + \sigma'_z}{3} \tag{3.61}$$

If we consider the trend of the average effective pressure in the peak points (Figure 3.32b), we can see that pressure peaks are increasing with the number of gait cycles, as the fluid-structure interaction develops. Furthermore, by observing the contour plot at $t = t_{Ip}$ and $t = t_{IIp}$ (Figure 3.32a), we can see that peaks are located in positions where usually takes place ulceration phenomenon [62], where there are bone angularities and, especially, under the metatarsal head tissue zone. Thus, starting from these observations, we decided to use the average pressure as the control variable in the ulceration triggering. Comparing VM stress and average pressure trends an interesting deduction can be done: the ulcer formation probably depends on the volume variation rather than on a shape change.

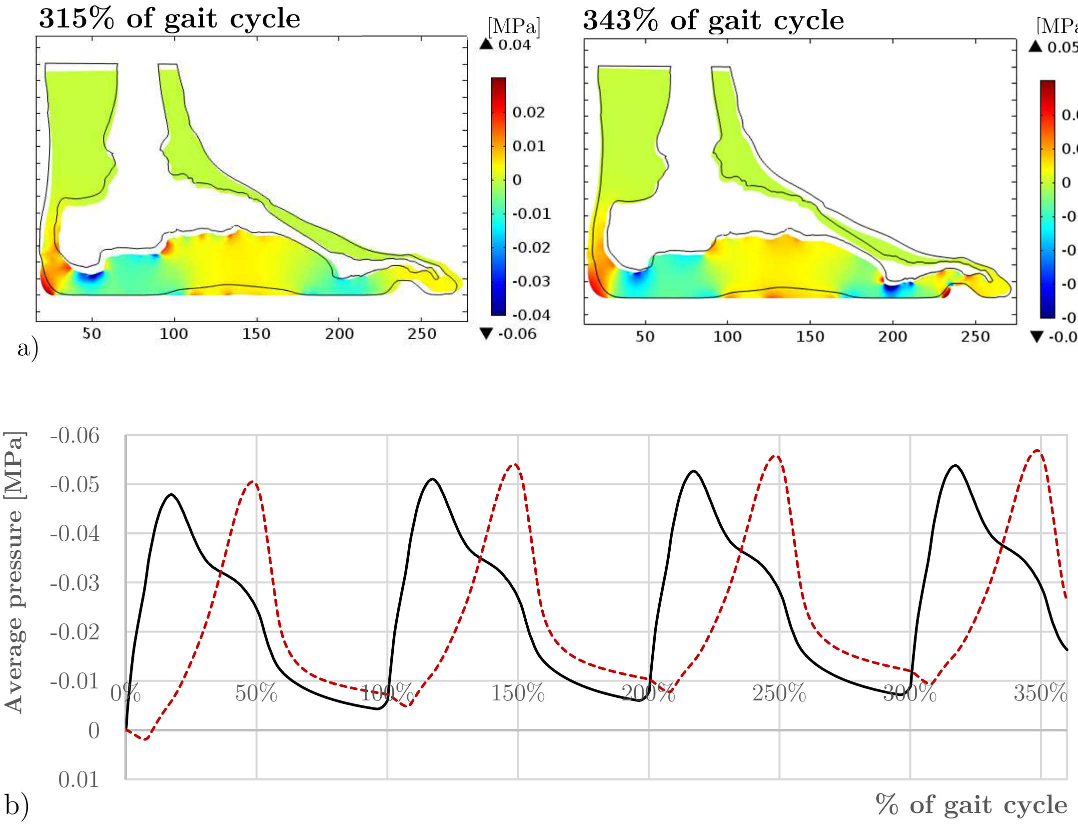

Figure 3.32 a) Contour plot of the average effective pressure at the two peaks in vertical loading at the fourth step. b) Graph of the average effective pressure in the points of stress peak (near calcaneus, with continuous line and near metatarsal head, with dotted line).

Due to the lack in literature of a specific stress threshold value for the triggering of ulcers, we based our assumptions on the output of our 2D model of the healthy foot. In particular, we choose a compressive threshold of 0.057 MPa and a tensile threshold of 0.12 MPa. Ulceration is probably mainly led by negative effective average pressure, in accordance with the contour plot in Figure 3.32a and the ulcer positions observed in experimental results.

3.1.8.3. Simulation of ulceration development in a 2D diabetic foot

As explained in the previous paragraph, we consider the average pressure as leading variable in ulceration (see (3.5)). The mass fraction of the ulcerated cell grows with increasing absolute average pressure, giving an intraphase mass exchange with the healthy cells in the solid phase. In this analysis no dissolution of ulcerated cells into fluid phase is considered ($\overset{Us\to f}{M} = 0$ in (3.4)).

Let us firstly analyze the reference variable values at two points in the tissue (Figure 3.33): in the calcaneus zone (P_3) and within the metatarsal area (P_4). If we compare the results for the diabetic foot (Figure 3.34) with the healthy foot (Figure 3.29), we can see that maximum values of the interstitial fluid pressure and effective stresses are evidently higher in the neuropathic foot. It is a consequence of different morphology of the foot and of the constitutive behavior of the solid skeleton in the tissue. The diabetic foot is stiffer than the healthy foot in accordance with [9] and it reaches higher values of stresses within the tissue domain.

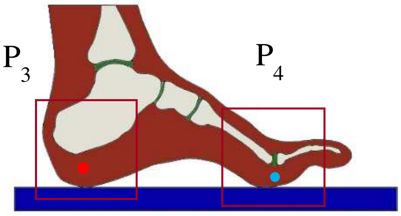

Figure 3.33 Point of evaluation of output variables for the hindfoot (P_3, red dot) and for the forefoot (P_4, blue dot)

Finally, we considered the evolution of the mass fraction of ulcerated cells. Two principal areas are affected by the ulceration. The first one is located under the calcaneus, at the interface between bone angularities and soft tissue and at the contact surface with the ground. The second group of ulcers triggers at the interface between the metatarsal head bones and the tissue, and it develops throughout the entire tissue depth (Figure 3.35 and Figure 3.36).

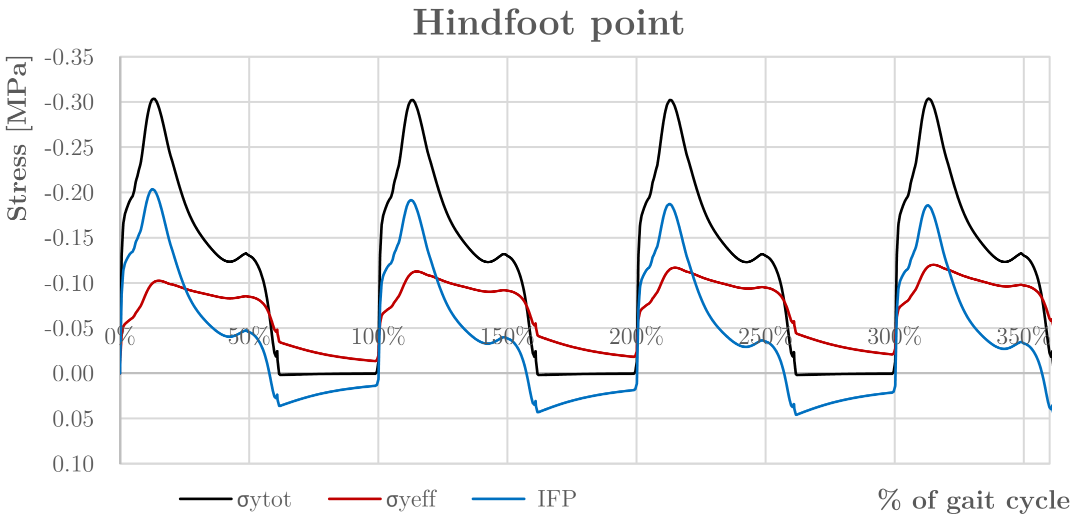

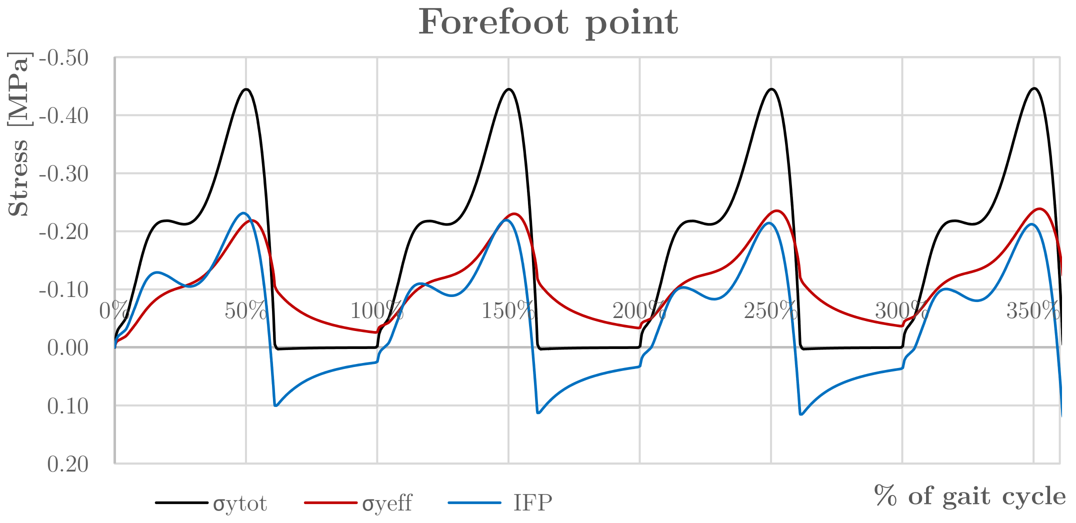

Figure 3.34 Trend of interstitial fluid pressure, total and effective stresses for four gait cycles at two reference point. (IFP is positive for traction)

Although the first ulceration zone is less recurring in diabetic subjects, the ulcers under the metatarsal heads are frequently occurring. The metatarsal head zone is indeed one of the most stressed in the plantar tissue: if we look at the foot geometry in Figure 3.5, the thickness of the tissue in this zone is lower than in the heel. Thus, this thicker elastic layer less efficaciously soften the transfer of the load from metatarsal head bone to the ground. An additional factor that accentuate this phenomenon is that the highest peak in vertical load takes place after midstance, mainly involving the loading of the forefoot area (Figure 3.7 and Figure 3.11). In reality, these stress peaks under metatarsal heads are further sharpened by the callus formation at the contact surface with the ground. Calluses are the protective response of the tissue to stress concentrations. They are stiffer than the tissue and, as a consequence, accentuate the stress peaks, promoting the ulcer triggering.

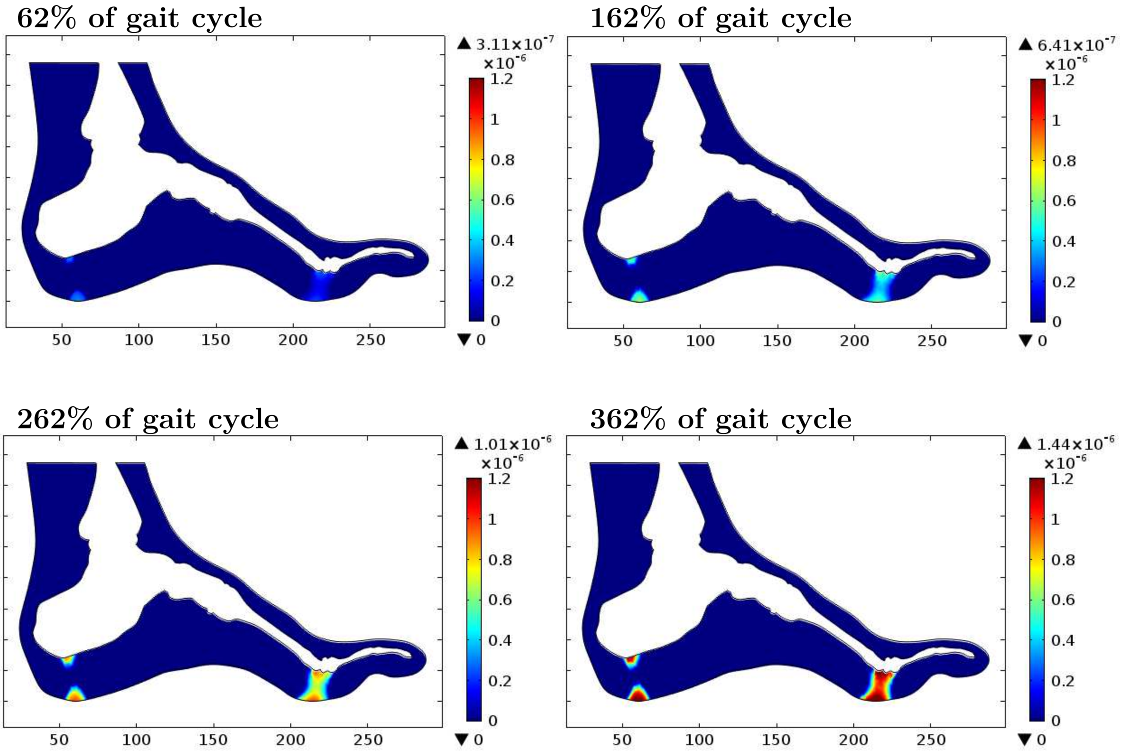
62% of gait cycle

162% of gait cycle

262% of gait cycle

362% of gait cycle

Figure 3.35 Contour plot of the ulcer development at the end of the stance phase in each gait cycle.

If we look at Figure 3.37a, we can see the ulcer developing mainly in the initial phase of each gait cycle, and it does not grow from almost 50% to 100% of each step. The pressure limit is initially exceeded in the first part of the gait cycle. As the fluid-structure interaction proceeds, the time interval with higher pressure than the limit increases (Figure 3.37b). As a consequence, the longer we are above the threshold, the bigger chance to develop an ulcer. By considering the pressure peak point in the metatarsal head zone, a similar trend can be found (Figure 3.38), with ulceration triggering time starting at about 40% of gait cycle. Due to the higher values of pressure reached, larger time intervals of ulcer development can be observed in the forefoot.

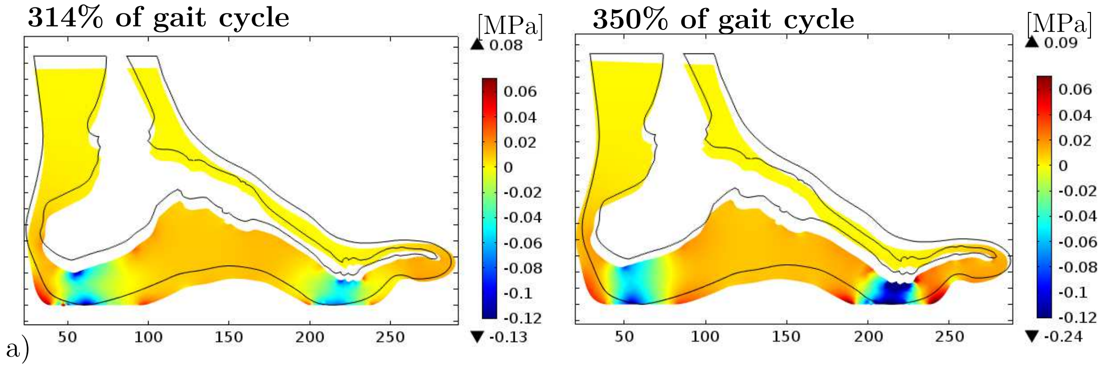

Figure 3.36 Contour plot of the average effective pressure at the two peaks in vertical loading at the fourth step.

It is worth to remark that there is a time shift in the development of the ulceration in the heel and in the forefoot (Figure 3.37a and Figure 3.38a). Since the vertical force moves from the hindfoot to the forefoot, the heel is loaded firstly and then the metatarsal head area.

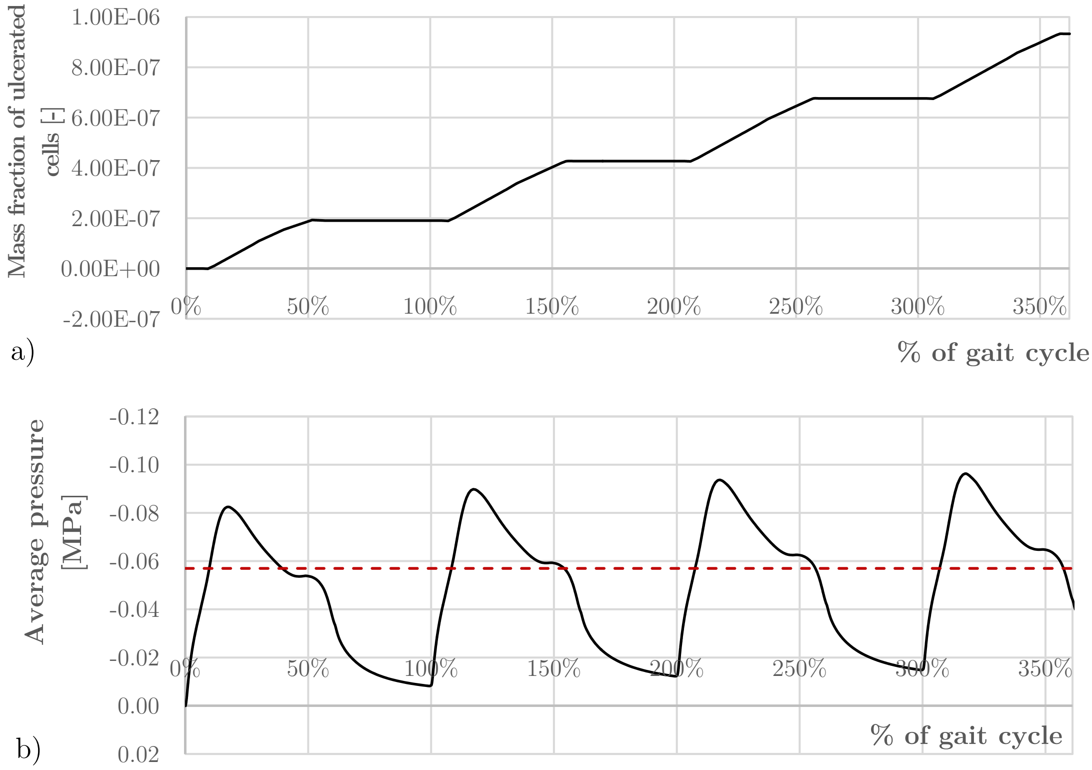

Figure 3.37 a) Graph of the ulcerated cell mass fraction near the average pressure peaks in the heel. b) Graph of the effective average pressure (continuous line) at the same point, and the threshold compressive pressure (dotted line).

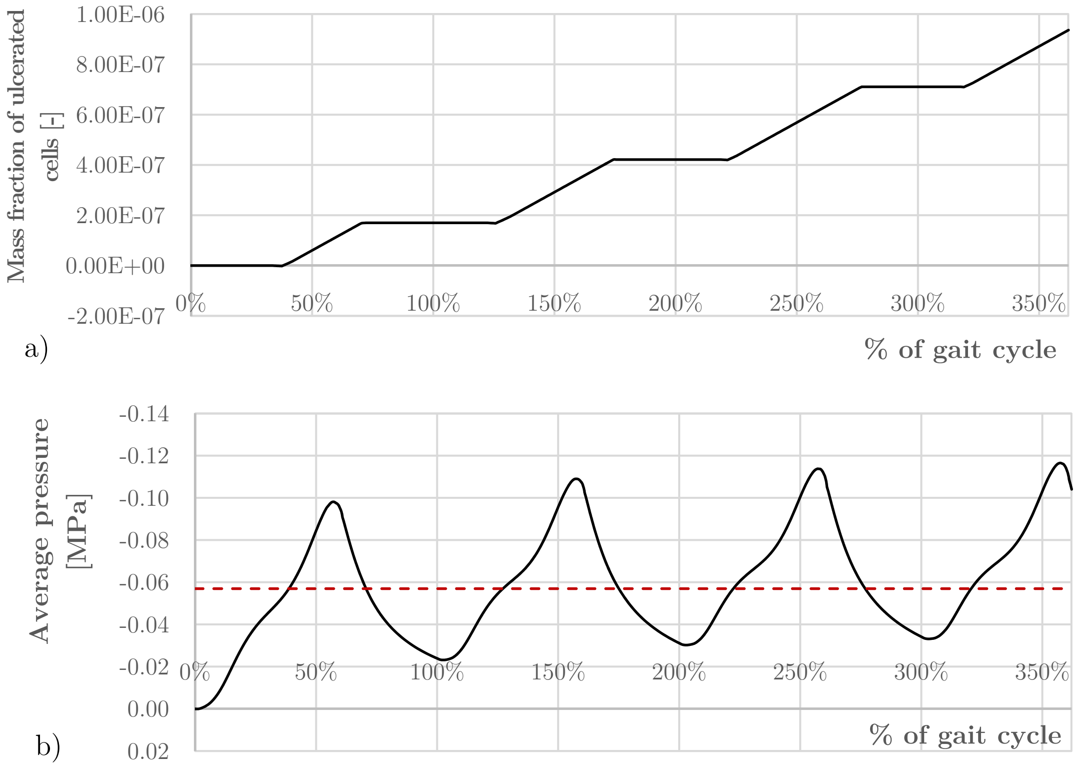

Figure 3.38 a) Graph of the ulcerated cell mass fraction near the average pressure peaks in the metatarsal head zone. b) Graph of the effective average pressure (continuous line) at the same point, and the threshold compressive pressure (dotted line).

3.1.9. Conclusions and perspectives

The presented mathematical model was applied to the case of a diabetic foot. Experimental tests allowed us to define patient specific data as inputs of our model: in this way, the geometry of the domain and loads applied are peculiar of the subject. Concerning material characteristics, though the lack of values for the parameters, extensive literature research allowed us to obtain input data for the model. In particular, where the uncertainty on the parameters were high, an OAT sensitivity analysis were made, to assess the influence of the parameter on the model results.

The porous media approach introduced some innovative aspects. First, the concept of time as a variable with a physical meaning: specificities of gait cycles are taken into account, contrarily to usually-adopted time independent hyperelastic approaches. Second, the presence of fluid and solid phases in the medium allows us to obtain different distributions of stresses, whether total or effective value are considered. Third, as a consequence of the fluid-solid interaction, an increasing trend of effective stress peaks with the number of steps is recorded.

These different aspects are considered in the study of the ulceration risk. In literature, specific ulceration stress limits are not available. As a consequence, we took advantage of the stress peaks in the healthy foot to define a pressure threshold for the diabetic one.

Though in this study simplified loading and only four gait cycles are considered, the results obtained are promising. The location and the development of ulcers are in agreement with experimental observations, and numerical results allows us to hypothesize that ulcer formation is linked to a volume variation rather than a shape modification.

The future perspectives are certainly focused to improve the model: on one hand we want to study the development of the ulceration in the 3D foot, by also perfecting both the loading configuration and the patient specific material values. On the other hand, we want to enrich the model by adding biological stimuli: the lack of oxygen dispersed within the fluid phase could be a useful parameter in contributing to the ulceration risk.

3.2. Scaffold for biomechanical applications

3.2.1. Introduction

Tissue engineering is nowadays a growing branch of medical sciences, thanks to the progress in technology and the frequent collaborations among physicians, engineers and scientists. According to [70, p. 107], it is defined as "an interdisciplinary field that combines the knowledge and technology of cells, engineering materials, and suitable bio-chemical factors to create artificial organs and tissues or to regenerate damaged tissues".

In order to reach this purpose, there is a need of design specific structures capable both to promote the recall of specific cells and to provide adequate stimuli for their differentiation to define the final tissue requested. In this context, a *scaffold* is the specific structure that gives a temporal artificial (mechanical and biochemical) support in the tissue formation process. It is a high porosity structure which chemical composition must provide the right signal to cells and, at the same time, it must supply adequate mechanical support to them in the whole phases of the tissue formation [71]. According to [72], [73], mechanical stresses within the scaffold fulfill an essential role in tissue definition: specific loading conditions can promote particular cell differentiation. Furthermore, the number of voids, their size, 3D distribution and interconnection are fundamental parameters to guide the process appropriately [74]–[76]: the network of pores should create open paths for the access of oxygen, nutrients and for the removal of cell waste products. In addition, scaffolds must be clearly biocompatible, because they have to be transplanted into a human body: their chemical composition has to stimulate a specific tissue creation, avoid the tissue rejection and promote an entire degradation of their structure as the tissue formation proceeds [71], [77].

Within a scaffold, complex biological phenomena take place: cell seeding, cell migration and proliferation, cell differentiation, blood vessel formation, consumption of nutrients are only some examples. Taking advantage of computer aided numerical simulation, great effort has been made in the last decades to mimic and foretell some of these processes, giving valuable information to improve the design and the efficiency of the scaffolds.

Different modelling techniques are developed, depending upon the features of the phenomenon considered. Scaffolds can be schematized sometimes as a biphasic porous medium, made of a solid skeleton and an interstitial fluid that fills the pores. In this case, it is considered as a continuum, with no sharp interfaces between phases. One possible approach in the design phase of such modelled scaffolds is the use of the homogenization technique: starting from a representative volume element of the scaffold (RVE), macroscopic properties (e.g. Young's modulus and permeability) are derived through an averaging process within the volume of the unit cell [78]. In this way, by studying different representative cell properties, it is possible to design specific scaffold structures (of fixed effective stiffness or permeability) targeted to induce the tissue requested [79].

Along with mechanical stimulus, another governing factor in the tissue formation is the fluid flow: the velocity of the interstitial fluid influences the cell seeding, depending on the dimension, interconnection and distribution of the pores. Linked to this, bioreactors[14] are often used in tissue engineering to ensure a uniform distribution of fluid within the scaffold and, as a consequence, a homogenous cell population [80], [81]. By considering the computational counterpart of this phenomenon, scaffolds are modeled as a truly 3D porous structure in which fluid flow is modelled using computational fluid dynamics analysis [73], [82], taking into account the effects of the velocities, as well as the influence of pore distribution. In this case, the definition of a reliable geometry of the scaffold becomes a fundamental

---

[14] A *bioreactor* is a device or a system used in tissue engineering to grow cells or tissues in the field of cell culture.

task. Thanks to micro-Computed Tomography and Nuclear Magnetic Resonance, the three-dimensional structure of the scaffold can be reconstructed, allowing also to compute the properties of the pores (e.g. size, interconnection and specific surface area).

From the early 60's numerous researchers started to analyze the biological and mechanical factors involved in the formation of tissues. One of the pioneers in this field was Pauwels [83]: firstly he theorized first an association between mechanical stimuli and specific tissue development. He assumed that the formation of collagenous fibers could be promoted by distortional shear stress, whereas hydrostatic compressive pressure helped the creation of cartilage. As regards bone formation, he supposed that it could be supported by a low strain regime, as well as maintained at a low strain rate to proceed with the endochondral ossification. Though his hypotheses were based on clinical observations, at that time he was not able to define specific limit values of stresses and strains triggering tissue differentiation. A step forward in this sense was taken by Carter [72], [84]. He introduced different domains of strain, hydrostatic pressure and octahedral shear stress, with different states of vascularization, promoting the formation of specific tissues. Along with the theoretical aspects of his work, finite element analyses were used as an effective tool in the study of his insights about tissue differentiation.

In the late 90's a true innovation was introduced by Claes and Heigele [85], [86]; in their research, they compare stress and strain fields obtained from numerical analyses with histological outcomes from animal experiments. In this manner they were able to define the domains of strain and hydrostatic pressure with specific boundary thresholds that trigger a specific tissue definition. In the following years some further advances of this model were brought in the bone healing context by Ament and Hofer [87] and Shefelbine [88], by introducing additional guiding factors of the differentiation process.

In the same years Prendergast and his team developed a different mechano-regulation model for tissue differentiation [16], [89]–[93], which introduced the fluid flow velocity as additional variable. They used a biphasic modelling of tissue, in which tissue differentiation is guided by a mechano-regulation algorithm that combines the effects of the interstitial fluid velocity and the octahedral shear strain.

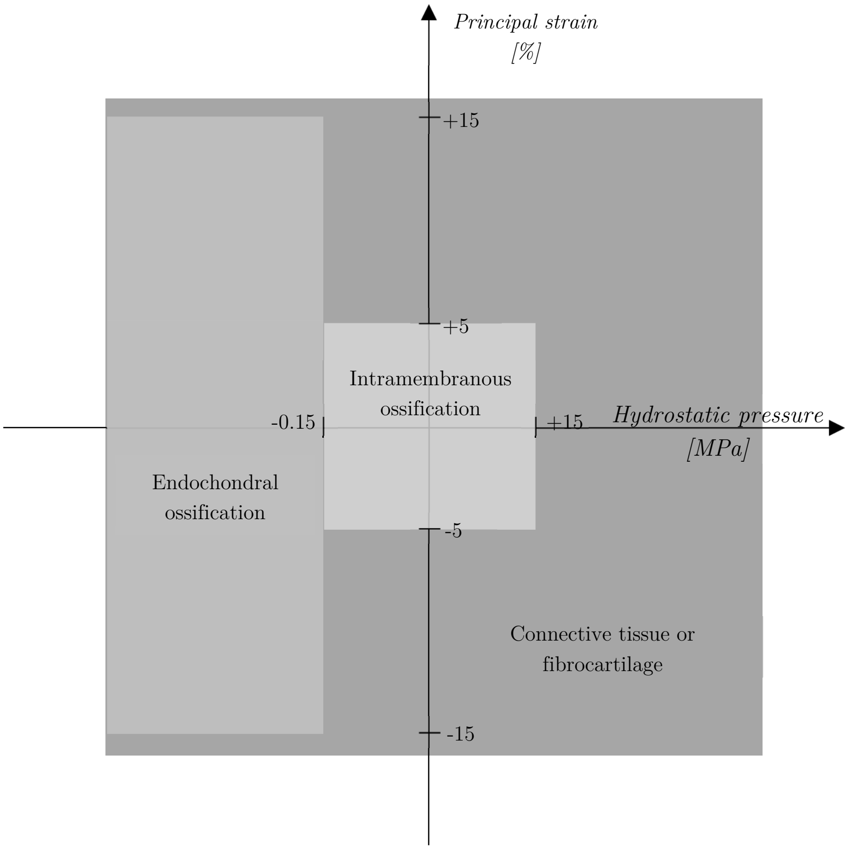

Figure 3.39 The Claes and Heigele threshold for tissue differentiation during fracture healing (re-elaborated graphics from [86])

Thanks to the collaboration with the *Houston team,* in this thesis we dealt with two types of scaffolds: a single-material scaffold, used for spinal fusion, and a multi-layer composite scaffold for the repair of osteochondral defects. This collaboration was born from their needs of having a numerical tool that could be used to improve the geometry of the scaffold in a post-surgery perspective of faster tissue formation. Thus is still an ongoing work, in the future it will be improved with new experimental data. Nevertheless, it is a good starting point for an effective exploitation of numerical models for the development of loading procedures and geometries, targeted to a final tissue creation.

3.2.2. Scaffold for spinal fusion

In case of bone damaging, due to injury, degenerative diseases, cancer or post-operative defects [6], bone augmentation is one of the ways to restore the functionality of the structure. The supply of materials or tissue allows the bone to return to its initial condition, through a bone augmentation process [94]. This result can be achieved through different strategies [6]: one of the most common techniques adopts autologous bone, using patient specific bone tissue as starting material for bone augmentation process. Mainly due to the high post-operative period and surgical complication, a second technique, which exploits allografts, was introduced as a possible improvement. However, the risk of rejection and disease transmission, caused by the use of not autologous bone, led clinicians to explore new solutions for a more straightforward bone augmentation process. The research of synthetic materials, as a solution to the complications connected to both autologous bone and allograft techniques, was surely a challenging task in the last decades. A truly turning point was reached when researchers focused on *biocompatibility* property of those innovative materials: with the specific aim of reducing adverse effects related to the use of synthetic products, osteoconductive and osteoinductive materials were studied. These materials should possess the properties of supplying a structure to permit the bone growth [95], [96] as well as of exhibiting specific stimuli that can recall the undifferentiated cells and guide them into the differentiation process, to reach the requested final tissue. A further step forward was clearly the addition of the *biomimicry* property: such materials should not only induce the bone formation, but also resemble the target tissue [97], by creating an environment that should be as similar as possible to that in the human body, during the bone formation process.

If we focus on the spinal fusion surgery, it is commonly used as a treatment for different disease, such as spinal disc herniation, vertebral fracture, spinal tumor and any condition that causes instability of the spine. The surgical procedure is designed to fix the relative motion at a vertebral segment to decrease the pain generated from the joint. A rigid connection between vertebrae is reached by inserting additional bone tissue (i.e. autograft, allograft or artificial), to promote a solid link through the bone augmentation process. In case of use of artificial bone promoters, in the last years scaffolds are commonly adopted for their properties of rapidly inducing bone formation (see §3.2.1). In this surgical procedure the scaffold is implanted between two vertebrae. After scraping the surfaces of the two adjacent spine bones, to create a housing for the extremities of the scaffold, the mesenchymal stem cells start to access the porous structure from its top and bottom faces, triggering the tissue formation process and allowing to firmly solder the painful vertebral segment.

In this context, the *Houston team* developed a bio-inspired scaffold, to use in the bone augmentation process in the spinal fusion [6]. This scaffold, made of magnesium-doped hydroxyapatite/type I collagen, is indeed capable to express chemo-physical and morphological cues of human osteogenic niche, engineered bearing in mind the biomimicry property target of the scaffold. Due to the fact that magnesium is one of the most abundant ions in bone during osteogenesis, inserting it in the scaffold structure allows indeed to reproduce the osteogenic environment.

This innovative material was reported to have a high osteoinductive potential, confirmed by *in vitro* experimental results. Furthermore, the capability of promoting bone formation was confirmed by results from *in vivo* ectopic rabbit model. By focusing on the *in vivo* experiments, one cylindrical scaffold (1cm of diameter, 3 cm of height) was implanted subcutaneously into pocket surgically created on the back of the rabbits. The change in density and the volume of bone types (i.e. trabecular and cortical bone) were measured in a time period of six weeks at specific intervals (i.e. at 24h, two, four and six weeks). From experimental results, the scaffold shows its potentiality of developing substantial volume of trabecular bone in only two weeks from the implant, and a not negligible quantity of cortical bone at the end of the measurements. In Figure 3.40 the volume of both trabecular and cortical bone during the time period of the experiment are represented.

Starting from these results and as a response to *Houston team* needs, we developed a preliminary computational model that could be capable to mimic the evolution of the bone formation in the six week measurements in order to study the effects of the loading of the scaffold on the specific tissue differentiation.

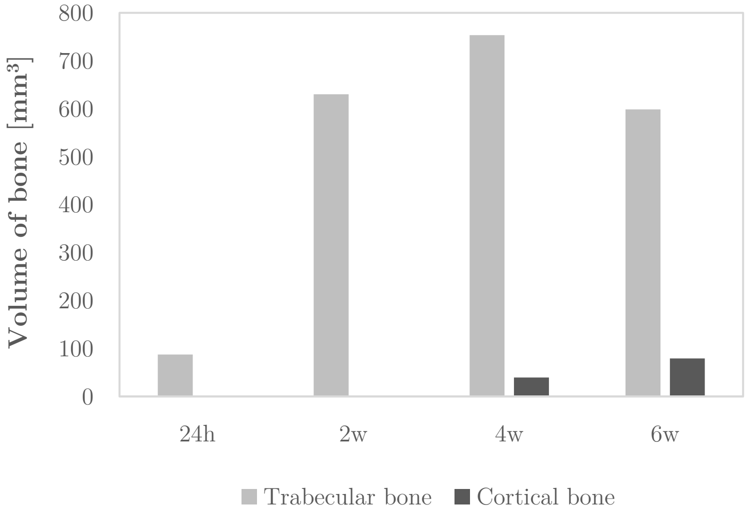

Figure 3.40 Volume of the bone within the scaffold in rabbit ectopic site at 24h, 2w, 4w and 6w. Courtesy of Houston team, [6].

3.2.2.1. The mathematical model

By taking advantage of the model developed for the plantar tissue in the diabetic foot (§3.1.3), the scaffold was modelled as a porous medium, made of a solid skeleton (cells and extracellular matrix) fully saturated by an interstitial fluid. Due to limited experimental data at this stage, in our model mesenchymal stem cells differentiate during time into trabecular bone; trabecular bone, at later time of the experimental measurement, transforms into cortical bone, following the trends shown in Figure 3.40. Three different species[15] are considered within the solid phase of the medium:

---

[15] Each species comprises also the ECM.

the mesenchymal stem cells (*MSC*), the trabecular bone (*T*) and the cortical bone (*C*). The mass conservation for each species can be written respectively as:

$$\frac{\partial\left(\varepsilon^s\rho^s\omega^{MSCs}\right)}{\partial t}+\nabla\cdot\left(\varepsilon^s\rho^s\omega^{MSCs}\mathbf{v}^s\right)+\varepsilon^s r^{M-Ts}=0 \tag{3.62}$$

$$\frac{\partial\left(\varepsilon^s\rho^s\omega^{Ts}\right)}{\partial t}+\nabla\cdot\left(\varepsilon^s\rho^s\omega^{Ts}\mathbf{v}^s\right)-\varepsilon^s r^{M-Ts}+\varepsilon^s r^{T-Cs}=0 \tag{3.63}$$

$$\frac{\partial\left(\varepsilon^s\rho^s\omega^{Cs}\right)}{\partial t}+\nabla\cdot\left(\varepsilon^s\rho^s\omega^{Cs}\mathbf{v}^s\right)-\varepsilon^s r^{T-Cs}=0 \tag{3.64}$$

where the symbolism is the same used in the general theory (§2.2.5), with the superscripts *MSC*, *T* and *C* to mesenchymal stem cells, trabecular and cortical bone respectively referring, and s is representative of a solid phase mass conservation.

By taking into account the entire interstitial fluid phase, its mass conservation equation can be obtained from (3.13)[16] :

$$\frac{\partial\left(\varepsilon^f\rho^f\right)}{\partial t}+\nabla\cdot\left(\varepsilon^f\rho^f\mathbf{v}^f\right)=0 \tag{3.65}$$

The intraphase exchange term $\varepsilon^s r^{M-Ts}$ in (3.62) and (3.63) governs the transformation of the MSC mass fraction into trabecular bone, while $\varepsilon^s r^{T-Cs}$ in (3.63) and (3.64) regulates the transformation of trabecular into cortical.

These terms can be written using a constitutive relation introduced by Preziosi and Vitale [50], [51], conveniently modified:

$$\varepsilon^s r^{MSC-Ts}=\begin{cases}Pf\left(1-\omega^{Ts}\right)\varepsilon^s \quad for\ t\le t^{Ts},\ \omega^{Ts}\left(t^{Ts}\right)=1\\ 0 \quad for\ t>t^{Ts},\ \omega^{Ts}\left(t^{Ts}\right)=1\end{cases} \tag{3.66}$$

---

[16] By summing over all the species in the fluid. We are interested only to the mass conservation of the entire fluid phase, so no additional details about different species in fluid phase are reported.

$$\varepsilon^s r^{T-Cs} = \begin{cases} Ph\left(1-\omega^{Cs}\right)\varepsilon^s \quad for\ t \le t^{Cs},\ \omega^{Cs}\left(t^{Cs}\right)=1 \\ 0 \quad for\ t > t^{Cs},\ \omega^{Cs}\left(t^{Cs}\right)=1 \end{cases} \tag{3.67}$$

where f and h are two time-dependent functions chosen to fit experimental data, while P is a pressure factor (with $P \le 1$) defined as follows:

$$P = \begin{cases} 1 \quad if\ \left|p_m\right| \le p_{mLim} \\ \left(\dfrac{p_{mLim}}{\left|p_m\right|}\right)^{1.5} \quad if\ \left|p_m\right| > p_{mLim} \end{cases} \tag{3.68}$$

where p_m is the effective average pressure and $p_{mLim} = 0.15\,MPa$.

By applying (3.66) and (3.67) we can write equations (3.62), (3.63) and (3.64) in the material reference frame as:

$$\frac{\partial \omega^{MSCs}}{\partial t} = \frac{1}{\rho^s \varepsilon^s}\left(-\varepsilon^s r^{MSC-Ts}\right) \tag{3.69}$$

$$\frac{\partial \omega^{Ts}}{\partial t} = \frac{1}{\rho^s \varepsilon^s}\left(\varepsilon^s r^{MSC-Ts} - \varepsilon^s r^{T-Cs}\right) \tag{3.70}$$

$$\frac{\partial \omega^{Cs}}{\partial t} = \frac{1}{\rho^s \varepsilon^s}\left(\varepsilon^s r^{T-Cs}\right) \tag{3.71}$$

The solution of (3.71)[17] is shown in Figure 3.41; we can observe that the function h guides the position of the curve inflexion point, while the pressure factor reduces the rate of increase of the species mass fraction.

---

[17] The solution of (3.71) is clearly the same of (3.69) and (3.70), if we consider only the first term in the brackets.

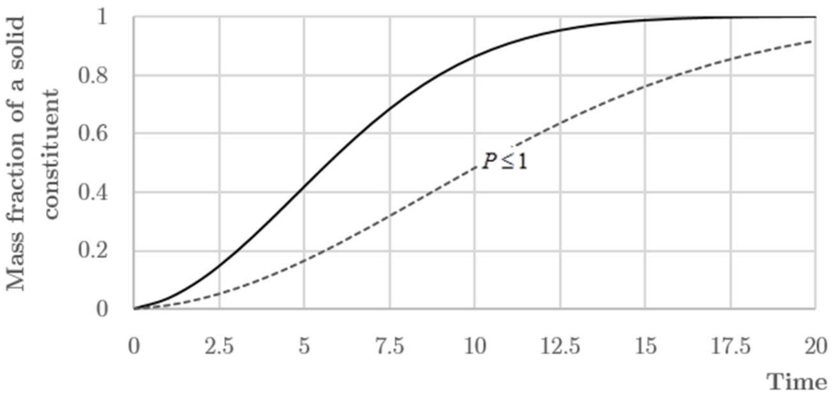

Figure 3.41 General trend of $\omega^{Cs}(t)$ when a linear load is considered over the whole time interval. Continuous line: unit pressure factor; dotted line: pressure factor lower-than-1.

As explained in the introduction, the mechanical stimulus is fundamental for the tissue differentiation process. Following Claes and Heigele results [85], [86], our model is enriched with a tissue differentiation guided by mechanical stimuli. If we consider the scaffold for spinal fusion, we assume that the tissue formation within the scaffold, after its implant between vertebrae, behaves almost like a vertebral (i.e. trabecular bone) fracture healing process. This phenomenon of bone formation is guided by the intramembranous ossification[18]. Taking into account the threshold stress in [86], we define a pressure factor that reduces the rate of growth of trabecular and cortical bone mass fractions. In our case, the limitation of hydrostatic pressure to ±0.15 MPa is more restrictive than the value of maximum strain of ±5% (Figure 3.39): the stiffness of the tissue becomes rather high in a short period of time (i.e. approximately 3000 MPa in one week), inducing with external loads significant stresses with small deformations. The pressure factor uses an analytical form, (3.68), that is able to firmly reduce the rate of increase of bone mass fraction (trabecular and cortical), when the threshold effective average pressure is reached (Figure 3.41).

---

[18] *Intramembranous ossification* is one of the two possible processes in the osteogenesis. Contrarily to *osteochondral ossification*, the intramembranous process develops precursor bone cells directly from the mesenchymal stem cell, without almost no intermediate cartilage formation.

During the process of bone formation in the scaffold, the mechanical properties of the solid phase vary with time, along with the growth of bone mass fractions. Each constituent contributes to the total stiffness of the solid skeleton behaving like a spring in parallel with the others (Figure 3.42). It is possible to define an average Young's modulus of the solid phase by considering the axial stiffness of each species [98, p. 186]:

$$k^i = \frac{E^i A^i}{l} \tag{3.72}$$

The total stiffness can be expressed as:

$$\frac{E^{avg} A^{tot}}{l} = \frac{E^{MSCs} A^{MSCs}}{l} + \frac{E^{Ts} A^{Ts}}{l} + \frac{E^{Cs} A^{Cs}}{l} \tag{3.73}$$

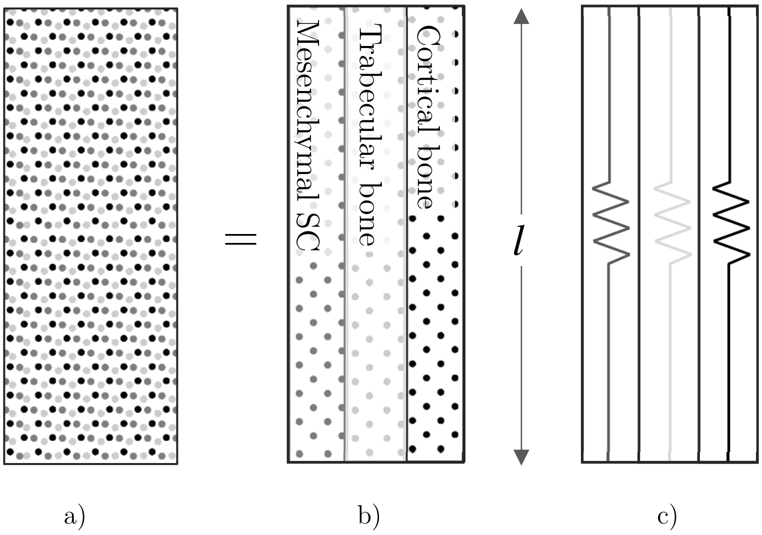

Figure 3.42 a) Schematic representation of the solid phase made of the three constituents. b), c) Each species in the solid skeleton behaves like a spring in parallel with the others.

Finally, the average Young's modulus can be obtained as:

$$E^{avg} = E^{MSCs} \frac{A^{MSCs}/l}{A^{tot}/l} + E^{Ts} \frac{A^{Ts}/l}{A^{tot}/l} + E^{Cs} \frac{A^{Cs}/l}{A^{tot}/l} \tag{3.74}$$

In equation (3.74) $\frac{A^{MSCs}/l}{A^{tot}/l}, \frac{A^{Ts}/l}{A^{tot}/l}, \frac{A^{Cs}/l}{A^{tot}/l}$ are the volume fractions of the constituents of the solid phase. In a multiphase porous medium, after passing to the macroscale, these microscale quantities must have a macroscale counterpart. As usually for the volume fractions in the solid phase, it is used the mass fraction of the species. Thanks to this assumption, we can rewrite equation (3.74) as:

$$E^{avg}\left(t\right) = E^{MSCs}\omega^{MSCs}\left(t\right) + E^{Ts}\omega^{Ts}\left(t\right) + E^{Cs}\omega^{Cs}\left(t\right) \tag{3.75}$$

Analogously to (3.75) and according to [88], the Poisson's coefficient is written as:

$$\nu^{avg}\left(t\right) = \nu^{MSCs}\omega^{MSCs}\left(t\right) + \nu^{Ts}\omega^{Ts}\left(t\right) + \nu^{Cs}\omega^{Cs}\left(t\right) \tag{3.76}$$

The evolution of the average permeability of the medium is defined using the same rationale:

$$\mathbf{k}^{avg}\left(t\right) = \mathbf{k}^{MSCs}\omega^{MSCs}\left(t\right) + \mathbf{k}^{Ts}\omega^{Ts}\left(t\right) + \mathbf{k}^{Cs}\omega^{Cs}\left(t\right) \tag{3.77}$$

The values of the material properties of the solid constituents are taken from [6], [16], [91], [99] and reported in Table 7.

Two additional equations complete our model: the mass conservation of the medium and the linear momentum balance. They can be derived with the same process described in §3.1.3.

The mass conservation of the entire medium in the spatial reference frame, by neglecting interphase exchange terms, can be expressed as:

$$\nabla \cdot \mathbf{v}^{s} + \nabla \cdot \left(\mathbf{q}\right) = 0 \tag{3.78}$$

The linear momentum balance equation in the spatial frame can be written as:

$$\nabla \cdot \left[\boldsymbol{\sigma}' - \mathbf{I}\,\alpha_B p^f\right] = 0 \tag{3.79}$$

The mechanical behavior of the solid skeleton is modelled as a Saint Venant-Kirchhoff nonlinear elastic material, which can be defined by *Lamé's constants*

λ, μ (see §3.1.3). λ, μ depend upon time through E, ν that are functions of the species mass fractions.

Table 7 Material properties for the scaffold evolving in time along with the tissue differentiation.

Component	E [MPa]	v	$\mathbf{k}$ [m^2][19]	ε
Mesenchymal stem cells[a]	2000[6], [99]	0.3[16]	1E-13[a]	0.52[99]
Trabecular bone[b]	10400[100]	0.3[16]	3.7E-18[16]	0.8[91]
Cortical bone	17000[16]	0.3[16]	1E-20[16]	0.04[91]

[a] Mesenchymal stem cell Young's modulus is taken equal to the empty scaffold's one. Due to the lack of experimental data, Poisson's coefficient is chosen equal to the bone, while permeability is selected of the same order of magnitude of the plantar tissue in the foot model (§3.1.7).

[b] The permeability and the Poisson's coefficient of the trabecular bone is set equal to the one of the mature bone, because no experimental values were found.

---

[19] The hydraulic conductivity $\mathbf{K}$ used in [16] is measured in m^4/Ns and is related to the permeability $\mathbf{k}$ with the relation: $\mathbf{K} = \frac{\mathbf{k}}{\mu}$, where μ is the dynamic viscosity, with $\mu = 0.001\ N \cdot s\ /\ m^2$.

3.2.2.2. Numerical results

To investigate the effect of the loading on tissue differentiation, three different analyses are developed. In the first one, no external loads are considered, to assess the capacity of the model to match *in vivo* results. In the second one, a pressure of 0.64 MPa[20] is linearly increased over a time of 200 minutes, starting at 10000 minutes (about 1 week) and then is kept almost[21] constant until the end of the simulation (Figure 3.46). In the third case the scaffold is loaded at four weeks (40000 min), to study the effects of the delayed mechanical stimulus on the phenomenon.

According to the surgery procedure, as a first approximation a Dirichlet condition on the interstitial fluid pressure is used $(p_f = 0)$ at the top and the bottom of the scaffold. The axisymmetric model with boundary conditions and loads is presented in Figure 3.43.

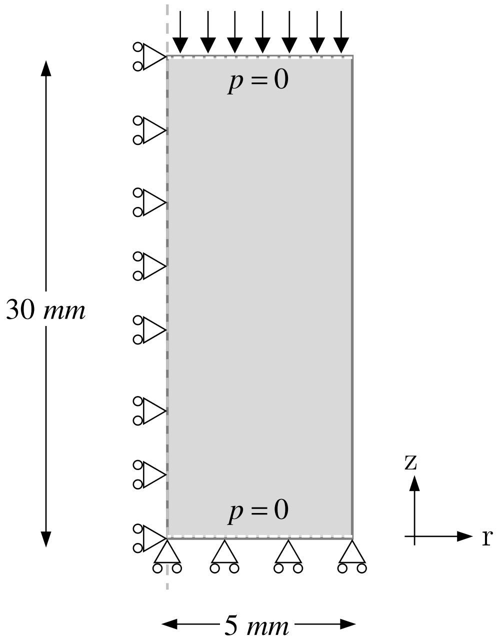

Figure 3.43 Schematization of the geometry, boundary conditions and loads on the scaffold for spinal fusion model.

---

[20] Since the scaffold is implanted in a rabbit spine, in our analyses we considered a load of 50 N, which corresponds to the average weight of the animal $\left(0.64\ MPa\ =\ 50\ N\ /\ (5^2\pi)\ mm^2\right)$; New Zealand white rabbits: http://www.criver.com/files/pdfs/rms/nzw/rm_rm_d_nzw_rabbit.aspx

[21] Actually, a further increase of the load of 0.005 is used to overcome to convergence issues.

Considering the first (reference) case without applied loads (Figure 3.44), at the initial time the mesenchymal stem cell mass fraction is 100%. From that moment on, in almost 3.2 weeks (about 32000 min), the cortical bone grows from 0% to 100%, thus reducing the mass fraction of the MSC. When the trabecular bone reaches its peak (about 32000 min), the cortical species starts growing, with a limited increase with time.

The development of the volume fraction of trabecular and cortical bone are measured experimentally in [6]. In analogy to what is stated in §3.2.2.1, by scaling the volume fractions with the maximum value of the range, it is possible to compare experimental results with the species mass fraction development curves of our model.

In Figure 3.44 it can be observed that the model gives results that are in good agreement with experimental ones [6], for both trabecular and cortical bone.

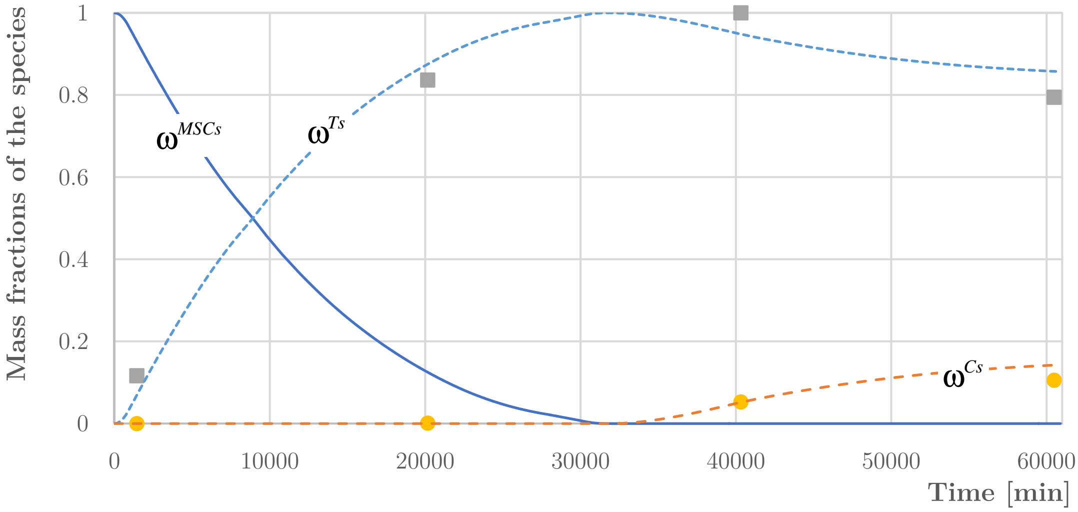

Figure 3.44 Evolution with time of the mass fraction of the species for the numerical simulation without loads applied. Numerical results for MSC species, ω^{MSCs}, are represented with continuous line, while cortical and trabecular species mass fractions are shown with dotted lines (short dash for cortical, ω^{Ts}, long dash for trabecular, ω^{Cs}).Experimental results are displayed with square dots (trabecular bone) and circular dots (cortical bone).

For the reference case, the evolution of the Young's modulus and the permeability, following (3.75) and (3.77), is shown in Figure 3.45.

Let us now consider the second case, with the load applied at about 10000 min. The effect of the stresses on the growth of the tissue is clear: the application of the load on the scaffold leads to an effective average pressure (about 0.22 MPa) within the domain that is higher (+46%) than the limit value for intramembranous ossification process (Figure 3.39). The pressure factor introduced in (3.68) limits the velocity of transformation of mesenchymal stem cells into trabecular bone.

By comparing Figure 3.44 and Figure 3.47, it is evident that the trabecular bone mass fraction after 6 weeks does not reach the value of 100%, but grows only to 65%. As a consequence, there is no cortical bone formation during the time period observed.

If we consider the evolution of the Young's modulus, evidently it follows the trend of the trabecular bone mass fraction, remaining almost constant after the application of the load (when trabecular bone mass fraction increases very slowly), and becoming stiffer more rapidly after three weeks. Young's modulus and hydrostatic effective pressure are displayed in Figure 3.48.

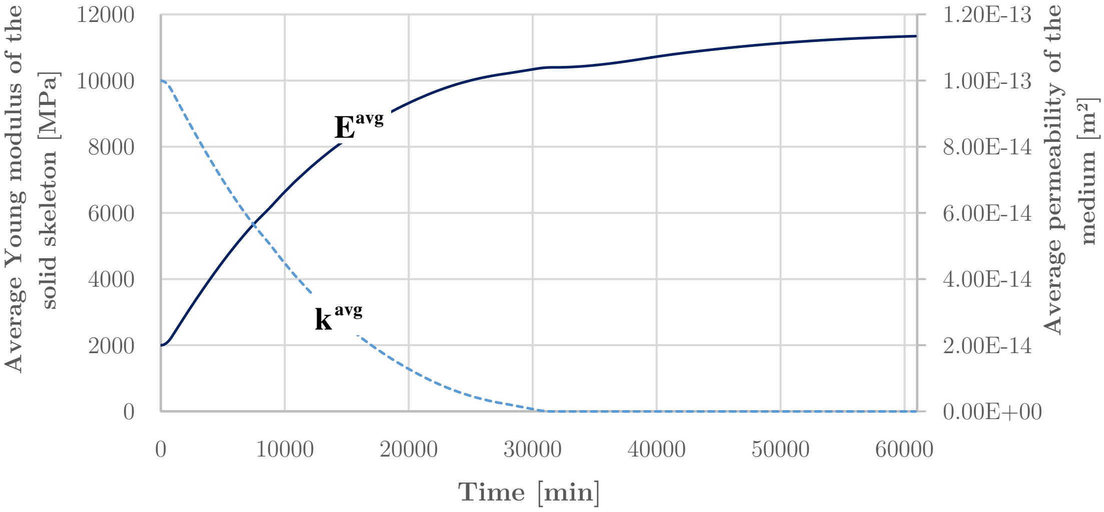

Figure 3.45 Trend in time of the average Young's modulus of the solid skeleton (continuous line) and of the average permeability of the medium (dotted line) for the numerical simulation without loads applied.

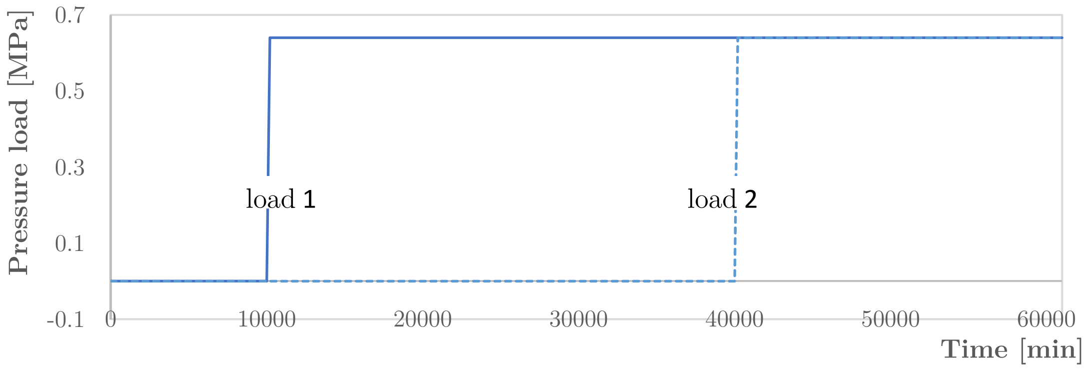

Figure 3.46 Loading configurations: *load 1* is applied at t=10000 min, whereas *load 2* starts increasing at t=40000 min.

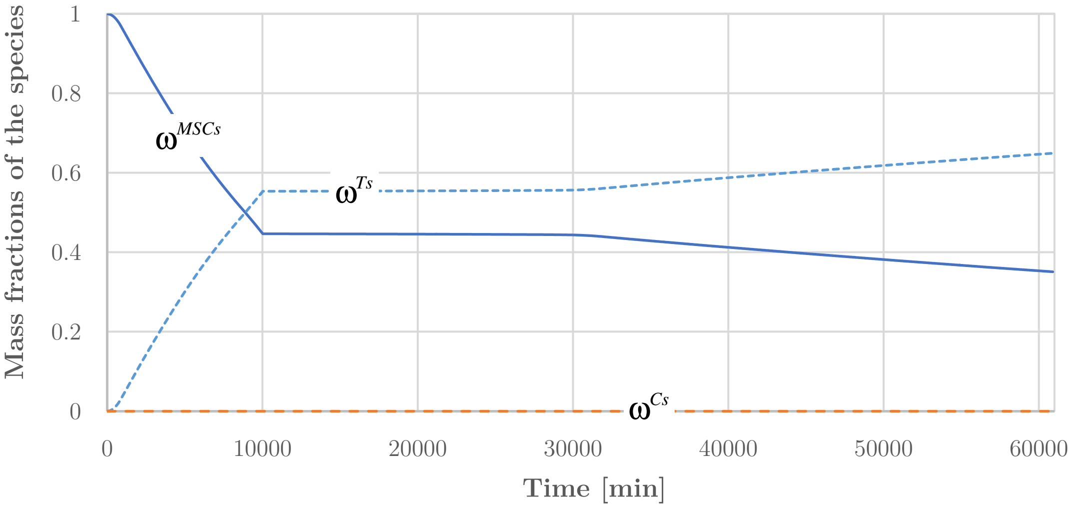

Figure 3.47 Evolution with time of the mass fraction of the species for the numerical simulation with load applied after 10000 min. Numerical results for MSC species, ω^{MSCs}, are represented with continuous line, while cortical and trabecular species mass fractions are shown with dotted lines (points for cortical, ω^{Ts}, dashes for trabecular, ω^{Cs}).

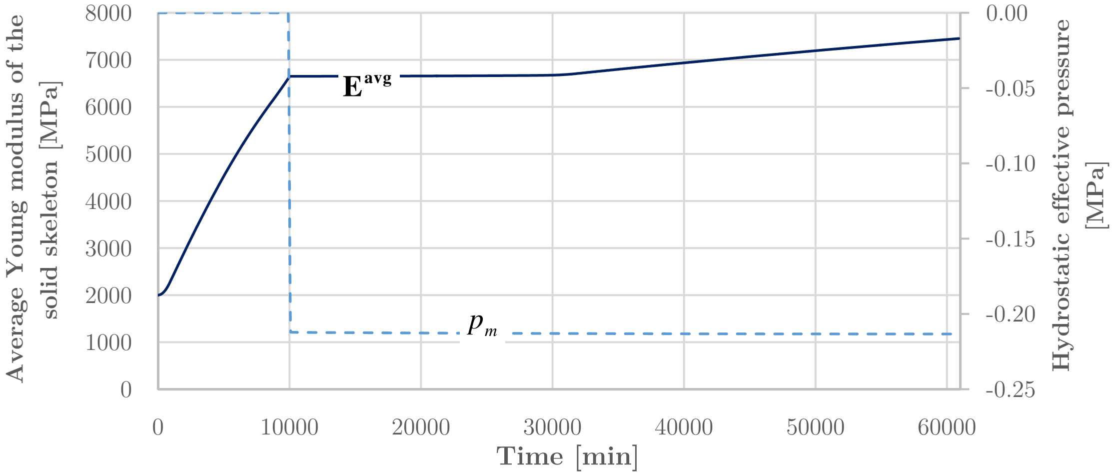

Figure 3.48 Average Young's modulus (continuous line) and hydrostatic effective pressure (dotted line), for the numerical simulation with load applied at 10000 min.

In the final case, the load application is delayed to 32000 min. Contrarily to the second configuration, this load affects only the cortical bone formation process, since it is applied after the complete transformation of the whole MSC solid constituent into trabecular one. The pressure factor strongly reduces the increasing rate of the cortical bone mass fraction, determining an almost constant value of the mass fraction from the end of the load ramp to the conclusion of the simulation. As a consequence the value of the average Young's modulus grows slightly, as well as the values of the trabecular bone mass fraction, due to the fact that its cortical counterpart increases very slowly.

Due to the time scale of the problem, the velocity of loading and the boundary conditions $(p = 0)$, the value of the interstitial fluid pressure is almost always negligible. The load is applied very slowly, allowing the fluid transferring the stresses to the solid skeleton almost instantaneously and rapidly exiting from the free flow boundary.

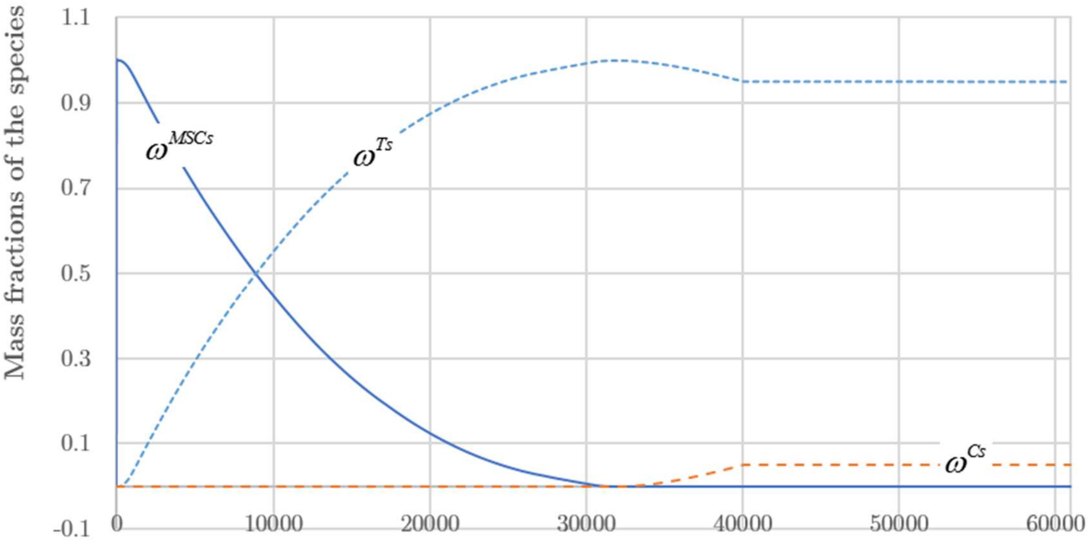

Figure 3.49 Evolution of the mass fraction of the species for the numerical simulation with load applied after 40000 min. With continuous line numerical results for MSC species, ω^{MSCs}, is represented, while with dotted lines cortical and trabecular species mass fractions are shown (short dash for cortical, ω^{Ts}, long dash for trabecular, ω^{Cs}).

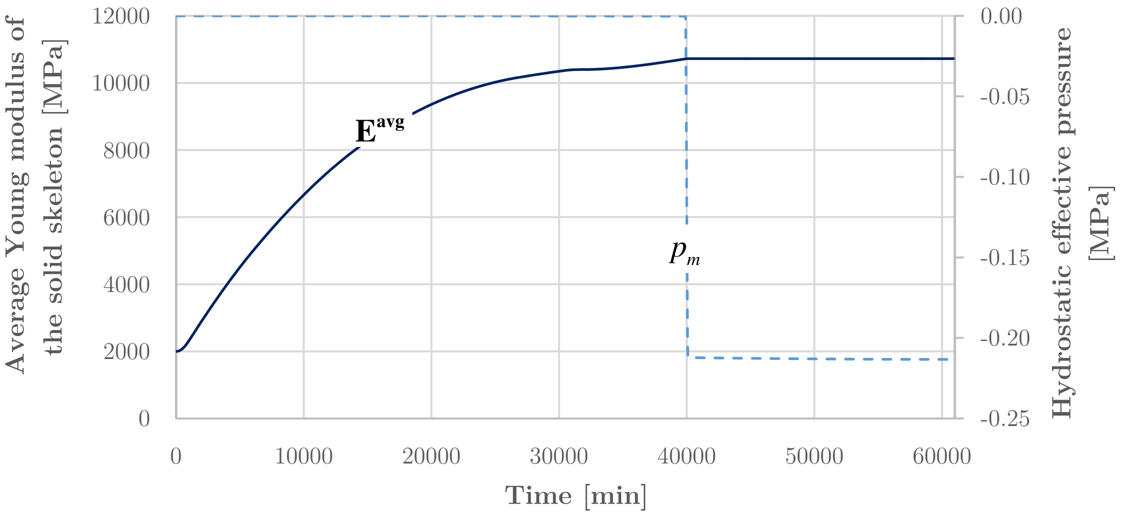

Figure 3.50 Comparison between average Young's modulus (continuous line) and hydrostatic effective pressure (dotted line), for the numerical simulation with load applied at 4 weeks.

Though this model is a preliminary study in the field of scaffold for spinal fusion, it is clearly promising. It is able to efficiently fit the evolution of the experimental data during time by simulating the mass fraction of trabecular and cortical bone within a scaffold implanted in rabbit. The mechanical stimuli guide the bone formation, following the results introduced by Claes and Heigele in [86]. As a consequence, the level of hydrostatic effective pressure is capable to limit the velocity of tissue differentiation during time. This model can be a useful tool in the definition of scaffold dimensions, to promote a bone augmentation process depending upon the load supported by the scaffold during the post-operative period in the spine fusion surgery.

The results found *in silico* could be validated in the future by experimental tests on *in vivo* implanted scaffolds. By estimating the load borne by one scaffold (i.e. a portion of the total weight), it is possible to assess the capability of the cells to differentiate into tissues. This validation process can be achieved by a comparison between the volume fractions of the bone constituents in case of impeded mobility and in case of load bearing started at a specific moment after the implant.

As a future perspective, the mechanical stimuli for the tissue formation can be also enriched by fluid flow velocity [91], as well as by biological stimuli such as the nutrient concentration in the fluid phase as in [10], [13], [101].

3.2.3. Scaffold for the repair of osteochondral defect

Articular cartilage is a fundamental structure in the joints that allows the transmission of loads, by ensuring a low friction and low shear stiffness environment. The main constituent of a body joint is the cartilage (Figure 3.51). This tissue gives the articulation a gliding surface property [102], which allows relative motions of the bones, thanks to its high shear stress and high traction resistances [103]. It is composed by four parts: the superficial, the transitional, the middle and the calcified cartilage zones. Each component, with its specific structure due to different cell arrangement and biochemical composition, contributes to the overall behavior of the joint. Nevertheless, the superficial layer plays the major role in the behavior described. Due to its high water content, it acts as a low-friction soft bearing, reducing stress peaks on the subchondral bone by working as a shock absorber [102]. The mechanical behavior of the cartilage is very different from the bony layer: in the calcified cartilage zone a *tidemark* tissue can be identified. In this part of the joint it takes place a gradual transition from the resilient cartilaginous part [102] to the stiffer subchondral bone, thus reducing the effects of the bone-cartilage discontinuity.

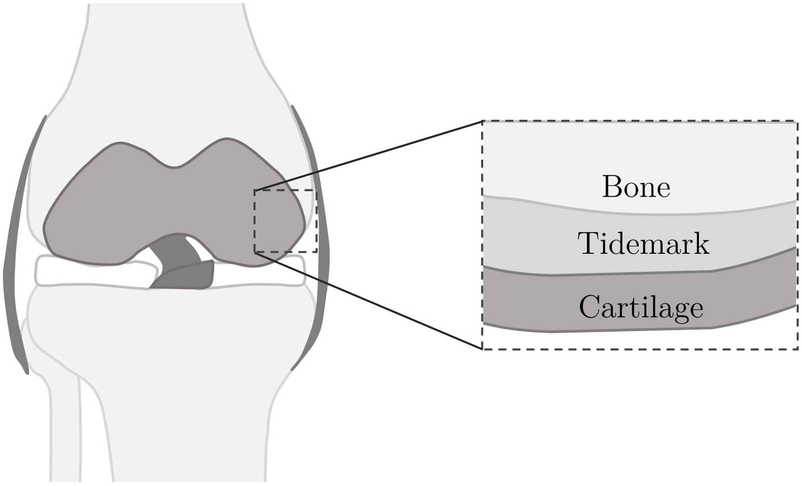

Figure 3.51 Schematization of a knee joint. In detail, the layers of the articulation.

According to [104]–[106], about 65% of the subjects that undergo knee arthroscopies suffer from articular defects. Two different types of defects can be defined, whether they involve the cartilage layer (*chondral defect*) or also the subchondral bone constituent (*osteochondral defect*) of the joint. Due to its structure, articular cartilage is mainly made of water (from 65% to 80%) and it has neither vascularization nor nerve supply [107]. As a consequence, in case of defect triggering at an early stage it is difficult to feel a protective pain which prevents from loading the joint, and later, to promote an autonomous repair process in the tissue. The capacity of repair also depends on different factors: such as the depth of defect, the age of the subject and the type of the trauma [102]. Defects involving the entire chondral layer cannot be repaired; on the contrary, if only the subchondral bone is scratched, the mesenchymal stem cells from bone marrow can reach the defect, allowing a repair. However, from a biological and mechanical point of view, the resulting tissue is different from the initial one, determining a repaired layer with a reduced load-bearing capacity.

Chondral injury leads to severe pain and disability, due to swelling, locking and catching of the joint. In addition, if defects are not treated, they can cause a premature arthritis, which can require the replacement of the articular surface. However, this solution is ideal for subjects over 60 years, with a sedentary life style [102], but it is not suitable for young people. Different approaches are developed [108]–[111], but one of the most promising solutions in the engineered tissue field is the use of heterogeneous scaffolds [99]. They can be made with different layers, to promote an efficient integration within the joints, by regenerating both its cartilage and bone constituents.

In this context, *Houston team* developed a biomimetic osteochondral composite scaffold [99]. Its structure and chemical composition are studied to resemble the extracellular matrix of cartilage and bone. As a results, a three layer scaffold is obtained: a first layer, which mimics the subchondral bone, is made of hydroxyapatite (HA)[22] and type I collagen (Coll) in a mass proportion respectively of 70/30. An intermediate layer, resembling the tidemark, is very similar to the previous one, but

---

[22] The HA component brings the mineral component, which is fundamental in the bone formation process.

it has a reduced mineral content: it is made of HA/Coll in a mass proportion of 40/60. A third layer has to trigger cartilage formation, so it is composed of hyaluronic acid and type I collagen.

Analogously to the spinal fusion (§3.2.2), a tissue formation process takes places in the osteochondral scaffold, with biological and mechanical properties that vary with time (Figure 3.52).

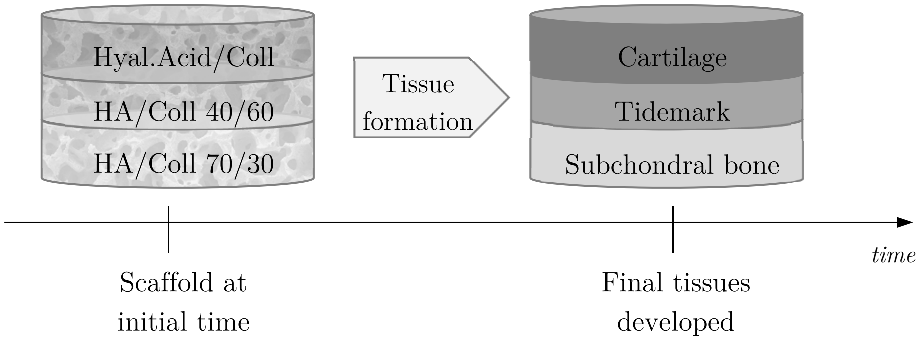

Figure 3.52 Schematization of the scaffold property development as a function of time.

Due to the complexity of the problem, as a starting point the final configuration of the scaffold is considered, i.e. when the final tissues are fully developed.

3.2.3.1. The mathematical model

The scaffold for osteochondral defect is modelled as a composite porous medium: the solid skeleton of each layer, which is made of the tissue cells (i.e. cartilage, tidemark and bone) and their extracellular matrix, is fully saturated by the interstitial fluid. No species transformation within solid and no interphase mass exchange are considered, because of the scaffold configuration chosen (Figure 3.52).

The mass conservation for the entire medium can be written in analogy to (3.18) as:

$$\nabla \cdot \mathbf{v}^s + \nabla \cdot \left(-\frac{\mathbf{k}^t}{\mu^f} \nabla p^f \right) = 0 \tag{3.80}$$

where $\mathbf{k}^t$ is the specific permeability of the tissue filling the layer.

Following (3.27), the linear momentum balance for the whole composite is:

$$\nabla \cdot \left[\boldsymbol{\sigma}' - \mathbf{I}\, \alpha_B p^f \right] = 0 \tag{3.81}$$

The effective Cauchy stress tensor is obtained by the derivation of the elastic strain energy density as in §3.1.3. The solid skeleton of each material is modelled as a Neo-Hookean hyperelastic material, due to the high strain regime involving the cartilage layer. The strain energy density for the compressible version of the Neo-Hookean material can be written following [112]:

$$w = \frac{1}{2}\mu\left(I_1 - 3\right) - \mu \ln\left(J_{el}\right) + \frac{1}{2}\lambda\left[\ln\left(J_{el}\right)\right]^2 \tag{3.82}$$

where λ, μ are Lamé coefficients, J_{el} is the elastic volume ration and I_1 is the first invariant of the elastic right Cauchy-Green deformation tensor $\left(\mathbf{C}\right)$.

Additional equations must be introduced at the interfaces between different layers. Thus, in the solid skeleton two relations are used for displacement continuity and stresses condition [55, p. 153] respectively:

$$\left[\left| \mathbf{u} \right|\right] = \mathbf{0} \tag{3.83}$$

$$\left[\left| \boldsymbol{\sigma} \cdot \mathbf{n}^t \right|\right] = \mathbf{0} \tag{3.84}$$

where $\left[\left| * \right|\right]$ represents the jump at the interface for the argument and $\mathbf{n}^t$ is the unit normal to the interface.

By considering the fluid phase, a continuity condition on the interstitial fluid pressure and another one on fluxes are written respectively as:

$$\left[\left| p^f \right|\right] = 0 \tag{3.85}$$

$$\left[\left| \left(\mathbf{k} \nabla p^f\right) \cdot \mathbf{n}^t \right|\right] = 0 \tag{3.86}$$

3.2.3.2. Numerical Results

According to [99], the scaffold is a cylinder of 10 mm radius, its height is 6 mm, divided into bone (2.5 mm), intermediate (1.5 mm) and cartilaginous (2.0 mm) layers. The properties of the tissues are summarized in Table 8, with the properties of tidemark chosen to be intermediate between bone and cartilage ones, due to its transition function within the tissue. We suppose to implant the scaffold within a knee joint, in an articulation defect repairing perspective (Figure 3.53). By taking advantage of the experimental loads coming from the diabetic foot application (§3.1.6), we decided to consider two different types of load: a vertical force (i.e. the one perpendicular to the ground, measured by means of the force plates), and a shear force (corresponding to the anterior-posterior shear force component on the ground plane). These forces are applied to the bottom surfaces of the scaffold bone layer and we further assume that only 1/5 of their value is transferred to the scaffold.

Table 8 Material properties for each tissue within the scaffold.

Layer	E [MPa]	v	$\mathbf{k}$ [m^2]
Cartilage[91]	10	0.167	5E-18
Tidemark	8505	0.235	2.51E-18
Bone[91]	16500[a]	0.3	1E-20

[a] A lower value than the one in [91] is used, due to the fact that the layer is made of subchondral bone.

Let us consider a first set of three analyses in which the maximum vertical load (about 148 N[23], Figure 3.10a) is linearly ramped over time from 0 to t_1; it is maintained constant until t_2 and finally linearly reduced to zero between t_2 and t_3 (Figure 3.54). The interstitial fluid can flow only through the lateral surface of the scaffold and it is restrained at the top face as represented in Figure 3.55.

---

[23] $148\ N = 0.2 \cdot 740\ N$

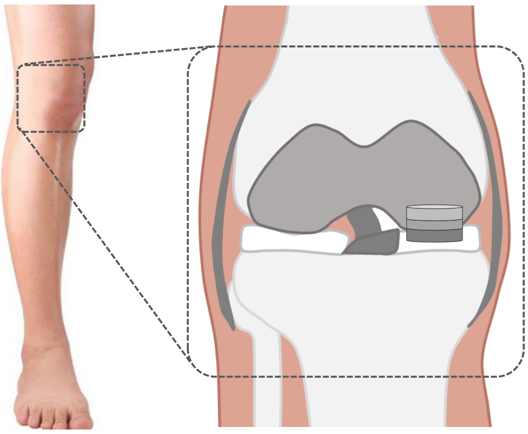

Figure 3.53 Schematization of an osteochondral scaffold in a knee joint for articular repair.

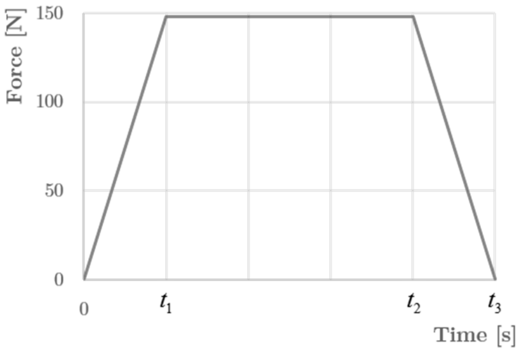

Ramp #	1	2	3
t_1 [s]	1	2.5	5
t_2 [s]	5	5	5
t_3 [s]	1	2.5	5

Figure 3.54 *Left:* Vertical load as a function of time. *Right:* Values of loading time for the three analyses developed.

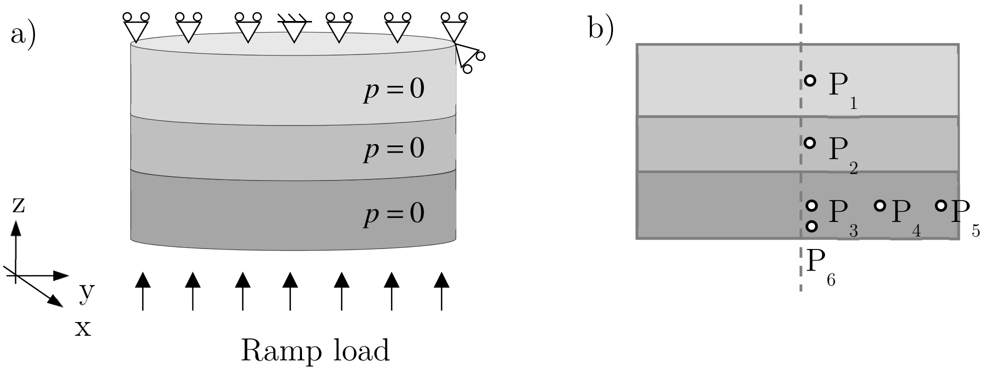

Figure 3.55 a) Boundary conditions applied to the geometry of the scaffold. b) Vertical section of the cylinder. Interstitial fluid pressure, total and effective stresses are evaluated in the six points highlighted.

Each condition is defined to study the effect of the loading velocity on the fluid-structure interaction within the tissues. Let us compare the cases number 1, 2 and 3 (Figure 3.56, Figure 3.57, Figure 3.58): the load is applied very rapidly (1 s) in the first configuration, while it increases more slowly in the second and third ones, (2.5s and 5 s respectively).

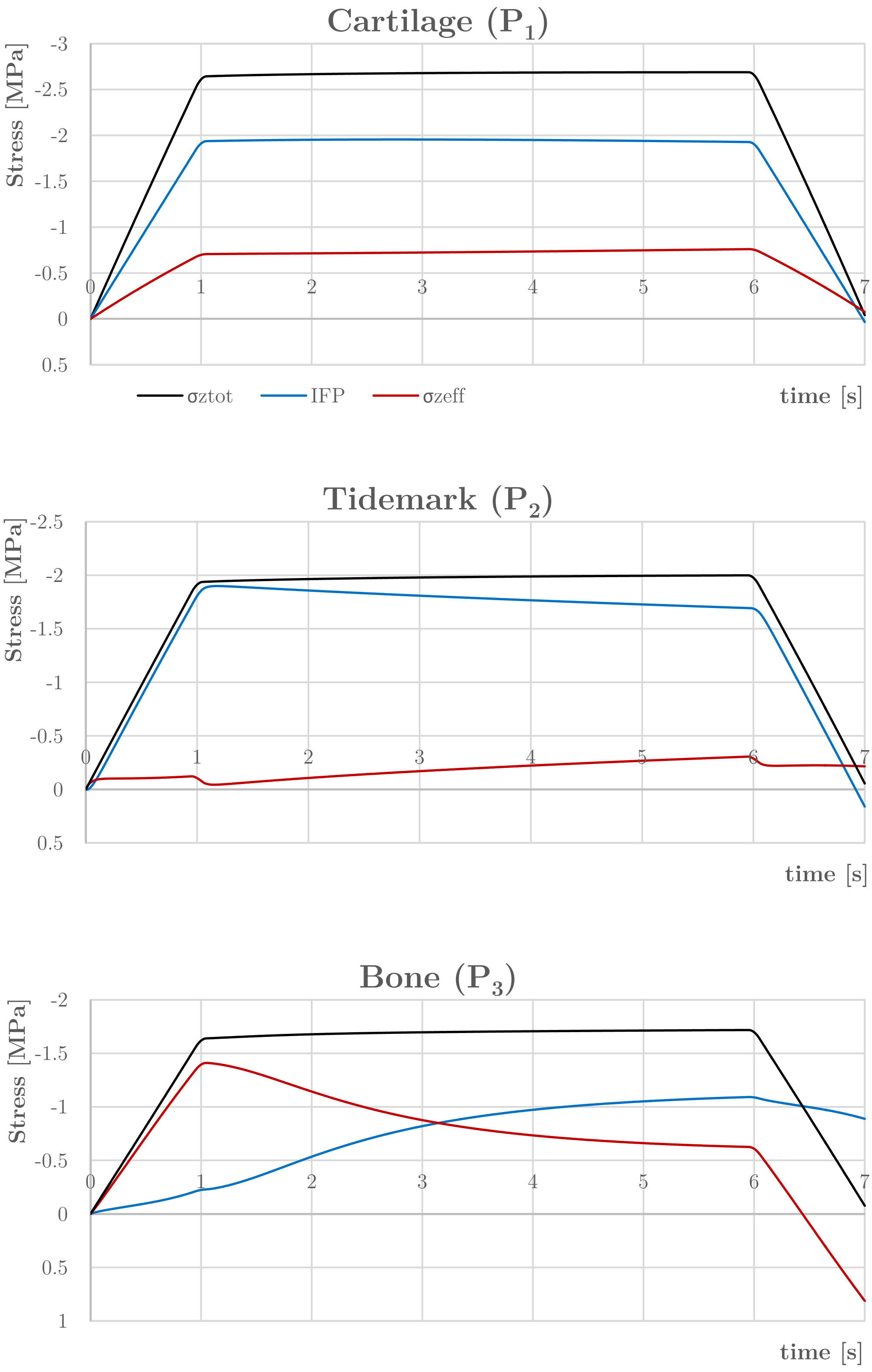

Figure 3.56 Interstitial fluid pressure (light blue), total (black) and effective (red) vertical stress in different points within the scaffold for the ramp load #1. (IFP is positive for traction)

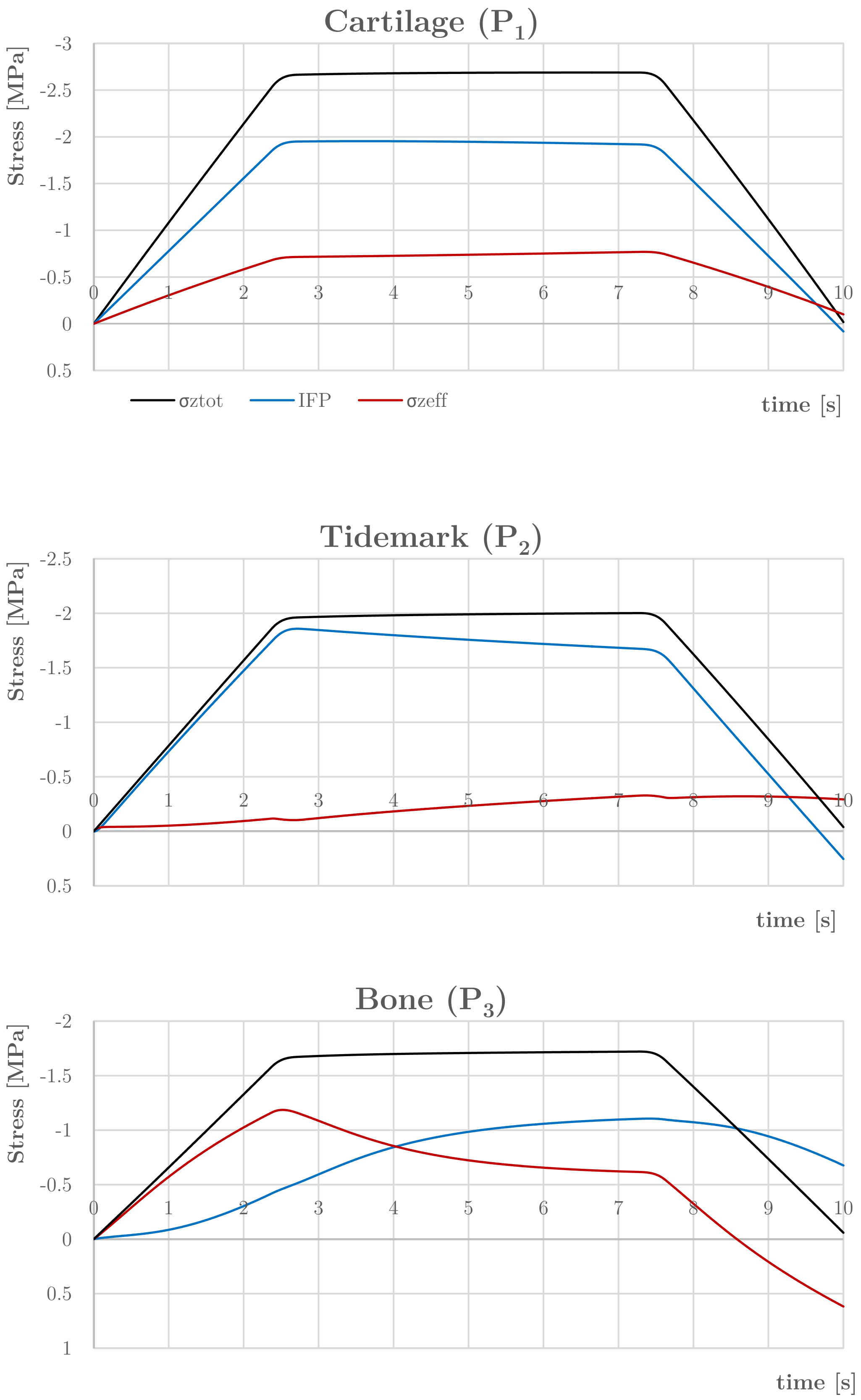

Figure 3.57 Interstitial fluid pressure (light blue), total (black) and effective (red) vertical stress in different points within the scaffold for the ramp load #2. (IFP is positive for traction)

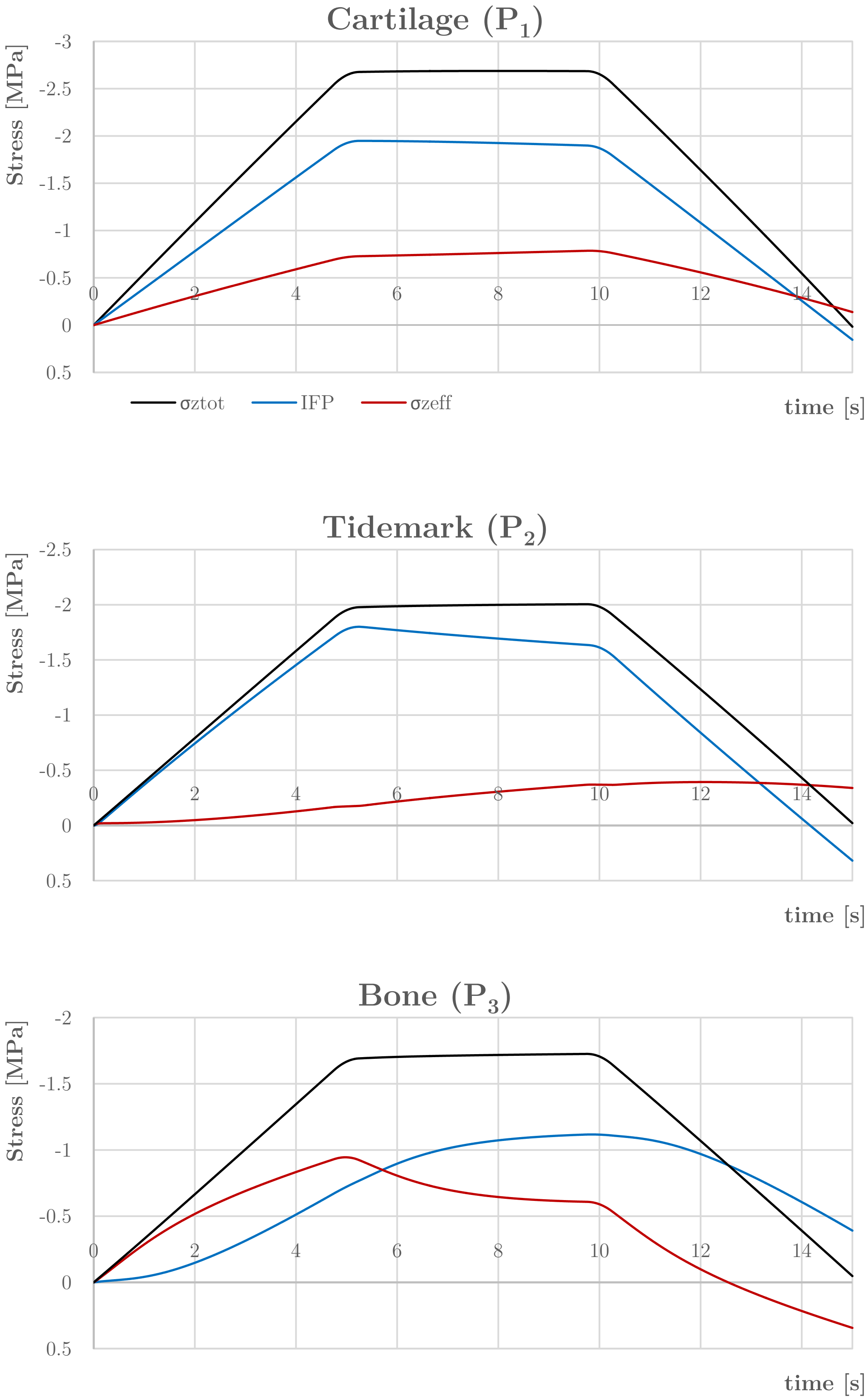

Figure 3.58 Interstitial fluid pressure (light blue), total (black) and effective (red) vertical stress in different points within the scaffold for the ramp load #3. (IFP is positive for traction)

The cartilage layer (point P₁) is almost insensitive to the velocity of loading. When the load is constant, the solid-fluid interaction leads to a low reduction of the interstitial fluid pressure, and a limited increase of the vertical effective stress. A more pronounced trend can be observed in the tidemark layer (point P₂), where the effective stress increases more slowly with the lowest loading velocity (#3). In the bone layer (point P₃), we can see that IFP and the effective stress have an opposite trend with respect to the tidemark layer. This behavior is due to the interaction of different properties: the stiffness and the permeability of the solid skeleton, the velocity of the load and the interaction with the other tissues. The bone layer is very stiff and has a low permeability: therefore, in the inner zone of the scaffold it is very difficult for the fluid to exit through the lateral surface. In addition, the fluid from the tidemark layer flows into the bone one, causing an excess of fluid pressure in the middle of the bone (Figure 3.60). Thus, the stresses in the solid skeleton are decreased, instead of increased for the consolidation during the constant load phase.

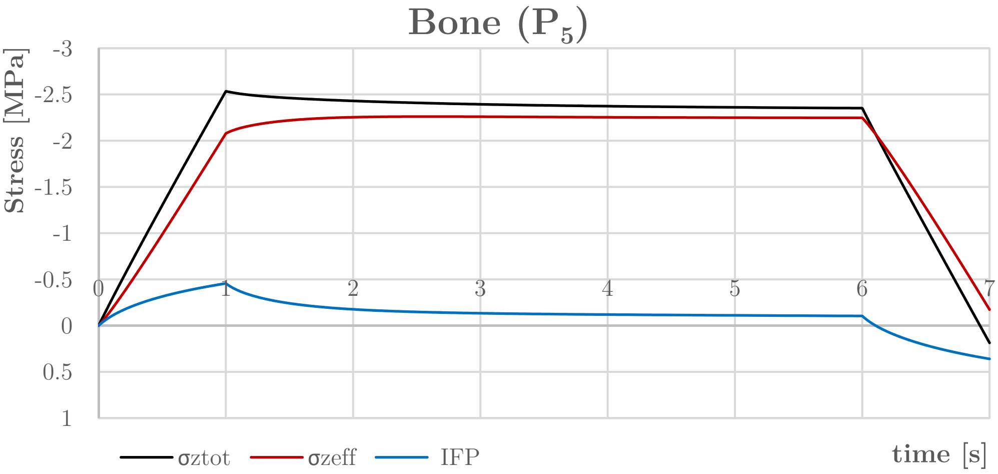

Figure 3.59 Interstitial fluid pressure (light blue), total (black) and effective (red) vertical stress in point P_5 for the ramp load #1. (IFP positive for tractions)

On the contrary, by considering the trend of the stresses and IFP in point P_5 (near the free flow surface) we can see the effects of the consolidation (Figure 3.59), because of the higher facility for the fluid to flow outside the scaffold. A further confirmation is given by Figure 3.61, where a fourth analysis, with longer periods ($t_1 = 200\,s$ and

$t_2 = 1000\,s$), is performed. In this case, the effects of fluid flow from the tidemark layer to the bone one become almost negligible, allowing the consolidation phenomenon to proceed.

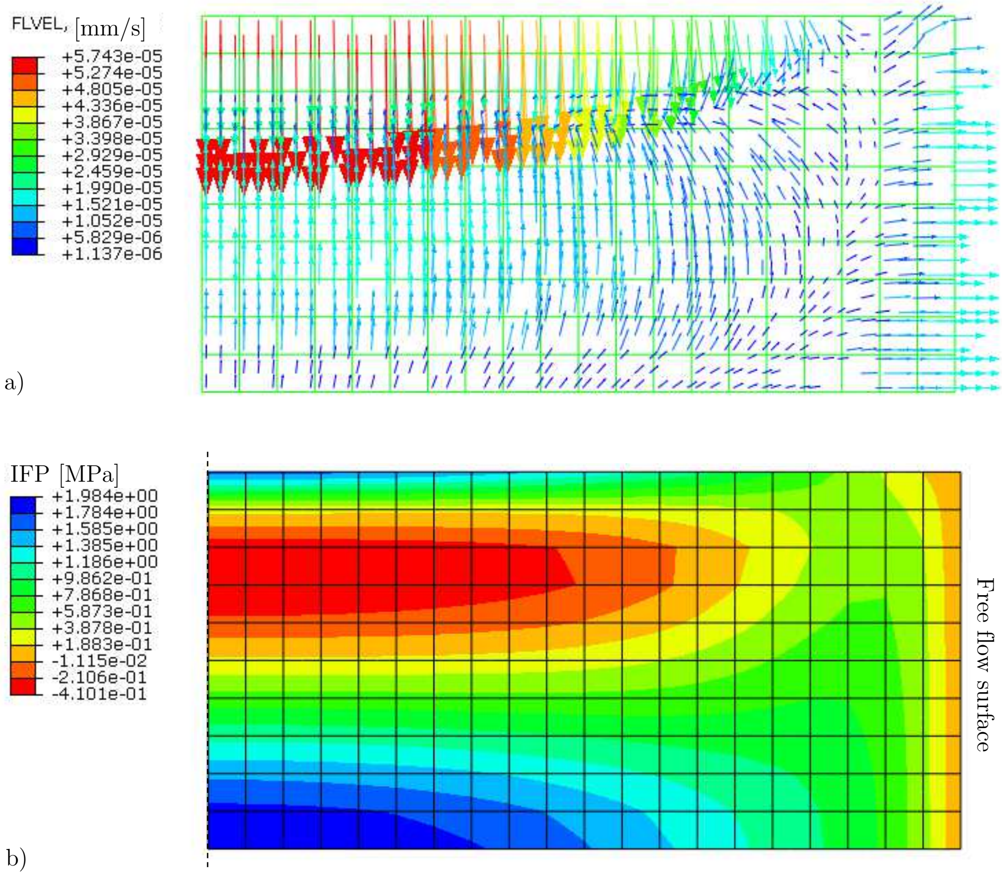

Figure 3.60 a) Vector plot of fluid velocity (FLVEL). b) Contour plot of IFP (Positive for compression) at t=1 s for the load case #1 within the bone layer (plane *yz*).

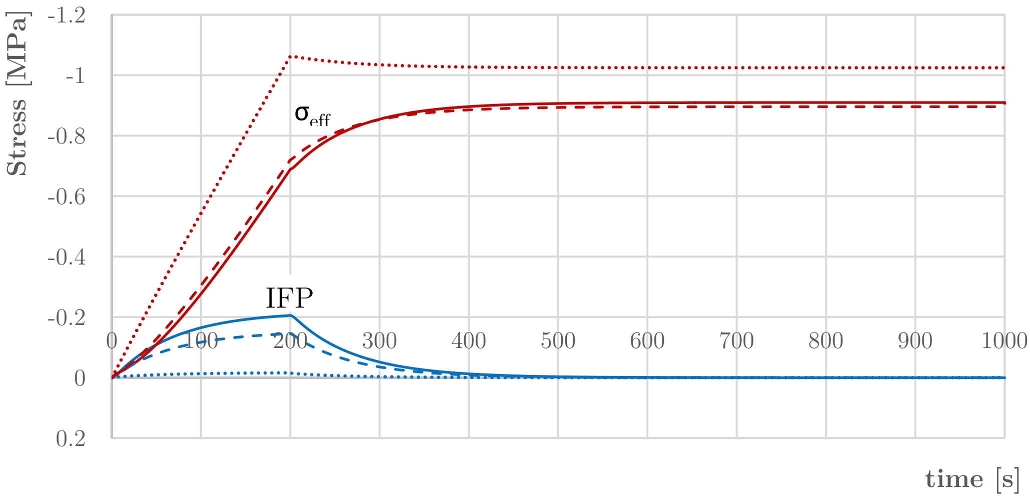

Figure 3.61 Comparison between effective vertical stress and IFP for 1000 s loading time, evaluated in P3 (continuous line, near the cylinder axis), P_5 (dashed line), P_4 (dotted line, near the lateral surface of the cylinder).

Finally, two real cases are considered by exploiting subject specific loads acquired experimentally. The application of the vertical force and the shear anterior-posterior force in four gait cycles are taken into account.

By considering the vertical force shown in Figure 3.12, numerical results show stress trends that are similar to the one obtained with ramp load analyses (Figure 3.62). By observing Figure 3.63, peaks in the interstitial fluid can be found at the layer interfaces, near the axis of the scaffold. In particular, the pressure gradient between the center of the intermediate and the lower layers induces a vertical fluid flow from the tidemark to the bone layer. In P_3, the fluid-structure interaction is affected by the mutual influence of different layers, giving increasing peak values of IFP, while they are decreasing for the vertical stress. On the contrary, at the bottom of the bone layer (P_6), the fluid is able to flow more freely, determining a usual transfer of stresses from the interstitial fluid to the solid skeleton, as the number of load cycles increases.

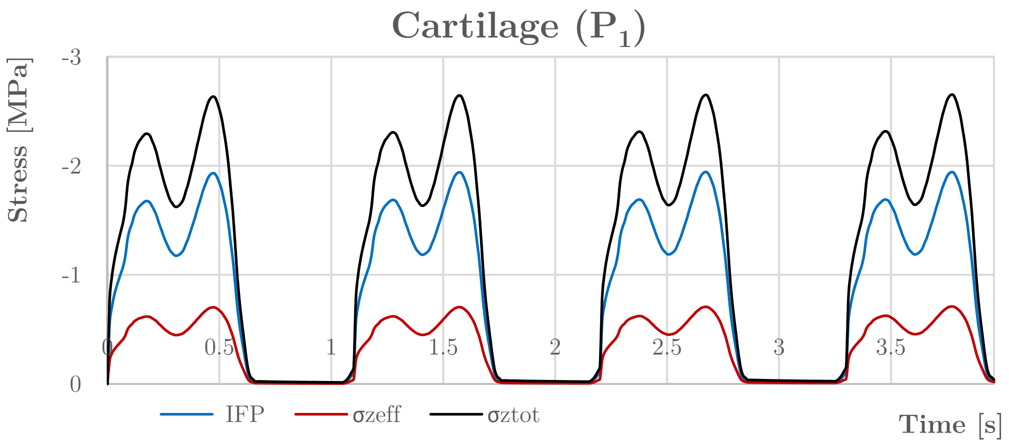

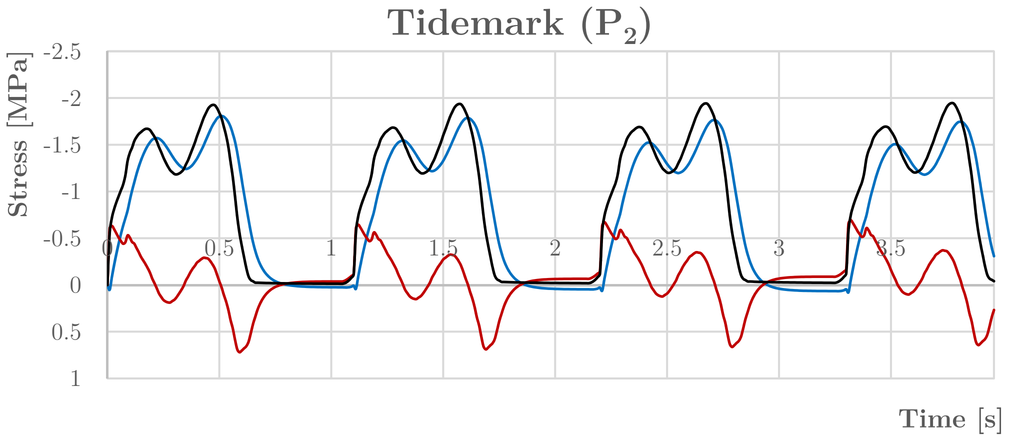

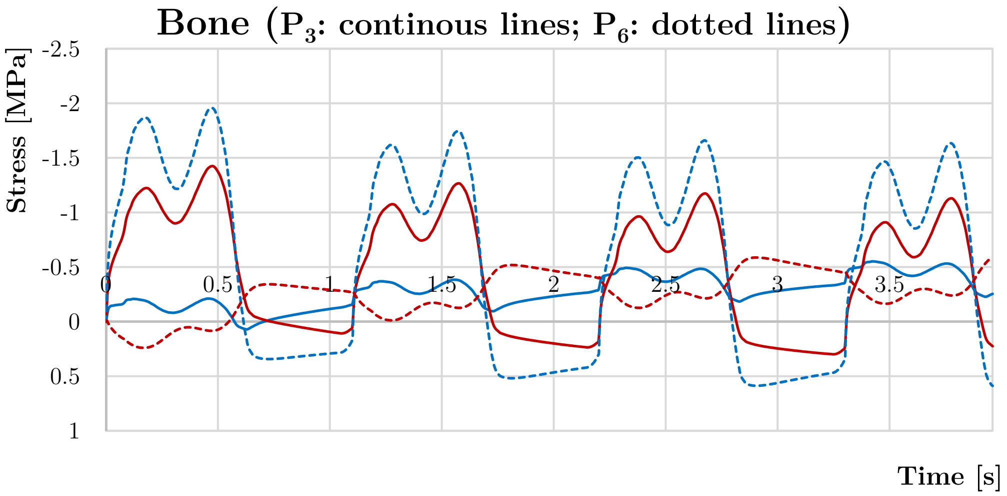

Figure 3.62 Trend of the interstitial fluid pressure (light blue), total (black) and effective (red) vertical stress at different points within the scaffold for the vertical load in four gait cycles. (IFP is positive for traction)

Starting from the preliminary results of these analyses with vertical loads, we obtained valuable information for a possible improvement of the scaffold structure. Due to the trends of vertical effective stress and IFP in the bone layer, this part of the scaffold can be enhanced. To reduce the interaction effects between adjacent layers, the biochemical structure of the scaffold bone layer could be rethought. The main target is to induce within the layer zones of bone tissue showing different properties (i.e. stiffness and permeability), in a perspective of determining a more homogenous stress value map within the bone constituent. A good starting point solution could be obtained by introducing an intermediate central bone layer with lower stiffness and higher permeability, resembling the trabecular bone, reducing pressure gradient within the core of the bone layer.

As a future perspective, following the same strategy used in §3.2.2, the tissue development within scaffold, as a function of time, can be implemented. The evolution of different species within the solid skeleton, mimicking the tissue formation process, can be introduced depending on the application of external biomechanical stimuli (e.g. stress, strain, cell nutrient, etc.).

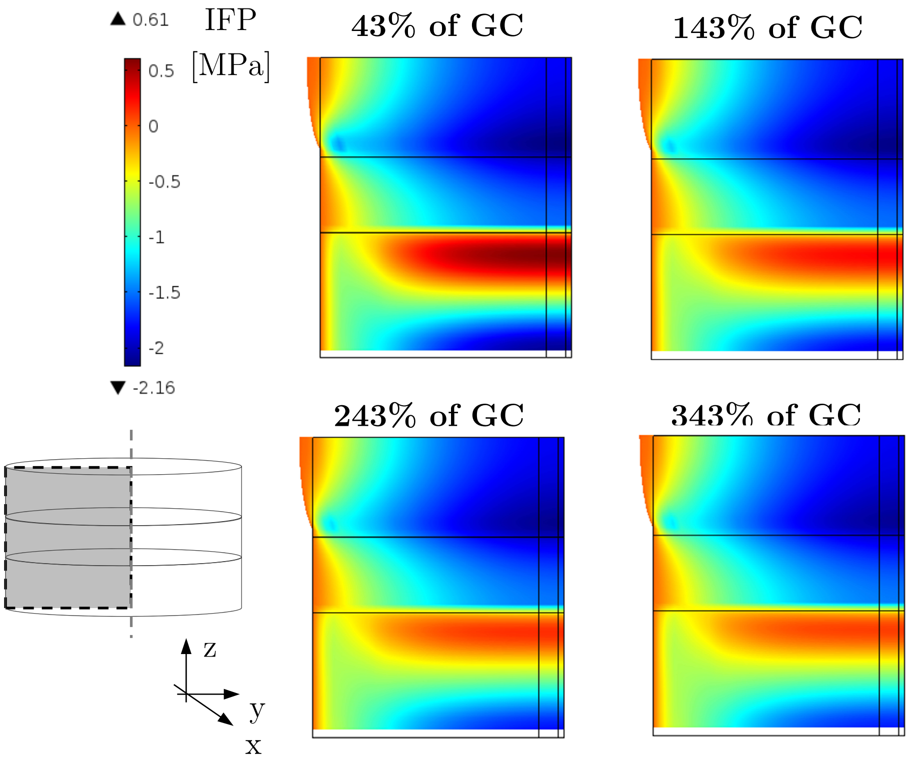

Figure 3.63 Contour plot of the IFP at the four peaks in vertical load during four gait cycles (GC) in a xy plane as in detail (*bottom left*). (IFP is positive for traction)

Let us finally consider the application of the anterior-posterior foot shear forces to the scaffold. In Figure 3.64 the boundary conditions (a) and the load applied (b) are shown. The loading configuration is a limit case, due to the fact that in reality both shear and vertical forces are applied at the same time. By analyzing the contour plot of the shear stress component τ_{zy} in Figure 3.66, we can observe that the highest values are near the center of the cylinder, whereas they are minimum at the extremities of the diameter, with a parabolic trend, with maximum values at the center of the scaffold (Figure 3.65).

Bone and tidemark layers are highly stiffer than the cartilage one, as seen Table 8: as a consequence, due to shear stress they are subjected primarily to an almost rigid body motion with small strains, whereas higher deformations can be found in the cartilage.

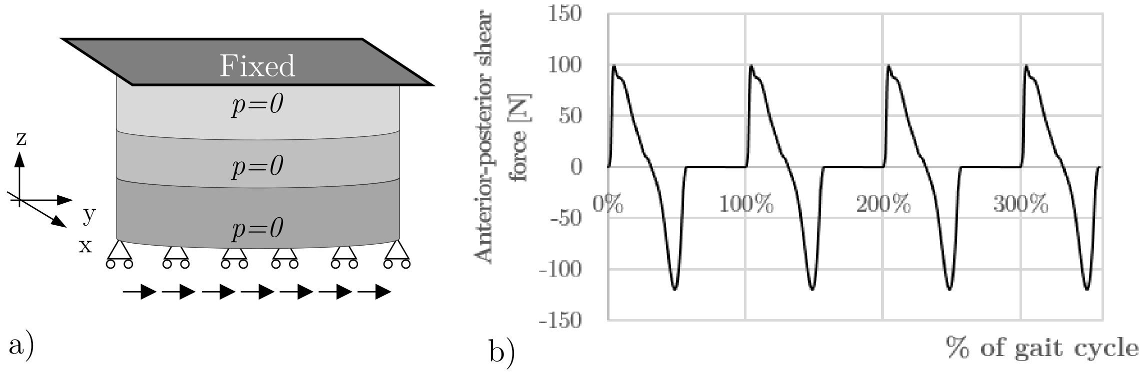

Figure 3.64 a) Boundary conditions applied to the scaffold. b) Anterior-posterior shear force as a function of four gait cycles. Data are experimentally measured from a healthy subject as introduced in §3.1.6; in the analyses only the 20% of the load is considered.

Starting from these observations, our ongoing work is to define a possible risk of delamination due to shear stress applied. No delamination was found experimentally by the Houston team in usual applications, but additional studies must be done in the future to assess this risk, depending on stress states reached. By taking advantage of the numerical results, an appropriate delamination criterion can be identified and stress limits, such as in [113], [114], must be obtained by experimental measurements. In this way, modifications on the scaffold geometry can be tested through numerical results and then verified to the delamination risk with a tuned computational model based on the developed criterion. Though this is an ongoing research, these results are encouraging and show the possibilities offered by the computational model, in a context of mutual collaboration between physicians and engineers, in the definition of medical procedures or scaffold best-choice geometries.

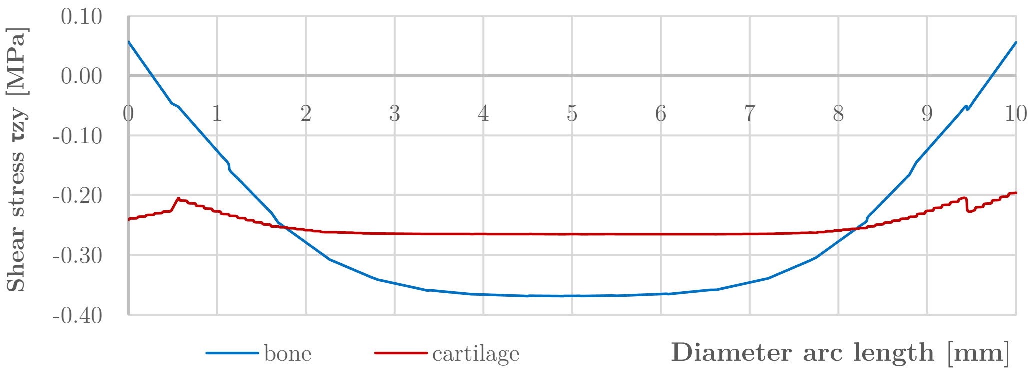

Figure 3.65 Shear stress values (τ_{zy}) along the diameter in the bone and in the cartilage layers near the interface surfaces between different materials.

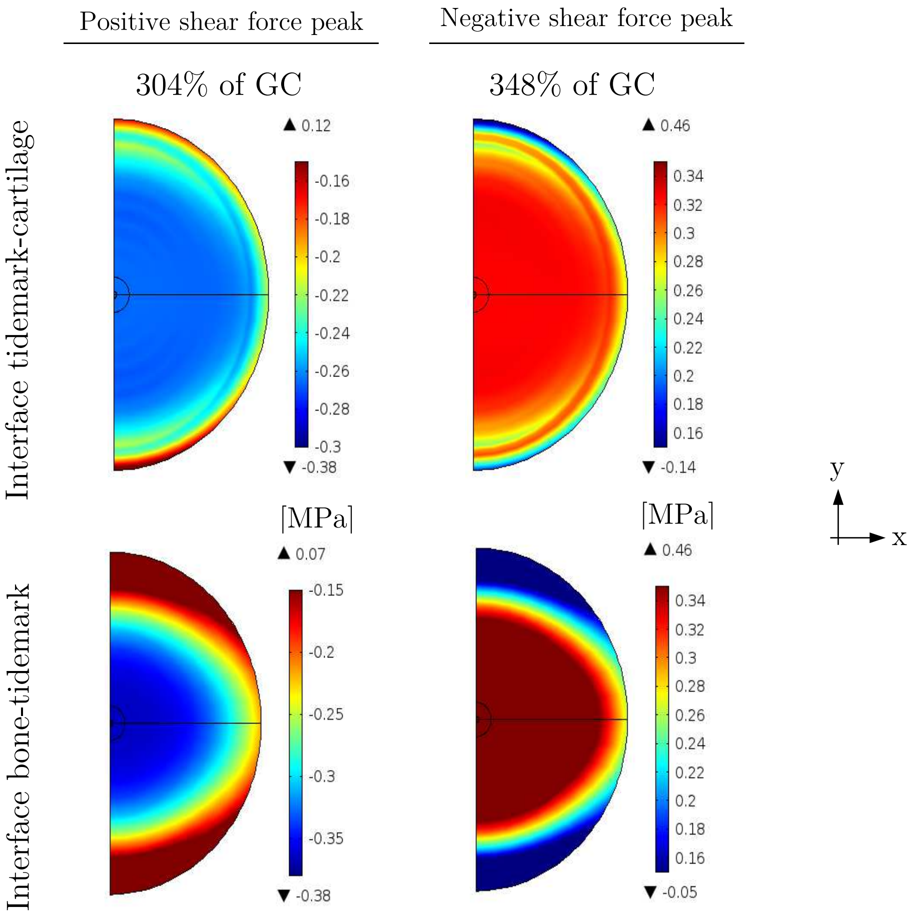

Figure 3.66 Contour plot of the shear stress component τ_{zy} at the last peak in both positive and negative shear forces, at the two interfaces (tidemark-cartilage at the top and bone-tidemark at the bottom)

4. Appendix

4.1. The Darcy's law from the TCAT

Let us derive the Darcy's law introduced in (3.17), following the same derivation in [10], [20]. We start from the linear momentum balance (2.52) expressed for the interstitial fluid as follows:

$$\varepsilon^f \rho^f \mathbf{g}^f + \nabla \cdot \varepsilon^f \mathbf{t}^f + \sum_{\kappa \in \Im_{cf}} \overset{\kappa \to f}{\mathbf{T}} = 0 \tag{4.1}$$

with the meaning of the terms as in §2.2.5.

Terms in the entropy inequality are arranged into force-flux pairs thanks to the TCAT closure method. Each term of these pairs is zero at the equilibrium: thus, the closure of the conservation system is accomplished by this constraint in case of near equilibrium conditions. This situation is verified for slow fluid flow regime, as in our cases. Following [10], the entropy inequality can be written by considering negligible fluid phase volume fraction variation and isothermal condition as:

$$\frac{\varepsilon^f}{\theta^f}\left(\mathbf{t}^f + p^f \mathbf{I}\right) : \mathbf{d}^f - \frac{1}{\theta^f}\left[-p^f \nabla \varepsilon^f + \sum_{\kappa \in \Im_{cf}} \overset{\kappa \to f}{\mathbf{T}}\right] \cdot \left(\mathbf{v}^f - \mathbf{v}^s\right) \geq 0 \tag{4.2}$$

where θ^f is the macroscale temperature of the fluid phase and $\mathbf{d}^f = \frac{1}{2}\left[\nabla \mathbf{v}^f + \left(\nabla \mathbf{v}^f\right)^T\right]$ is the rate of strain tensor of the fluid phase. In (4.2) two force-flux products can be seen: they must be zero at the equilibrium configuration and they must be non-negative to satisfy (4.2). Thus, two linear relations can be introduced for the first terms of each product:

$$-p^f \nabla \varepsilon^f + \sum_{\kappa \in \Im_{cf}} \overset{\kappa \to f}{\mathbf{T}} = -\mathbf{R}^f \cdot \left(\mathbf{v}^f - \mathbf{v}^s\right) \geq 0 \tag{4.3}$$

$$\mathbf{t}^f + p^f \mathbf{I} = \mathbf{A}^f : \mathbf{d}^f \tag{4.4}$$

where $\mathbf{R}^f$ is a symmetric, positive and semi-definite tensor representative of the resistance to flow, whereas $\mathbf{A}^f$ is a fourth order tensor that links the stress tensor with the rate of strain. Usually, it is assumed zero at the macroscale for slow flow, leading equation (4.4) to:

$$\mathbf{t}^f = -p^f \mathbf{I} \tag{4.5}$$

By substituting (4.3) and (4.5) into (4.1) we finally obtain:

$$\varepsilon^f \nabla p^f - \varepsilon^f \rho^f \mathbf{g}^f + \mathbf{R}^f \cdot \left(\mathbf{v}^f - \mathbf{v}^s \right) = 0 \tag{4.6}$$

Instead of using $\mathbf{R}^f$ tensor, intrinsic permeability and dynamic viscosity are usually used, resulting:

$$-\frac{\mathbf{k}}{\mu^f} \left(\nabla p^f - \rho^f \mathbf{g}^f \right) = \varepsilon^f \left(\mathbf{v}^f - \mathbf{v}^s \right) \tag{4.7}$$

where $\mathbf{R}^f = \left(\varepsilon^f \right)^2 \dfrac{\mu^f}{\mathbf{k}}$

By neglecting the gravity term in (4.7), equation (3.17) is finally obtained.

4.2. The Terzaghi consolidation benchmark

The Terzaghi consolidation benchmark is considered to test our model. A column of fully saturated sand is loaded at $t = 0$ with a constant pressure on the top (Figure 4.1). As a consequence, an overpressure p_0 and a vertical displacement w_0 can be appreciated at the initial time. The displacements normal to the lateral surfaces are restrained, except for top one. On that surface a boundary condition of zero interstitial fluid pressure is applied. Furthermore, compressibility of the fluid and the solid are zero.

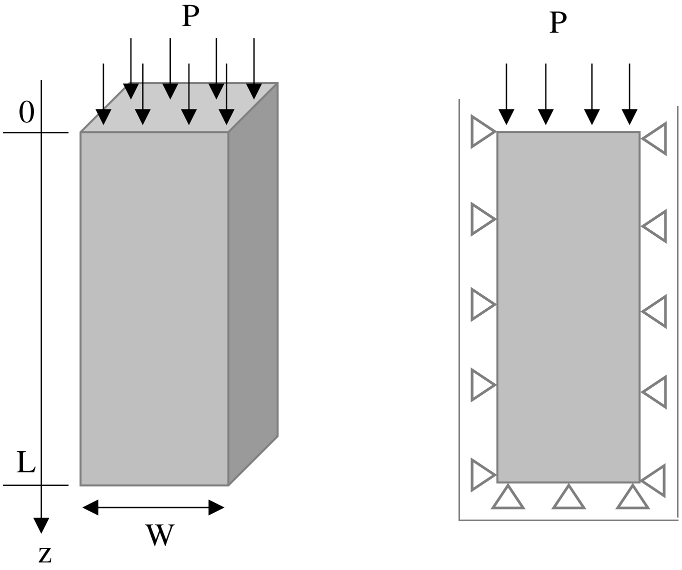

Figure 4.1 Geometry of the sand column for the Terzaghi consolidation benchmark.

The values of the interstitial fluid pressure and of the displacements as function of the depth and time are obtained analytically through the following relations [115], [116]:

$$p_f\left(z,t\right) = \frac{4p_0}{\pi}{}_0\sum_{m=0}^{\infty}\frac{1}{2m+1}\exp\left[\frac{-\left(2m+1\right)^2\pi^2 ct}{4L^2}\right]\sin\left[\frac{\left(2m+1\right)\pi z}{2L}\right] \tag{4.8}$$

$$w\left(z,t\right)=c_M p_0\left\{\left(L-z\right)-\frac{8L}{\pi^2}\sum_{m=0}^{\infty}\frac{1}{\left(2m+1\right)^2}\exp\left[\frac{-\left(2m+1\right)^2\pi^2 ct}{4L^2}\right]\cos\left[\frac{\left(2m+1\right)\pi z}{2L}\right]\right\}+w_0 \tag{4.9}$$

where $p_0=\frac{\alpha_B S}{K_u+4G/3}P_L$, $w_0=\frac{1}{K_u+4G/3}P_L\left(L-z\right)$, and the other parameters are specified in Table 9.

H	Height	15.00	m
W	Width	1.00	m
α_B	Biot's coefficient	1	
n	Porosity	0.375	
β_f	Fluid compressibility	4.40E-30	Pa^{-1}
β_s	Solid grain compressibility	0	Pa^{-1}
K	Bulk modulus	6.67E+07	Pa
G	Shear modulus	4.00E+07	Pa
P_L	Pressure	1.00E+04	Pa
k_{sand}	Permeability	1.00E-05	m/s
g	Gravity	9.81	m/s^2
ρ_f	Density of fluid	1.00E+03	kg/m^3
S	Storage coefficient	6.06E+29	Pa
K_u	Undrained Bulk modulus	6.06E+29	Pa
c_M	Vertical uniaxial compressibility	8.33E-09	1/Pa
γ_f	Specific weight of the fluid	9.81E+03	N/m^3
c	Consolidation coefficient	1.22E-01	m^2/s
p_0	Initial fluid pressure	1.00E+04	Pa

Table 9 Parameter of the consolidation benchmark from [116]

Figure 4.2 shows that our model gives pressures and displacements, which are overlapping with the analytical ones, showing a very good accuracy of numerical computations.

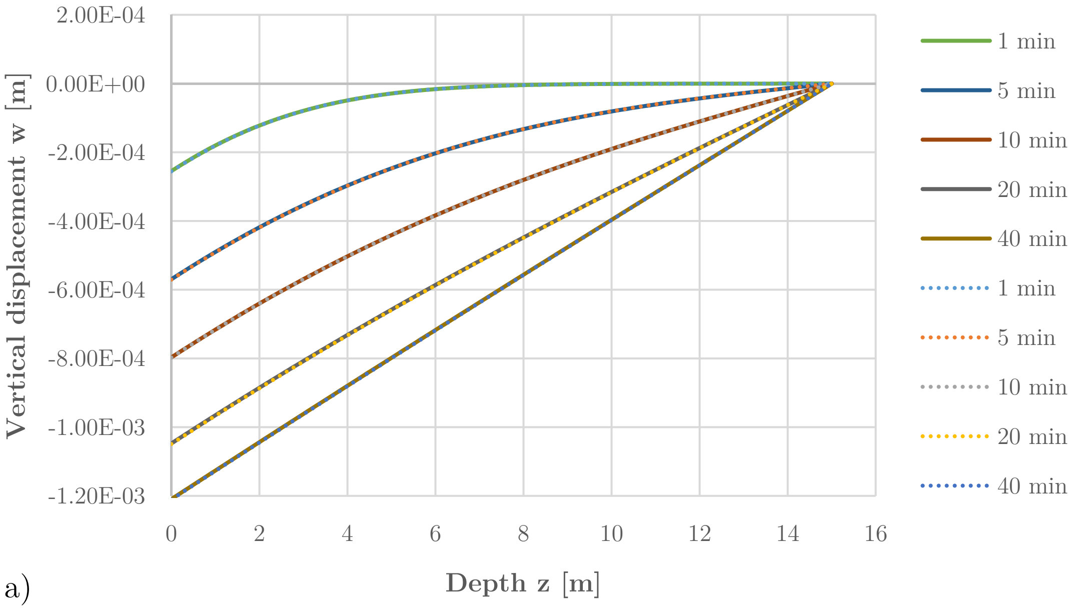

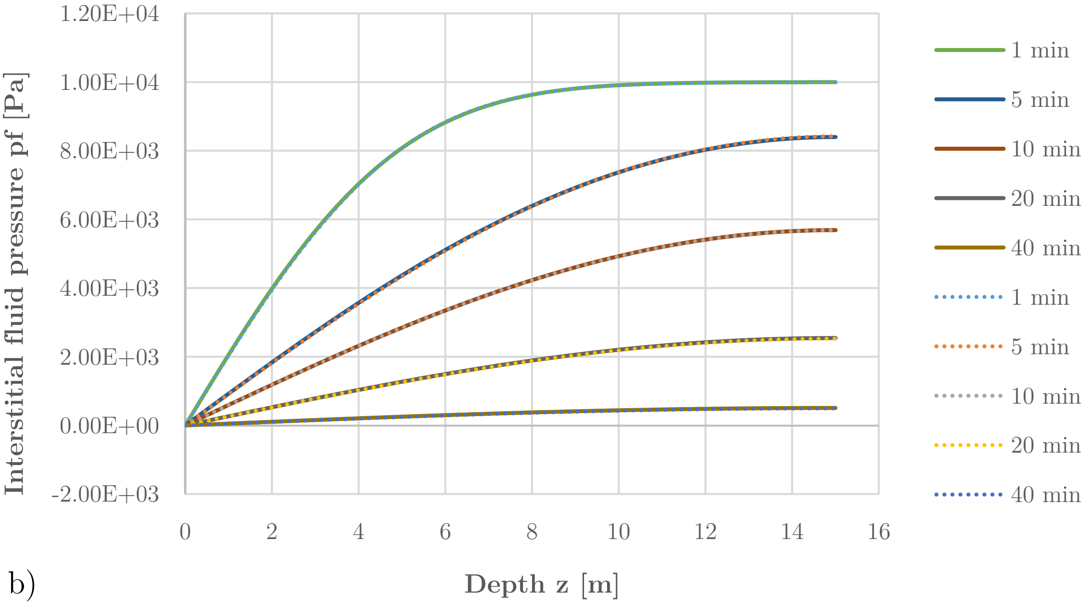

Figure 4.2 Vertical displacement (a) and interstitial fluid pressure (b) over the depth of the column at different times. Continuous lines stand for the analytical results, dotted lines represent the finite element results.

5. References

[1] H. A. Mang, “Numerical methods in finite element analysis, K. J. Bathe and E. L. Wilson, Prentice-Hall, Englewood Cliffs, N. J., 1976. No. of pages: 528. price: $\$28 \cdot 95$,” *Int. J. Numer. Methods Eng.*, vol. 11, no. 9, pp. 1485–1485, 1977.

[2] G. Strang and G. Fix, “An analysis of the finite element method,” 1973.

[3] O. C. Zienkiewicz, R. L. Taylor, and J. Z. Zhu, *The Finite Element Method: Its Basis and Fundamentals.* Butterworth-Heinemann, 2005.

[4] K.-J. Bathe, *Finite Element Procedures.* 2006.

[5] H. G. Knoopers, A. Nijhuis, E. J. G. Krooshoop, H. H. J. ten Kate, P. Bruzzone, P. J. Lee, and A. A. Squitieri, “Third round of the ITER strand bench mark test,” pp. 1271–1274, Jan. 1997.

[6] S. Minardi, B. Corradetti, F. Taraballi, M. Sandri, J. Van Eps, F. J. Cabrera, B. K. Weiner, A. Tampieri, and E. Tasciotti, “Evaluation of the osteoinductive potential of a bio-inspired scaffold mimicking the osteogenic niche for bone augmentation.,” *Biomaterials*, vol. 62, pp. 128–37, Sep. 2015.

[7] Z. Sawacha, G. Cristoferi, G. Guarneri, S. Corazza, G. Donà, P. Denti, A. Facchinetti, A. Avogaro, and C. Cobelli, “Characterizing multisegment foot kinematics during gait in diabetic foot patients.,” *J. Neuroeng. Rehabil.*, vol. 6, no. 1, p. 37, Jan. 2009.

[8] A. Scarton, A. Guiotto, Z. Sawacha, G. Guarneri, A. Avogaro, and C. Cobelli, “2-Dimensional foot FE models for clinical application in gait analysis,” *J. Foot Ankle Res.*, vol. 7, no. Suppl 1, p. A73, Apr. 2014.

[9] A. Guiotto, Z. Sawacha, G. Guarneri, A. Avogaro, and C. Cobelli, “3D finite element model of the diabetic neuropathic foot: a gait analysis driven approach.,” *J. Biomech.*, vol. 47, no. 12, pp. 3064–71, Sep. 2014.

[10] G. Sciumè, S. Shelton, W. G. Gray, C. T. Miller, F. Hussain, M. Ferrari, P. Decuzzi, and B. a Schrefler, “A multiphase model for three-dimensional tumor growth,” *New J. Phys.*, vol. 15, no. 1, p. 015005, Jan. 2013.

[11] G. Sciumè, W. G. Gray, F. Hussain, M. Ferrari, P. Decuzzi, and B. a. Schrefler,

"Three phase flow dynamics in tumor growth," *Comput. Mech.*, vol. 53, no. 3, pp. 465–484, Dec. 2013.

[12] S. E. Shelton, "Mechanistic Modeling of Cancer Tumor Growth Using a Porous Media Approach," 2011.

[13] G. Sciumè, W. G. Gray, M. Ferrari, P. Decuzzi, and B. a. Schrefler, "On Computational Modeling in Tumor Growth," *Arch. Comput. Methods Eng.*, vol. 20, no. 4, pp. 327–352, Oct. 2013.

[14] W. Ehlers, N. Karajan, and B. Markert, "An extended biphasic model for charged hydrated tissues with application to the intervertebral disc.," *Biomech. Model. Mechanobiol.*, vol. 8, no. 3, pp. 233–51, Jun. 2009.

[15] E. A. Meroi, A. N. Natali, and B. A. Schrefler, "A Porous Media Approach to Finite Deformation Behaviour in Soft Tissues.," *Comput. Methods Biomech. Biomed. Engin.*, vol. 2, no. 3, pp. 157–170, Jan. 1999.

[16] D. J. Kelly and P. J. Prendergast, "Mechano-regulation of stem cell differentiation and tissue regeneration in osteochondral defects.," *J. Biomech.*, vol. 38, no. 7, pp. 1413–22, Jul. 2005.

[17] J. Crank, "The Mathematics of Diffusion," *Ann. Nucl. Energy*, vol. 4, no. 4–5, pp. 205–206, 1977.

[18] A. Fick, "Ueber Diffusion," *Ann. der Phys. und Chemie*, vol. 170, no. 1, pp. 59–86, 1855.

[19] J. B. J. Fourier, *Théorie analytique de la chaleur*. Paris: F. Didot, 1822.

[20] W. G. Gray and C. Miller, *Introduction to the Thermodynamically Constrained Averaging Theory for Porous Medium Systems*, 1st ed. Zürich, Switzerland: Springer International Publishing, 2014.

[21] G. F. Pinder and W. G. Gray, *Essentials of Multiphase Flow and Transport in Porous Media*, 1st ed. Hoboken, New Jersey: John Wiley & Sons, 2008.

[22] W. G. Gray and C. T. Miller, "Thermodynamically constrained averaging theory approach for modeling flow and transport phenomena in porous medium systems: 1. Motivation and overview," *Adv. Water Resour.*, vol. 28, no. 2, pp. 161–180, Feb. 2005.

[23] W. G. Gray and C. T. Miller, "Thermodynamically constrained averaging theory approach for modeling flow and transport phenomena in porous medium systems: 3. Single-fluid-phase flow," *Adv. Water Resour.*, vol. 29, no. 11, pp.

1745–1765, Nov. 2006.

[24] C. T. Miller and W. G. Gray, “Thermodynamically constrained averaging theory approach for modeling flow and transport phenomena in porous medium systems: 2. Foundation,” *Adv. Water Resour.*, vol. 28, no. 2, pp. 181–202, Feb. 2005.

[25] C. T. Miller and W. G. Gray, “Thermodynamically Constrained Averaging Theory Approach for Modeling Flow and Transport Phenomena in Porous Medium Systems: 4. Species Transport Fundamentals.,” *Adv. Water Resour.*, vol. 31, no. 3, pp. 577–597, Mar. 2008.

[26] W. G. Gray and C. T. Miller, “Thermodynamically Constrained Averaging Theory Approach for Modeling Flow and Transport Phenomena in Porous Medium Systems: 5. Single-Fluid-Phase Transport.,” *Adv. Water Resour.*, vol. 32, no. 5, pp. 681–711, May 2009.

[27] G. Sciumè, “Thermo-hygro-chemo-mechanical model of concrete at early ages and its extension to tumor growth numerical analysis,” University of Padova, 2012.

[28] R. Lewis and B. Schrefler, *Finite Element Method in the Deformation and Consolidation of Porous Media*, 2nd ed. Chichester: John Wiley & Sons, 1998.

[29] K. G. Alberti and P. Z. Zimmet, “Definition, diagnosis and classification of diabetes mellitus and its complications. Part 1: diagnosis and classification of diabetes mellitus provisional report of a WHO consultation.,” *Diabet. Med.*, vol. 15, no. 7, pp. 539–53, Jul. 1998.

[30] American Diabetes Association, “Diagnosis and classification of diabetes mellitus.,” *Diabetes Care*, vol. 33 Suppl 1, pp. S62–9, Jan. 2010.

[31] D. M. Nathan, “Long-Term Complications of Diabetes Mellitus,” *N. Engl. J. Med.*, vol. 328, no. 23, pp. 1676–1685, Jun. 1993.

[32] N. Singh, D. G. Armstrong, and B. A. Lipsky, “Preventing foot ulcers in patients with diabetes.,” *JAMA*, vol. 293, no. 2, pp. 217–28, Jan. 2005.

[33] S. Zimny, H. Schatz, and M. Pfohl, “The Role of Limited Joint Mobility in Diabetic Patients With an At-Risk Foot,” *Diabetes Care*, vol. 27, no. 4, pp. 942–946, Mar. 2004.

[34] D. S. B. Williams, D. Brunt, and R. J. Tanenberg, “Diabetic neuropathy is related to joint stiffness during late stance phase.,” *J. Appl. Biomech.*, vol. 23,

no. 4, pp. 251–60, Nov. 2007.

[35] D. J. Fernando, E. A. Masson, A. Veves, and A. J. Boulton, “Relationship of Limited Joint Mobility to Abnormal Foot Pressures and Diabetic Foot Ulceration,” *Diabetes Care*, vol. 14, no. 1, pp. 8–11, Jan. 1991.

[36] M. J. Mueller, M. Hastings, P. K. Commean, K. E. Smith, T. K. Pilgram, D. Robertson, and J. Johnson, “Forefoot structural predictors of plantar pressures during walking in people with diabetes and peripheral neuropathy,” *J. Biomech.*, vol. 36, no. 7, pp. 1009–1017, Jul. 2003.

[37] K. . Maluf and M. . Mueller, “Comparison of physical activity and cumulative plantar tissue stress among subjects with and without diabetes mellitus and a history of recurrent plantar ulcers,” *Clin. Biomech.*, vol. 18, no. 7, pp. 567–575, Aug. 2003.

[38] D. G. Armstrong and L. a Lavery, “Diabetic foot ulcers: prevention, diagnosis and classification.,” *Am. Fam. Physician*, vol. 57, no. 6, pp. 1325–32, 1337–8, 1998.

[39] A. Erdemir, J. J. Saucerman, D. Lemmon, B. Loppnow, B. Turso, J. S. Ulbrecht, and P. R. Cavanagh, “Local plantar pressure relief in therapeutic footwear: design guidelines from finite element models.,” *J. Biomech.*, vol. 38, no. 9, pp. 1798–806, Sep. 2005.

[40] K. M. Patil, L. H. Braak, and A. Huson, “Analysis of stresses in two-dimensional models of normal and neuropathic feet,” *Med. Biol. Eng. Comput.*, vol. 34, no. 4, pp. 280–284, Jul. 1996.

[41] A. Gefen, “Plantar soft tissue loading under the medial metatarsals in the standing diabetic foot,” *Med. Eng. Phys.*, vol. 25, no. 6, pp. 491–499, Jul. 2003.

[42] J. T. Cheung and M. Zhang, “Finite Element Modeling of the Human Foot and Footwear,” pp. 145–159.

[43] J. T.-M. Cheung, M. Zhang, A. K.-L. Leung, and Y.-B. Fan, “Three-dimensional finite element analysis of the foot during standing—a material sensitivity study,” *J. Biomech.*, vol. 38, no. 5, pp. 1045–1054, May 2005.

[44] J. T.-M. Cheung and M. Zhang, “A 3-dimensional finite element model of the human foot and ankle for insole design.,” *Arch. Phys. Med. Rehabil.*, vol. 86, no. 2, pp. 353–8, Feb. 2005.

[45] G. Sciumè, A. Guiotto, Z. Sawacha, D. P. Boso, C. Cobelli, and B. A. Schrefler,

"A porous media approach for foot biomechanics," in *XII International Conference on Computational Plasticity. Fundamentals and Applications. COMPLAS XII*, 2013, pp. 1–10.

[46] G. Sciumè, D. P. Boso, W. G. Gray, C. Cobelli, and B. A. Schrefler, "A two-phase model of plantar tissue: a step toward prediction of diabetic foot ulceration.," *Int. j. numer. method. biomed. eng.*, vol. 30, no. 11, pp. 1153–69, Nov. 2014.

[47] D. P. Boso, G. Sciumè, M. Pizzocaro, and B. A. Schrefler, "A poroelastic model for plantar tissue during gait: main features and perspectives," in *11th World Congress on Computational Mechanics (WCCM XI)*, 2014.

[48] D. P. Boso, G. Sciumè, M. Pizzocaro, and B. A. Schrefler, "A porous media approach for plantar tissue during gait," *PAMM*, vol. 15, no. 1, pp. 87–88, Oct. 2015.

[49] M. Pizzocaro, A. Guiotto, G. Sciumè, Z. Sawacha, C. Cobelli, D. P. Boso, and B. A. Schrefler, "A foot finite element model integrating porous media approach and gait analysis: A step forward in the study of the diabetic foot disease," *Gait Posture*, vol. 42, pp. S24–S25, Sep. 2015.

[50] L. Preziosi and G. Vitale, *a Multiphase Model of Tumor and Tissue Growth Including Cell Adhesion and Plastic Reorganization*, vol. 21, no. 09. 2011.

[51] L. Preziosi and G. Vitale, "Mechanical Aspects of Tumour Growth: Multiphase Modelling, Adhesion, and Evolving Natural Configuration," in *New Trends in the Physics and Mechanics of Biological Systems*, M. Ben Amar, A. Goriely, M. M. Müller, and L. F. Cugliandolo, Eds. Oxford: Oxford University Press, 2011, pp. 177–228.

[52] J. E. Marsden and T. J. R. Hughes, *Mathematical Foundations of Elasticity.* New York: Dover Publications, Inc., 1994.

[53] S. M. Hassanizadeh and W. G. Gray, "Mechanics and thermodynamics of multiphase flow in porous media including interphase boundaries," *Adv. Water Resour.*, vol. 13, no. 4, pp. 169–186, Dec. 1990.

[54] M. A. Biot and D. G. Willis, "The Elastic Coefficients of the Theory of Consolidation," vol. 24, pp. 594–601, Jan. 1957.

[55] T. Belytschko, W. Liu, and B. Moran, *Nonlinear finite elements for continua and structures. 2000*, vol. 16. 2000.

[56] Dassault Systèmes, *Abaqus Theory Manual v.6.13.* 2014.

[57] P. J. Flory, “Thermodynamic relations for high elastic materials,” *Trans. Faraday Soc.*, vol. 57, p. 829, 1961.

[58] Z. Sawacha, G. Cristoferi, G. Guarneri, S. Corazza, G. Donà, A. Facchinetti, C. Denard, M. Sommavilla, M. Zaccaria, A. Avogaro, and C. Cobelli, “A method for the simultaneous assessment of gait and posture,” Jan. 2005.

[59] J. A. Stebbins, M. E. Harrington, C. Giacomozzi, N. Thompson, A. Zavatsky, and T. N. Theologis, “Assessment of sub-division of plantar pressure measurement in children.,” *Gait Posture*, vol. 22, no. 4, pp. 372–6, Dec. 2005.

[60] Z. Sawacha, G. Guarneri, G. Cristoferi, A. Guiotto, A. Avogaro, and C. Cobelli, “Integrated kinematics-kinetics-plantar pressure data analysis: a useful tool for characterizing diabetic foot biomechanics.,” *Gait Posture*, vol. 36, no. 1, pp. 20–6, May 2012.

[61] A. Gefen, M. Megido-Ravid, Y. Itzchak, and M. Arcan, “Biomechanical Analysis of the Three-Dimensional Foot Structure During Gait: A Basic Tool for Clinical Applications,” *J. Biomech. Eng.*, vol. 122, no. 6, p. 630, Dec. 2000.

[62] W.-M. Chen, T. Lee, P. V.-S. Lee, J. W. Lee, and S.-J. Lee, “Effects of internal stress concentrations in plantar soft-tissue--A preliminary three-dimensional finite element analysis.,” *Med. Eng. Phys.*, vol. 32, no. 4, pp. 324–31, May 2010.

[63] D. Lemmon, T. Y. Shiang, A. Hashmi, J. S. Ulbrecht, and P. R. Cavanagh, “The effect of insoles in therapeutic footwear—A finite element approach,” *J. Biomech.*, vol. 30, no. 6, pp. 615–620, Jun. 1997.

[64] W.-P. Chen, F.-T. Tang, and C.-W. Ju, “Stress distribution of the foot during mid-stance to push-off in barefoot gait: a 3-D finite element analysis,” *Clin. Biomech.*, vol. 16, no. 7, pp. 614–620, Aug. 2001.

[65] T.-M. Chu, N. P. Reddy, and J. Padovan, “Three-dimensional finite element stress analysis of the polypropylene, ankle-foot orthosis: static analysis,” *Med. Eng. Phys.*, vol. 17, no. 5, pp. 372–379, Jul. 1995.

[66] A. Fahlgren, L. Johansson, U. Edlund, and P. Aspenberg, “Direct ex vivo measurement of the fluid permeability of loose scar tissue.,” *Acta Bioeng. Biomech. / Wrocław Univ. Technol.*, vol. 14, no. 2, pp. 47–51, Jan. 2012.

[67] D. M. Hamby, “A comparison of sensitivity analysis techniques.,” *Health*

Phys., vol. 68, no. 2, pp. 195–204, Feb. 1995.

[68] K. Terzaghi, R. B. Peck, and G. Mesri, *Soil Mechanics in Engineering Practice, Third Edition.* New York: Wiley-Interscience Publication, John Wiley and Sons, Inc., 1996.

[69] M. A. Biot, “General theory of three dimensional consolidation,” *J. Appl. Phys.*, vol. 12, no. 2, pp. 155–164, 1941.

[70] L. Geris, *Computational Modeling in Tissue Engineering*, vol. 10. 2013.

[71] D. W. Hutmacher, J. T. Schantz, C. Xu, F. Lam, K. C. Tan, and T. C. Lim, “State of the art and future directions of scaffold-based bone engineering from a biomaterials perspective,” no. June, pp. 245–260, 2007.

[72] D. R. Carter, P. R. Blenman, and G. S. Beauprk, “Correlations between Mechanical Stress History and Tissue Differentiation in Initial Fracture Healing,” *J. Orthop. Res.*, pp. 6736–748, 1988.

[73] A. L. Olivares, E. Marsal, J. A. Planell, and D. Lacroix, “Finite element study of scaffold architecture design and culture conditions for tissue engineering.,” *Biomaterials*, vol. 30, no. 30, pp. 6142–9, Oct. 2009.

[74] C. Liu, Z. Xia, and J. T. Czernuszka, “Design and Development of Three-Dimensional Scaffolds for Tissue Engineering,” *Chem. Eng. Res. Des.*, vol. 85, no. 7, pp. 1051–1064, Jan. 2007.

[75] F. P. W. Melchels, K. Bertoldi, R. Gabbrielli, A. H. Velders, J. Feijen, and D. W. Grijpma, “Mathematically defined tissue engineering scaffold architectures prepared by stereolithography.,” *Biomaterials*, vol. 31, no. 27, pp. 6909–16, Sep. 2010.

[76] R. Zhang and P. X. Ma, “Porous poly(L-lactic acid)/apatite composites created by biomimetic process.,” *J. Biomed. Mater. Res.*, vol. 45, no. 4, pp. 285–93, Jun. 1999.

[77] D. W. Hutmacher, “Scaffolds in tissue engineering bone and cartilage,” *Biomaterials*, vol. 21, no. 24, pp. 2529–2543, Dec. 2000.

[78] S. J. Hollister, “Porous scaffold design for tissue engineering.,” *Nat. Mater.*, vol. 4, no. 7, pp. 518–24, Jul. 2005.

[79] R. J. Shipley, G. W. Jones, R. J. Dyson, B. G. Sengers, C. L. Bailey, C. J. Catt, C. P. Please, and J. Malda, “Design criteria for a printed tissue engineering construct: a mathematical homogenization approach.,” *J. Theor.*

Biol., vol. 259, no. 3, pp. 489–502, Aug. 2009.

[80] D. Wendt, S. Stroebel, M. Jakob, G. T. John, and I. Martin, “Uniform tissues engineered by seeding and culturing cells in 3D scaffolds under perfusion at defined oxygen tensions.,” *Biorheology*, vol. 43, no. 3–4, pp. 481–8, Jan. 2006.

[81] D. Wendt, A. Marsano, M. Jakob, M. Heberer, and I. Martin, “Oscillating perfusion of cell suspensions through three-dimensional scaffolds enhances cell seeding efficiency and uniformity.,” *Biotechnol. Bioeng.*, vol. 84, no. 2, pp. 205–14, Oct. 2003.

[82] J.-L. Milan, J. A. Planell, and D. Lacroix, “Computational modelling of the mechanical environment of osteogenesis within a polylactic acid-calcium phosphate glass scaffold.,” *Biomaterials*, vol. 30, no. 25, pp. 4219–26, Sep. 2009.

[83] F. Pauwels, “A new theory on the influence of mechanical stimuli on the differentiation of supporting tissue. The tenth contribution to the functional anatomy and causal morphology of the supporting structure.,” *Zeitschrift für Anat. und Entwicklungsgeschichte*, vol. 121, pp. 478–515, Jan. 1960.

[84] D. R. Carter, G. S. Beaupré, N. J. Giori, and J. A. Helms, “Mechanobiology of skeletal regeneration.,” *Clin. Orthop. Relat. Res.*, no. 355 Suppl, pp. S41–55, Oct. 1998.

[85] L. E. Claes, C. A. Heigele, C. Neidlinger-Wilke, D. Kaspar, W. Seidl, K. J. Margevicius, and P. Augat, “Effects of mechanical factors on the fracture healing process.,” *Clin. Orthop. Relat. Res.*, no. 355 Suppl, pp. S132–47, Oct. 1998.

[86] L. E. Claes and C. A. Heigele, “Magnitudes of local stress and strain along bony surfaces predict the course and type of fracture healing,” *J. Biomech.*, vol. 32, no. 3, pp. 255–266, Mar. 1999.

[87] C. Ament and E. . Hofer, “A fuzzy logic model of fracture healing,” *J. Biomech.*, vol. 33, no. 8, pp. 961–968, Aug. 2000.

[88] S. J. Shefelbine, P. Augat, L. Claes, and U. Simon, “Trabecular bone fracture healing simulation with finite element analysis and fuzzy logic.,” *J. Biomech.*, vol. 38, no. 12, pp. 2440–50, Dec. 2005.

[89] P. J. Prendergast, R. Huiskes, and K. Søballe, “Biophysical stimuli on cells during tissue differentiation at implant interfaces,” *J. Biomech.*, vol. 30, no. 6,

pp. 539–548, Jun. 1997.

[90] D. J. Kelly and P. J. Prendergast, “Prediction of the optimal mechanical properties for a scaffold used in osteochondral defect repair.,” *Tissue Eng.*, vol. 12, no. 9, pp. 2509–2519, 2006.

[91] D. Lacroix and P. J. Prendergast, “A mechano-regulation model for tissue differentiation during fracture healing: analysis of gap size and loading,” *J. Biomech.*, vol. 35, no. 9, pp. 1163–1171, Sep. 2002.

[92] D. Lacroix, P. J. Prendergast, G. Li, and D. Marsh, “Biomechanical model to simulate tissue differentiation and bone regeneration: application to fracture healing.,” *Med. Biol. Eng. Comput.*, vol. 40, no. 1, pp. 14–21, 2002.

[93] D. P. Byrne, D. Lacroix, and P. J. Prendergast, “Simulation of fracture healing in the tibia: mechanoregulation of cell activity using a lattice modeling approach.,” *J. Orthop. Res.*, vol. 29, no. 10, pp. 1496–503, Oct. 2011.

[94] B. S. McAllister and K. Haghighat, “Bone augmentation techniques.,” *J. Periodontol.*, vol. 78, no. 3, pp. 377–96, Mar. 2007.

[95] T. Albrektsson and C. Johansson, “Osteoinduction, osteoconduction and osseointegration.,” *Eur. Spine J.*, vol. 10 Suppl 2, pp. S96–101, Oct. 2001.

[96] W. S. Khan, F. Rayan, B. S. Dhinsa, and D. Marsh, “An osteoconductive, osteoinductive, and osteogenic tissue-engineered product for trauma and orthopaedic surgery: How far are we?,” *Stem Cells Int.*, vol. 2012, 2012.

[97] J. Patterson, M. M. Martino, and J. A. Hubbell, “Biomimetic materials in tissue engineering,” *Mater. Today*, vol. 13, no. 1–2, pp. 14–22, Jan. 2010.

[98] L. Corradi Dell’Acqua, *Meccanica delle strutture*, 2nd ed. Milano: McGraw-Hill Libri Italia, 2010.

[99] A. Tampieri, M. Sandri, E. Landi, D. Pressato, S. Francioli, R. Quarto, and I. Martin, “Design of graded biomimetic osteochondral composite scaffolds,” *Biomaterials*, vol. 29, no. 26, pp. 3539–3546, Sep. 2008.

[100] J. Y. Rho, R. B. Ashman, and C. H. Turner, “Young’s modulus of trabecular and cortical bone material: Ultrasonic and microtensile measurements,” *J. Biomech.*, vol. 26, no. 2, pp. 111–119, Feb. 1993.

[101] G. Sciumè, R. Santagiuliana, M. Ferrari, P. Decuzzi, and B. A. Schrefler, “A tumor growth model with deformable ECM,” *Phys. Biol.*, vol. 11, no. 6, p. 65004, 2014.

[102] A. M. Bhosale and J. B. Richardson, “Articular cartilage: structure, injuries and review of management.,” *Br. Med. Bull.*, vol. 87, no. 1, pp. 77–95, Jan. 2008.

[103] a R. Memon and J. F. Quinlan, “Surgical treatment of articular cartilage defects in the knee: are we winning?,” *Adv. Orthop.*, vol. 2012, p. 528423, 2012.

[104] A. Aroen, “Articular Cartilage Lesions in 993 Consecutive Knee Arthroscopies,” *Am. J. Sports Med.*, vol. 32, no. 1, pp. 211–215, Jan. 2004.

[105] K. Hjelle, E. Solheim, T. Strand, R. Muri, and M. Brittberg, “Articular cartilage defects in 1,000 knee arthroscopies,” *Arthroscopy*, vol. 18, no. 7, pp. 730–734, 2002.

[106] W. W. Curl, J. Krome, E. S. Gordon, J. Rushing, B. P. Smith, and G. G. Poehling, “Cartilage injuries: A review of 31,516 knee arthroscopies,” *Arthroscopy*, vol. 13, no. 4, pp. 456–460, 1997.

[107] J. A. Buckwalter and H. J. Mankin, “Instructional Course Lectures, The American Academy of Orthopaedic Surgeons - Articular Cartilage. Part I: Tissue Design and Chondrocyte-Matrix Interactions*†,” *J Bone Jt. Surg Am*, vol. 79, no. 4, pp. 600–611, 1997.

[108] A. Bernhardt, A. Lode, S. Boxberger, W. Pompe, and M. Gelinsky, “Mineralised collagen - An artificial, extracellular bone matrix - Improves osteogenic differentiation of bone marrow stromal cells,” *J. Mater. Sci. Mater. Med.*, vol. 19, no. 1, pp. 269–275, 2008.

[109] A. P. Newman, “Current Concepts Articular Cartilage Repair,” vol. 26, no. 2, 1998.

[110] I. Martin, S. Miot, A. Barbero, M. Jakob, and D. Wendt, “Osteochondral tissue engineering,” *J. Biomech.*, vol. 40, no. 4, pp. 750–765, 2007.

[111] H. Domaschke, M. Gelinsky, B. Burmeister, R. Fleig, T. Hanke, A. Reinstorf, W. Pompe, and A. Rösen-Wolff, “*In Vitro* Ossification and Remodeling of Mineralized Collagen I Scaffolds,” *Tissue Eng.*, vol. 12, no. 4, pp. 949–958, Apr. 2006.

[112] M. M. Attard, “Finite strain—isotropic hyperelasticity,” *Int. J. Solids Struct.*, vol. 40, no. 17, pp. 4353–4378, Aug. 2003.

[113] E. B. Chin, S. A. English, and T. M. Briggs, “Criteria for initiation of delamination in quasi-static punch-shear tests of a carbon-fiber composite

material," 2015.

[114] Z. Hashin and A. Rotem, "A Fatigue Failure Criterion for Fiber Reinforced Materials," *J. Compos. Mater.*, vol. 7, no. 4, pp. 448–464, Oct. 1973.

[115] H. Wang, *Theory of Linear Poroelasticity with Applications to Geomechanics and Hydrogeology.* 2000.

[116] S.-J. Wang and K.-C. Hsu, "The application of the first-order second-moment method to analyze poroelastic problems in heterogeneous porous media," *J. Hydrol.*, vol. 369, no. 1–2, pp. 209–221, May 2009.

Acknowledgements

I think that people in our life make it valuable and precious, with their support, but also only with their presence. This paragraph is the occasion for me to acknowledge the people that, directly or indirectly, contributed to the realization of this work.

I would like to express my gratitude to prof. D. Boso for instilling me her passion, and for making her valuable support and her expertise available for me in these nine years of collaboration.

I would like to thank P. Mascheroni for his inestimable help in the development of my thesis, but especially for his authentic friendship.

I want to express my gratitude to prof. B. Schrefler for the opportunities he gave me and for his tireless dedication to the research fields he loves.

I would like to thank Riccardo T., Alessandro, Claudia, Mauro, Riccardo M., Lorenzo, Fabio, Paolo, Claudio, Filippo, Paola, Silvia and Laura, because during this PhD I found not only colleagues, but extraordinary friends for life.

I would also like to express thanks to my friends that fill with their happiness, acuity and sincere support my free time.

And finally, I would like to thank my family, for being always naturally supportive and affectionate, and to Alessia, for having shared with me a joyful period of our lives.